The Dissertation Committee for Kiran Venugopal
certifies that this is the approved version of the following dissertation:

Millimeter Wave Wearable Communication Networks: Analytic Modeling and MIMO Support

Committee:

Robert W. Heath, Jr., Supervisor

François Baccelli

Matthew C. Valenti

Gustavo de Veciana

Haris Vikalo

Millimeter Wave Wearable Communication Networks: Analytic Modeling and MIMO Support

by

Kiran Venugopal

DISSERTATION

Presented to the Faculty of the Graduate School of

The University of Texas at Austin

in Partial Fulfillment

of the Requirements

for the Degree of

DOCTOR OF PHILOSOPHY

THE UNIVERSITY OF TEXAS AT AUSTIN

August 2017

Dedicated to my parents.

Acknowledgments

Firstly, I thank God for this life, its challenges, successes, failures and all experiences. I am forever indebted to my parents Gita and Venugopal for their sacrifices and unconditional love throughout. My journeys would never have been completed without them. My life has been considerably enhanced thanks to my many relatives – uncles, aunts, cousins, nephews and nieces. Many do not know that I have in these extra-ordinarily lovely and caring people, a massive support system. A special addition to this came in the form of my wife Praseetha and in-laws, making my life more colorful and joyous. I am thankful to all of them.

I am indebted to all my teachers, who set the foundations of my education. All my academic achievements trace back to them. My sincere gratitude to my supervisor Prof. Robert W. Heath, Jr. for his decisive advice and guidance. I am fortunate that I got a mentor in him who helped me fully utilize my potential, giving me clarity whenever in doubt. I would like to thank my doctoral committee members Prof. François Baccelli, Prof. Matthew Valenti, Prof. Gustavo de Veciana, and Prof. Haris Vikalo. Their encouraging comments and insights greatly improved my research. I am grateful to Prof. Matthew Valenti for his guidance and technical help to this work.

Special thanks to Dr. Kerstin Johnsson, Intel Labs, Prof. Angel Lozano and Geordie George from UPF Barcelona, Prof. Gustavo de Veciana and Yicong Wang

from UT Austin, and collaborators from TUT Finland for the wonderful research experience and ambience via the Intel-Verizon 5G project. Most of the material in this work were refined through the frequent telephonic discussions we had during this project. I would also like to thank my friends, past and current fellow WSIL mates and my UT ECE pals for providing wonderful memories and fun throughout my stay at Austin.

Finally, my self-belief and positive outlook to life stem from the Hindu philosophy. And I am grateful to have been exposed to this ancient Vedic wisdom, the benefits of which I reap everyday.

Kiran Venugopal

The University of Texas At Austin
June 2017

Millimeter Wave Wearable Communication Networks: Analytic Modeling and MIMO Support

Publication No. _____

Kiran Venugopal, Ph.D.
The University of Texas at Austin, 2017

Supervisor: Robert W. Heath, Jr.

Future high-end wearable electronic devices including virtual reality goggles and augmented reality glasses require rates of the order of gigabits-per-second and potentially very low latency. Supporting high data rate wireless connectivity for applications such as uncompressed video streaming among wearable devices in a densely crowded environment is challenging. This is primarily due to bandwidth scarcity when many users operate multiple devices simultaneously. The millimeter wave (mmWave) band has the potential to address this bottleneck, thanks to more spectrum and less interference because of signal blockage at these frequencies. This dissertation addresses key questions that need to be answered before realizing mmWave-based wearables in practice: (i) what are the expected achievable rates in a crowded user environment, with mmWave devices using a given hardware configuration? (ii) how is the wireless connectivity affected in an indoor operation, which is prone to surface reflections? (iii) can multi-stream data transmission, involving large bandwidth communication

under hardware constraints be realized? To answer these, tools from stochastic geometry and compressive sensing, and architectures involving hybrid analog/digital multiple-input multiple-output (MIMO) are leveraged. The main contributions of this dissertation are 1) analytical modeling to compute average achievable rates in mmWave wearable networks consisting of finite number of user devices and human blockages, 2) characterizing the impact of reflections and non-isotropic performance of mmWave wearable networks in crowded indoor environments, 3) channel estimation to support MIMO for wideband mmWave wearable devices using hybrid architecture, and 4) designing optimal, but easy-to-implement, precoding/combining strategies in frequency-selective mmWave systems. Both analysis and numerical simulations show how the proposed evaluation methodology and solutions serve to enable mmWave based communication among next generation wearable electronic devices.

Table of Contents

List of Tables

List of Figures

Chapter 1

Introduction

1.1 Wearables and Body Area Networks

Mobile wearable computing devices are rapidly making inroads due to advancements in miniature electronics fabrication technology, mobile wireless communication, efficient batteries, and increasingly capable data analytics. The major driver of the mobile electronics market has been fitness and health-care gadgets [2,3]. These low-end devices typically require long battery life and only require lower data rate connections to other devices. Recently, a new class of high-end wearable devices is emerging with relaxed power constraints and high data rate requirements.

There are several examples of high-end wearables, such as smartwatches, augmented reality glasses, accurate navigation assists, and virtual reality helmets/goggles. The applications involved may make use of high data rates, and the devices may be charged daily. While these devices could have their own cellular connection, it seems likely that they will instead form a network with a coordinating hub, such as the user's smartphone, creating a *wearable network*. An illustration of a wearable network is shown in Fig. 1.1. A coordinating on-body hub can ensure that interference from wireless devices attached on a given user's body is minimized. Further, the hub can have larger computing power than the other devices in the wearable network and

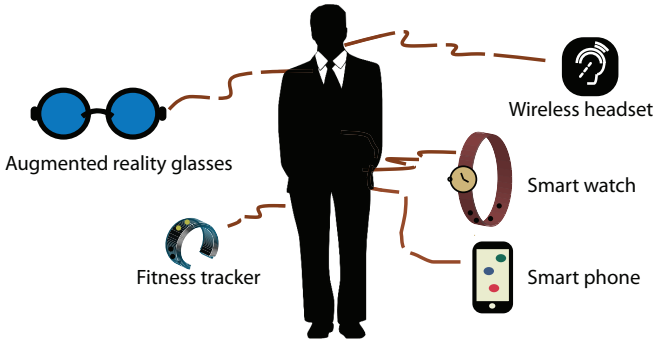

Figure 1.1: Figure showing several mobile wearable devices attached around a user's body. These devices form a wireless network around the user and is termed a wearable network.

be usually connected to wireless hotspots and/or cellular network. Hence, the coordinating hub can act as aggregating nodes to process various sensor data inputs as well as host multimedia contents for infotainment applications in wearable displays.

While the above description of a wearable network may sound similar to Body Area Network (BAN), most work on BANs has focused on low-end devices, especially in man-to-machine communication and health-care [4, 5]. These short-range wireless networks consist of body-surface-mounted electronic devices or in-body implants that transmit data to an on-body or off-body gateway device [6]. The IEEE 802.15.6 standard for the wireless BAN aims to provide low power and highly reliable wireless communication for BANs supporting data rates up to 10 Mbps [7]. These technologies are not feasible for high-end applications like uncompressed video streaming or augmented reality in wearable networks because of the rate requirements of the order of Gbps and the potential for very low latency. Note that the range of operation is not a major concern for these high-end devices in a wearable network, with device-to-device

wireless link lengths usually less than a meter.

Using millimeter wave (mmWave) communication is one approach to provide high data rates in wearable networks [8,9]. The mmWave frequency bands have large bandwidth, good isolation, and better co-existence due to directional antennas. WirelessHD [10] released in 2008 offers multi-gigabit wireless connectivity specifications for the 60 GHz unlicensed mmWave band to support high-definition video and audio digital transmission to replace wired interconnects. Following WirelessHD, IEEE 802.11ad [11] was released and offered several use cases for short range communication systems also at 60 GHz. These standards and other mmWave-based standards like the ECMA-387 and the IEEE 802.15.3c do not explicitly incorporate wearable networks as a use case. The Task Group ay for IEEE 802.11 is now considering mmWave-based high-end wearables in public places as a possible use case. As a consequence, industry is recognizing the importance of millimeter wave for high-end wearables. An illustration of a typical operation among finite-sizes, indoor, mmWave wearable network is shown in Fig. 1.2.

1.2 Finite MmWave Wearable Networks

A key consideration before promoting mmWave for communication in wearable networks is to model and predict the achievable data rates that can be realized in these devices, subject to hardware constraints. MmWave-based networks have been modeled previously using stochastic geometry to study interference and to characterize rate and coverage performance. Models to capture the effect of blockages and directionality of antennas are available in literature, mainly for cellular systems. Most

Figure 1.2: Illustration of a typical crowded indoor scenario such as a train car with several users operating their respective wearable devices.

prior work [12–14] assumed infinite number of devices spread over an infinite area for analytic tractability; these assumptions are also justifiable for outdoor deployments and cellular systems. MmWave wearable networks, however, are likely to have a finite number of users and devices, and located in a finite geographical area.

Analytic models for ad-hoc network with a finite number of devices and spatial extent were considered previously [15,16], but did not include the unique channel and antenna characteristics at mmWave frequencies. Since mmWave wearable networks would involve human users, human bodies are the main source of blockages for the signals and need to be modeled. This also means that the very same users that wear the interfering transmitters act to block other mmWave signals. More work, therefore, is needed to understand the interplay between body blockages and interference, while noting that both the number of users and interfering devices would be finite in number.

1.3 Surface Reflections during Indoor Operations

For crowded indoor operations of wearable networks using mmWave frequencies, modeling reflections from objects, walls and ceiling is critical. This is because mmWave signals suffer less scattering than specular reflections [17]. The reflections not only could help the desired signal (we could leverage the inherent diversity) but also could boost the net interference power. Stochastic models to characterize signal reflections need to be developed to ascertain the feasibility of mmWave wearable networks in indoor operations.

Moreover, the performance seen by a user could be impacted by the non-isotropy in the environment and the presence of restricting boundaries of the enclosed space. Intuitively, the interference pattern seen by the user located at the center of a crowded room is different from that when the user is near a corner. The direction in which the user is facing to could also play a role in dictating the expected data rates given that the user's own body can block/attenuate mmWave signals. Hence, new models need to be developed to better parameterize and understand these features.

1.4 MIMO Channel Estimation at MmWave Frequencies

A key factor to achieving high data rates in mmWave wearable systems is that huge bandwidth is available at these frequencies. Another contributing factor is that larger antenna arrays can be realized that occupy much less device space. To communicate efficiently, channel state information is critical. Given the large size of antenna arrays that are employed, however, channel estimation overhead would be higher, thus reducing the net throughput. Further, hardware restrictions necessitate hybrid

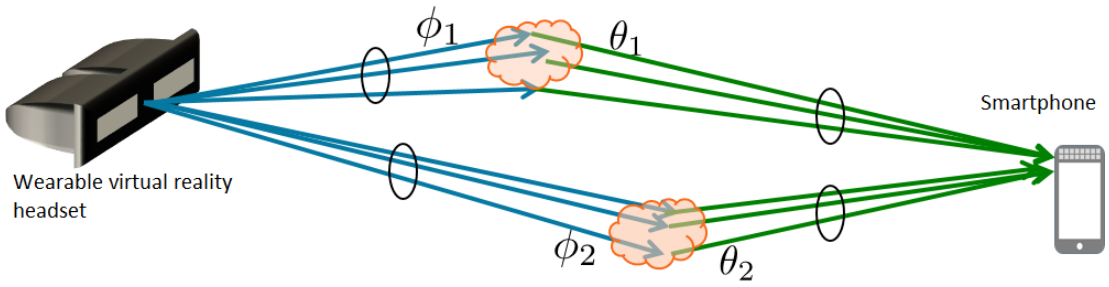

Figure 1.3: Illustration of the sparse mmWave channel between wearable devices.

architectures at the transceivers which restrict the effective number of measurements we can have per channel estimation phase.

Most prior work on mmWave hybrid MIMO channel estimation considered narrowband, frequency-flat channel models. An extension to the wideband, frequency-selective case is not straightforward due practical hardware limitations related to the circuit components. These limitations include the bandlimiting filters and phase shifters used to point the transmissions and receptions. Therefore, methods to enable MIMO channel estimation in hardware-constrained wideband mmWave systems need to be developed to support multi-stream communication and achieve high data rates among wearable devices.

1.5 Wideband MmWave MIMO Precoder Design

Once the channel information is known, developing hybrid MIMO precoders and combiners is the next natural step. Since the mmWave devices will be operating at large system bandwidths, the hybrid precoders and combiners have to operate in these wideband and frequency-selective channels. Prior work in frequency-selective

mmWave hybrid precoding proposed solutions involving different precoders for different narrowband, frequency-flat subcarriers within the wideband system bandwidth. This complicates the hardware design and implementation. For hardware-constrained wearable devices, however, the precoder design must minimize complexity. This motivates the development of low-complexity, easy-to-implement wideband precoding solutions for frequency-selective MIMO mmWave wearable systems.

MmWave channel is sparse in nature with a few multi-paths. An illustration of the sparse structure of the mmWave MIMO channel is shown in Fig. 1.3. This property could be leveraged to transmit and receive signals in the dominant subspace of the channel. This could also potentially simplify the channel state information acquisition used for precoder design. Identifying the key properties of the frequency-selective mmWave channel further is thus necessary to develop new techniques to design optimal precoders and combiners for mmWave wearable devices.

1.6 Overview of Contributions

Enabling mmWave wearable networks required answering the key concerns discussed in Section 1.2 – 1.5. The research presented in this dissertation aims to address these challenges. The primary contributions of this dissertation can be summarized as follows:

1. We propose an analytical framework to model finite sized wearable communication network operating at mmWave frequencies. This framework incorporates human body blockages, antenna parameters and key propagation features of

mmWave communication. Using this model, we derive the exact expression to coverage probability conditioned on the location of the human users and interfering devices. We also analyze spatially averaged rate results in close-form expressions using justifiable assumptions. These results appeared in [1, 18, 19].

2. We develop a tractable model to predict location-dependent performance of mmWave wearable networks in dense indoor operation. This model is used to study the impact of human body orientation and the spatial non-isotropy in the performance. We capture the impact of mmWave signal reflections from walls and ceiling into the analysis to classify interfering devices as strong and weak. The proposed method can be used to design MAC protocols to reduce overhead and improve throughput. These results were published in [20, 21].

3. We propose and analyze efficient channel estimation algorithms for frequency-selective wideband mmWave systems with hybrid architectures. We develop a sparse formulation of the mmWave channel leveraging the channel structure in both the delay and angular domain. Based on this formulation we propose channel estimation algorithms in both and frequency domains. The proposed formulation takes into account various hardware constraints in the system, and appeared in [22, 23].

4. We propose optimal precoders and combiners for frequency-selective mmWave wideband systems. These optimal beamformers are shown to be frequency-flat and easy to implement in practice. We develop the optimal designs leveraging new techniques in subspace estimation, noting that mmWave MIMO channel

matrices corresponding to various subcarriers all belong to the same subspace. These results appeared in [24].

1.7 Notation and Abbreviations

We use the following notation in the rest of the paper: bold uppercase $\mathbf{A}$ is used to denote matrices, bold lower case $\mathbf{a}$ denotes a column vector, and non-bold lower case a is used to denote scalar values. We use $\mathcal{A}$ to denote a set or a region. Further, $||\mathbf{A}||_F$ is the Frobenius norm, and $\mathbf{A}^*$, $\bar{\mathbf{A}}$ and $\mathbf{A}^T$ are the conjugate transpose, conjugate, and transpose of the matrix $\mathbf{A}$. The (i,j)th entry of matrix $\mathbf{A}$ is denoted using $[\mathbf{A}]_{i,j}$. The identity matrix is denoted as $\mathbf{I}$. Further, if $\mathbf{A}$ and $\mathbf{B}$ are two matrices, $\mathbf{A} \circ \mathbf{B}$ is the Khatri-Rao product of $\mathbf{A}$ and $\mathbf{B}$, and $\mathbf{A} \otimes \mathbf{B}$ is their Kronecker product. We use $\mathcal{N}(\mathbf{m}, \mathbf{R})$ to denote a circularly symmetric complex Gaussian random vector with mean $\mathbf{m}$ and covariance $\mathbf{R}$. The determinant of a square matrix $\mathbf{A}$ is denoted as $|\mathbf{A}|$. We use $\mathbb{E}$ to denote expectation. Discrete-time signals are represented as $\mathbf{x}[n]$, with the bold lower case denoting vectors, as before. The frequency domain signals in the kth subcarrier are represented using $\breve{\boldsymbol{x}}[k]$.

1.8 Organization

The rest of this dissertation is organized as follows. In Chapter 2, we propose an analytic model to study finite sized mmWave wearable networks. We then consider the impact of reflections and indoor operation of mmWave wearable network in Chapter 3, and propose a classification of devices in the system as strong and weak interferers. In Chapter 4, we develop explicit MIMO channel estimation

algorithms for wideband mmWave systems using hybrid architecture. This is carried forward further in Chapter 5 wherein optimal frequency-flat precoders and combiners are proposed using the channel knowledge. In this context, we develop subspace estimation techniques to design the optimal beamformers. Finally, concluding remarks and future work directions are presented in Chapter 6.

Chapter 2

Millimeter Wave Device-to-Device Communication in Finite Networks: Interference Modeling and Coverage

2.1 Overview

Emerging applications involving device-to-device communication among wearable electronics require Gbps throughput, which can be achieved by utilizing millimeter wave (mmWave) frequency bands. When many such communicating devices are indoors in close proximity, interference can be a serious impairment. In this chapter[1], we use stochastic geometry to analyze the performance of mmWave networks with a finite number of interferers in a finite network region. Prior work considered either lower carrier frequencies with different antenna and channel assumptions, or a network with an infinite spatial extent. In the mmWave wearable setting, human users not only carry potentially interfering devices, but also act to block interfering signals. Using a sequence of simplifying assumptions, we develop accurate expressions for coverage and rate that capture the effects of key antenna characteristics like

[1]This chapter is based on the work published in the journal paper: K. Venugopal, M. C. Valenti, and R. W. Heath, Jr., "Device-to-Device Millimeter Wave Communications: Interference, Coverage, Rate, and Finite Topologies," IEEE Transactions on Wireless Communications, vol. 15, no. 9, pp. 6175-6188, Sept. 2016. This work was supervised by Prof. Robert Heath. Prof. Matthew C. Valenti gave important ideas for modeling finite networks, Salvatore Talarico gave programming assistance and discussion with Geordie George about antenna gain pattern modeling was insightful.

directivity and gain, and are a function of the finite area and number of users. We validate the assumptions through a combination of analysis and simulation. The main conclusions are that mmWave frequencies can provide Gbps throughput even with omni-directional transceiver antennas, and larger, more directive antenna arrays give better system performance. Importantly, this chapter provides an analytic framework to model device-to-device communication between mmWave wearable devices in a finite space having finite number of interfering wearable sources and human user body blockages.

2.2 Introduction

From a wireless communications perspective, wearable communication networks are the next frontier for device-to-device (D2D) communication [25]. Wearable networks connect different devices in and around the human body including low-rate devices like pedometers and high-rate devices like augmented- or mixed-reality glasses. With the availability of newer commercial products, it seems feasible that many people will soon have multiple wearable devices [26], as illustrated in Fig. 2.1a. Such a wearable network *around* an individual may need to operate effectively in the presence of interference from other users' wearable networks. This is problematic for applications that require Gbps throughput like virtual reality or augmented displays. A typical use case consisting of independent wearable networks collocated in a finite space is illustrated in Fig. 2.1b. Understanding the interference environment is critical to understanding the achievable rate and quality-of-experience that can be supported by wearable communication networks as well as the feasible density of such

(a) Example wearable communication network. The user's smartphone can act as a coordinating hub for the wearable network.

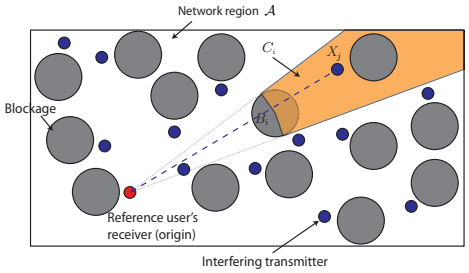

(b) A finite network located, for instance, in a train car. Small circles represent wireless devices and large circles represent blockages. Also shown the concept of a blocking cone C_i, and a blocked interferer $X_j \in C_i$.

Figure 2.1: Many users with wearable networks like those shown in (a) will be located in close proximity as in (b), creating mutual interference. People block some of the interfering signals.

networks.

The millimeter wave (mmWave) band contains a wide range of carrier frequencies capable of supporting short range high-rate wireless connectivity [9]. The mmWave band has several desirable features which include large bandwidth, compatibility with directional transmissions, reasonable isolation, and dense deployability. Standards like Wireless HD [10] and IEEE 802.11ad [11] have already made mmWave-based commercial products a reality. Wearable networks might use these standards or might use device-to-device operating modes proposed for mmWave-based next-generation (5G) cellular systems [27, 28]. Short-range mmWave communication systems usually focus on high-speed wireless connectivity to replace cable connections. However, these emerging protocols have yet to prove their effectiveness in a highly

dense interference scenario.

The tool of stochastic geometry has been extensively used to study interference in large wireless networks [29–32]. Prior work on mmWave-based networks has also used the results from stochastic geometry to analyze coverage and rate [12–14] while modeling the directionality of antennas and the effect of blockages. For analytical tractability, most work assumes an infinite number of mobile devices spread over an infinite area. These assumptions allow the analytical expressions related to the spatial average of the system performance to be simplified through application of Campbell's theorem [33]. Analysis of the outage probability conditioned on the network geometry in ad hoc networks with a finite spatial extent and number of interferers was performed in [15], which was extended to the analysis of frequency-hopping networks in [16]. The unique channel characteristics and antenna features [34] for mmWave networks, however, were not considered in [15, 16]. The mmWave channel has been studied for the outdoor environment [35] and the significant effect of blockages on signal propagation is well known [36]. In crowded environments, human bodies are a main and significant source of blockage of mmWave frequencies [37, 38]. This implies that the very same users that wear the interfering transmitters act to block interference from other wearable networks.

In this chapter, we characterize the performance of mmWave wearable communication networks. We focus on networks operating at mmWave carrier frequencies that are confined to a limited region and containing a finite number of interferers while not explicitly modeling the impact of reflections within the finite region or at its boundaries. We develop an approach for calculating coverage and rate in such a

network. As mmWave systems are likely to use compact antenna arrays, we assess the impact of antenna parameters, in particular the beamwidth and antenna gain, on the coverage and spectral efficiency of the system. Compared with [12–16, 32], we use the same computational approach as in [15, 16], with assumptions on mmWave propagation, antennas, and blockage similar to those in [12, 14], though we model people – not buildings – as blockages. This chapter also considers interferers that are randomly located. We begin by presenting an analysis that leads to closed-form expressions for the coverage probability conditioned on the location of the interferers and blockages. Then, through a sequence of assumptions, we find the spatially averaged coverage and rate when the interference and blockages are drawn from a random point process. The validity of the assumptions and accuracy of the analysis are verified through a set of simulations, which involve the repeated random placement of the users according to the modeled point process.

The organization of the chapter is as follows: We introduce the network topology and signal model in Section 2.3. We describe the interference model and derive expressions for the signal to interference plus noise ratio (SINR) distribution and rate coverage probability in Section 2.4. In Section 2.5, we provide numerical results when the users are located at fixed locations. We assert the simplifying assumptions for analyzing wearable networks when the users are located at random locations in Section 2.6 and, in Section 2.7, verify through simulations that the assumptions have a negligible effect on the accuracy of the analysis. Finally, we conclude this chapter drawing insights from the analysis and simulations in Section 2.8.

2.3 Network Topology and Signal Model

Consider a finite network region $\mathcal{A}$ with a reference receiver and K potentially interfering transmitters. The reference transmitter is assumed to be located at an arbitrary but fixed distance R_0 from the reference receiver at an azimuth angle ϕ_0 and elevation ψ_0. The area of the network in the horizontal plane is denoted by $|\mathcal{A}|$, so that the interferer density $\lambda = K/|\mathcal{A}|$. The interfering transmitters and their locations are denoted by $X_i,\ i = 1,\ 2,\ ...,\ K$. We assume the reference receiver to be located at the origin and represent X_i as a complex number $X_i = R_i e^{j\phi_i}$, where $R_i = |X_i|$ is the distance between the i^{th} transmitter and the receiver, and $\phi_i = \angle X_i$ is the azimuth angle to X_i from the reference receiver. For simplicity, we assume that all the interferers are on the same horizontal plane that contains the reference receiver, though our model could also be easily generalized to handle the 3-D locations of the transmitters. Further, this assumption results in the 2-D blockage model that is elaborated next.

To model human body blockages, we associate each user's body with a circle of diameter W, as illustrated in Fig. 2.1b. These circles as well as the location of their centers are denoted by B_i. Like X_i, B_i is represented as a complex number so that $B_i = |B_i|e^{j\angle B_i}$, where $|B_i|$ is the distance between the center of the i^{th} human body blockage and the receiver, and $\angle B_i$ is the azimuth angle to B_i from the reference receiver. In this blockage model, a transmitter X_i is blocked if the direct path from X_i to the reference receiver goes through the circle associated with any B_j or if X_i falls within the diameter-W circle associated with any blockage B_j. The i^{th} user is associated with both a transmitter X_i and a blockage B_i, and it is possible that

transmitter X_i is blocked by its corresponding blockage B_i. This is called *self-blocking*, a phenomenon that was studied in [38], in the context of 5G mmWave cellular system. If there are no blockages in the path from X_i to the reference receiver, then we say that the path is *line of sight* (LOS); otherwise, we say that it is *non-LOS* (NLOS). We associate different channel parameters with LOS and NLOS paths, accounting for different path-loss and fading models inspired by measurements [39, 40]. In this chapter, we assume that an interferer i is potentially blocked from the reference receiver by $B_j, j \neq i$. Under this assumption that no signal is self-blocked, the following algorithm is used to determine which signals are blocked.

1. Determine $\mathcal{L}$, the set of all transmitters X_i that have no blockages $B_j, j \neq i$ within a distance of $W/2$; i.e.,

$$\mathcal{L} = \left\{ X_i : |X_i - B_j| > \frac{W}{2} \ \forall j \neq i \right\}, \tag{2.1}$$

   where $|X_i - B_j|$ is the distance along the horizontal plane between X_i and B_j.

2. Sort the blockages from closest to most distant, so that $|B_1| \leq |B_2| \leq ... \leq |B_K|$.

3. For each $i \in \{1,\ 2,\ ...,\ K\}$, compute the *blocking cones (wedge in 2D)*[2] C_i as

$$C_i = \left\{ x \in \mathcal{A} : \begin{array}{c} |\angle x - \angle B_i| \leq \arcsin\left(\frac{W}{2|B_i|}\right), \\ |x| > |B_i| \end{array} \right\}.$$

[2]Strictly speaking, a blocking cone is an instance of a truncated cone because it does not extend to the origin.

4. For each $\ell \in \mathcal{L}$, determine if X_ℓ is blocked by checking to see if it lies within any blocking cone; i.e., if

$$\phi_\ell \in \bigcup_{\{i:|B_i|<R_\ell\}} C_i, \tag{2.2}$$

then X_ℓ is blocked.

An illustration of the blocking cone discussed here is shown in Fig. 2.1.

While the antenna gain pattern $G(\phi, \psi)$ is a complicated function of the azimuth angle $\phi \in [-\pi, \pi]$ and the elevation angle $\psi \in \left[-\frac{\pi}{2}, \frac{\pi}{2}\right]$, to facilitate analysis, we use the three-dimensional sectorized antenna model as shown in Fig. 2.2. We characterize the antenna array pattern with four parameters - the half-power beamwidth $\theta^{(\mathsf{a})}$ in the azimuth, the half-power beamwidth $\theta^{(\mathsf{e})}$ in the elevation, antenna gain G within the half-power beamwidths (main-lobe) and gain g outside it (side-lobe). We use the subscript t to denote an antenna parameter for a transmitter and subscript r for the receiver. For example, the main-lobe gain of the transmitter is G_t and that of the receiver is G_r. Similarly, the side-lobe gains are denoted by g_t and g_r. Because the system model and the analysis presented in this chapter are general, substituting the appropriate values for the four parameters G, g, $\theta^{(\mathsf{e})}$ and $\theta^{(\mathsf{e})}$ into the expressions corresponding to the transmitters and the reference receiver enables the rapid evaluation of the SINR distribution. To compare performance in terms of directivity and gain based on practical antennas, we assume that a uniform planar square array (UPA) with half-wavelength antenna element spacing is used at the transmitters and the receiver. The number of antenna elements at the transmitter and receiver are denoted by N_t and N_r, respectively. The antenna gain $G(\phi, \psi)$ of a UPA is modeled

Table 2.1: Antenna parameters of a uniform planar square array

Number of antenna elements	N
Half-power beamwidth, $\theta^{(\mathsf{a})} = \theta^{(\mathsf{e})}$	$\frac{\sqrt{3}}{\sqrt{N}}$
Main-lobe gain G	N
Side-lobe gain g	$\frac{\sqrt{N} - \frac{\sqrt{3}}{2\pi} N \sin\left(\frac{\sqrt{3}}{2\sqrt{N}}\right)}{\sqrt{N} - \frac{\sqrt{3}}{2\pi} \sin\left(\frac{\sqrt{3}}{2\sqrt{N}}\right)}$

as a sectorized pattern as follows. The half-power beamwidths in the azimuth and the elevation are inversely proportional to $\sqrt{N}$ [41]. The main-lobe gain is taken to be N, which is the maximum power gain that can be obtained using N-element antenna array. Note that this is an approximation, though it is possible to design antennas to give near-flat response within the beamwidth with $G \propto N$. The side-lobe gain is then evaluated so that the following antenna equation for constant total radiated power is satisfied [41]

$$\int_{-\pi}^{\pi} \int_{-\frac{\pi}{2}}^{\frac{\pi}{2}} G(\phi, \psi) \cos(\psi) \mathrm{d}\psi \mathrm{d}\phi \quad = \quad 4\pi. \tag{2.3}$$

By using (2.3), we ensure the antenna arrays are passive components. The values for the half-power beamwidths (which are equal in both the azimuth and elevation for UPA), main-lobe and side-lobe gains for an N element (i.e. $\sqrt{N} \times \sqrt{N}$) UPA are given in Table 2.1. When the number of antenna elements is one, we say that the UPA is omni-directional and, hence, the main-lobe and side-lobe gains are unity. This serves as a reference to compare the impact of antenna gain and directivity. As in [12, 13], we assume that each interferer is transmitting with its main-lobe pointed in a random direction.

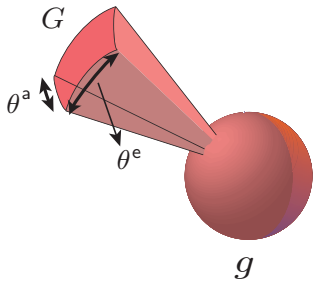

Figure 2.2: Sectorized 3D antenna pattern.

We assume Nakagami fading for the wireless channels so that the power gain h_i due to fading from X_i to the reference receiver is Gamma distributed. We use m_i to denote the Nakagami factor for the link from X_i to the reference receiver, which assumes a value of m_{L} for LOS and m_{N} for NLOS [12]. The path-loss exponent for X_i is denoted as α_i, where $\alpha_i = \alpha_{\mathsf{L}}$ if X_i is LOS and $= \alpha_{\mathsf{N}}$ if it is NLOS. There are different ways to define the signal-to-noise ratio (SNR) in a system with antenna arrays: with and without the antenna gains. We use σ^2 to denote the noise power divided by the reference transmitter power as measured at a reference distance excluding the antenna gains. While σ^2 is inversely proportional the SNR, we intentionally do not include the antenna gains into its computation, so that our results will naturally capture the SNR enhancement that accompanies the use of larger antenna arrays. The transmit power of X_i is denoted as P_i. Each interferer transmits with probability p_{t}, which is determined by the random-access protocol and user activity and is assumed to be the same for all interferers.

We assume that the reference communication link is always LOS. The reference link undergoes Nakagami fading with parameter $m_0 = m_{\mathsf{L}}$ and has path-loss exponent $\alpha_0 = \alpha_{\mathsf{L}}$. Of course, it is possible that the reference user's body itself will create

blockages on the reference link in a wearable network. When this occurs, it can be handled in our model by setting $m_0 = m_{\mathsf{N}}$ and $\alpha_0 = \alpha_{\mathsf{N}}$. Capturing self-blockage of the reference link in a more refined model and incorporating the results into the analysis is an interesting topic for future work.

It is important to note that the boundaries of the finite area are assumed to be impenetrable, so there is no leakage of external interference into the finite area. Further, reflections due to the boundary and objects within the network are not explicitly incorporated in the model. They are accounted for only in a coarse way in the different LOS and NLOS model parameters, which ideally would be determined based on ray tracing or measurement results. The assumption of omitting reflections holds true in many scenarios where the boundaries of the finite area are made of poorly reflecting materials such as concrete or bricks.

2.4 Interference Model

Conditioned on the network (meaning the locations of the transmitters and blockages), we can find the complementary cumulative distribution function (CCDF) of the SINR (also called SINR coverage probability [12]) by adapting the analysis in [15,16]. The analysis that follows in Section 2.4.1 is very general since it can admit the individual interferers to have separate and independent values for the channel parameters - α_i and m_i, and does not require the LOS channel to have values $(\alpha_{\mathsf{L}}, m_{\mathsf{L}})$ and the NLOS channel to have values $(\alpha_{\mathsf{N}}, m_{\mathsf{N}})$. The assumption of fixing the channel parameters of the LOS and NLOS interferers yields tractable analytical expression for spatially averaged SINR coverage probability in Section 2.6.

We define a discrete random variable I_i for $i = \{1, ..., K\}$ that represents the relative power radiated by X_i in the direction of the reference receiver. With probability $(1 - p_{\mathsf{t}})$, X_i does not transmit at all, and hence $I_i = 0$. Otherwise, the relative power will depend on whether or not the random orientation of X_i's antenna is such that the reference receiver is within the main-lobe. We assume a uniform orientation of X_i's antenna, so that the azimuth angle ϕ is uniform in $[0, 2\pi)$ and the elevation angle ψ has a probability density function (pdf) $\frac{1}{2}\cos(\psi)$ in $\left[-\frac{\pi}{2}, \frac{\pi}{2}\right]$. The pdfs can be derived by noting that the surface area element of a unit sphere is $\cos(\psi)\,\mathrm{d}\phi\mathrm{d}\psi$, a function of the elevation angle ψ. Thus the probability that the reference receiver is within the interferer's main-lobe is $\frac{\theta_{\mathsf{t}}^{(\mathsf{a})}}{2\pi}\sin\left(\frac{\theta_{\mathsf{t}}^{(\mathsf{e})}}{2}\right) = p_{\mathsf{M}}$. It follows that

$$I_i \;=\; \begin{cases} 0 & \text{with probability } (1 - p_{\mathsf{t}}) \\ G_{\mathsf{t}} & \text{with probability } p_{\mathsf{t}} p_{\mathsf{M}} \\ g_{\mathsf{t}} & \text{with probability } p_{\mathsf{t}}\,(1 - p_{\mathsf{M}}) \end{cases} . \tag{2.4}$$

Note that a similar approach was used in [16] for modeling adjacent-channel interference in frequency hopping: when the interferer transmitted, one of two power compensations was applied depending on whether the interferer hopped into the same or an adjacent channel. In the wearable network context, we can justify randomizing the orientation angles of the interferers because: (1) the user itself may be randomly moving the orientation of its devices while using them, and (2) the user may have a wearable network with several devices with different orientations and random activity, though we assume the medium access protocol (MAC) of a user's wearable network allows only one of her devices to transmit at a time. It may be noted here that this kind of wearable network is still under development, so the exact MAC protocol has

not yet been decided. We make a reasonable assumption that the network of a given user is coordinated such that only one device transmits at a time, while the devices of different users are not so coordinated and can therefore collide.

Now, let us define the normalized power gain from X_i to be

$$\Omega_i \;=\; \begin{cases} \frac{P_i}{P_0} G_{\mathsf{r}} R_i^{-\alpha_i} & \text{if } -\frac{\theta_{\mathsf{r}}^{(\mathsf{a})}}{2} \le \phi_i - \phi_0 \le \frac{\theta_{\mathsf{r}}^{(\mathsf{a})}}{2} \\ \frac{P_i}{P_0} g_{\mathsf{r}} R_i^{-\alpha_i} & \text{otherwise} \end{cases}, \tag{2.5}$$

where $\alpha_i = \alpha_{\mathsf{N}}$ if X_i is NLOS and $\alpha_i = \alpha_{\mathsf{L}}$ if X_i is LOS. This is the worst-case situation when $|\psi_0| \le \frac{\theta_{\mathsf{r}}^{(\mathsf{e})}}{2}$. If $|\psi_0| > \frac{\theta_{\mathsf{r}}^{(\mathsf{e})}}{2}$, we have $\Omega_i = \frac{P_i}{P_0} g_{\mathsf{r}} R_i^{-\alpha_i}$, $\forall\ i$ which is a simpler trivial case. For the rest of the chapter, we assume the non-trivial worst case and all the analysis presented hereafter extends easily for the trivial case. The SINR is

$$\gamma \;=\; \frac{G_{\mathsf{t}} h_0 \Omega_0}{\sigma^2 + \sum_{i=1}^{K} I_i h_i \Omega_i}, \tag{2.6}$$

where $\Omega_0 = G_{\mathsf{r}} R_0^{-\alpha_0}$ is the normalized power gain from the reference transmitter, as we assume the reference transmitter is always within the main beam of the reference receiver. The effect of misalignment of beam in the reference link was considered at lower frequencies (e.g. UHF) in prior work [42, 43]. In the wearable communication network context, however, since the distance of the reference link is short relative to the beamwidth of the antenna, pointing errors will not seriously degrade performance. (For instance, with our sectorized antenna model, the beam could be off by half the beamwidth without changing performance.)

2.4.1 Coverage Probability

Denoting $\mathbf{\Omega} = [\Omega_0, ..., \Omega_K]$, the coverage probability $P_{\mathsf{c}}(\beta, \mathbf{\Omega})$ for a given $\mathbf{\Omega}$ is defined as the CCDF of the SINR evaluated at a threshold β and is given by

$$P_{\mathsf{c}}(\beta, \mathbf{\Omega}) = \mathbb{P}\left[\gamma > \beta | \mathbf{\Omega}\right]. \tag{2.7}$$

Substituting (2.6) into (2.7) and rearranging leads to

$$P_{\mathsf{c}}(\beta, \mathbf{\Omega}) = \mathbb{P}\left[\mathsf{S} > \sigma^2 + \sum_{i=1}^{K} \mathsf{Y}_i \;\middle|\; \mathbf{\Omega}\right], \tag{2.8}$$

where $\mathsf{S} = \beta^{-1} G_{\mathsf{t}} h_0 \Omega_0$, and $\mathsf{Y}_i = I_i h_i \Omega_i$. Conditioned on $\mathbf{\Omega}$, let $f_{\mathbf{Y}}(\mathbf{y})$ denote the joint pdf of $(\mathsf{Y}_1, ..., \mathsf{Y}_K)$ and $f_{\mathsf{S}}(s)$ denote the pdf of S. Then, (2.8) can be written as

$$P_{\mathsf{c}}(\beta, \mathbf{\Omega}) = \int_{\mathbb{R}^K} ... \int \left(\int_{\sigma^2 + \sum_{i=1}^{K} y_i}^{\infty} f_{\mathsf{S}}(s) \mathrm{d}s \right) f_{\mathbf{Y}}(\mathbf{y}) \mathrm{d}\mathbf{y}. \tag{2.9}$$

Defining $\beta_0 = \beta m_0 / G_{\mathsf{t}} \Omega_0$ and assuming that m_0 is a positive integer, the random variable S is gamma distributed with pdf given by

$$f_{\mathsf{S}}(s) \;\; = \;\; \frac{(\beta_0)^{m_0}}{(m_0 - 1)!} s^{m_0 - 1} e^{-\beta_0 s}, \;\; s \geq 0. \tag{2.10}$$

Using (2.10), the right hand side of (2.9) evaluates to

$$\sum_{\ell=0}^{m_0 - 1} \int_{\mathbb{R}^K} ... \int \frac{e^{-\beta_0 (\sigma^2 + \sum_{i=1}^{K} y_i)}}{\ell! (\beta_0 \sigma^2)^{-\ell}} \left(1 + \frac{1}{\sigma^2} \sum_{i=1}^{K} y_i \right)^{\ell} f_{\mathbf{Y}}(\mathbf{y}) \mathrm{d}\mathbf{y}. \tag{2.11}$$

Using the binomial theorem followed by multinomial expansion,

$$\left(1 + \frac{1}{\sigma^2} \sum_{i=1}^{K} y_i \right)^{\ell} = \sum_{t=0}^{\ell} \binom{\ell}{t} \frac{t!}{\sigma^{2t}} \sum_{\mathcal{S}_t} \left(\prod_{i=1}^{K} \frac{y_i^{t_i}}{t_i!} \right), \tag{2.12}$$

where the last summation is over the set $\mathcal{S}_t$ containing all length-K non-negative integer sequences $\{t_1, \ldots, t_K\}$ that sum to t. This can be pre-computed and saved as a matrix as explained in [15]. Given $\mathbf{\Omega}$, the $\{\mathsf{Y}_i\}_{i=1}^K$ are independent. So, $f_{\mathbf{Y}}(\mathbf{y})$ may be written as $\prod_{i=1}^K f_{\mathsf{Y}_i}(y_i)$, where

$$f_{\mathsf{Y}_i}(y_i) = (1-p_{\mathsf{t}})\,\delta(y_i) + p_{\mathsf{t}} \left(\frac{m_i}{\Omega_i}\right)^{m_i} \frac{y_i^{m_i-1}}{\Gamma(m_i)} \left[p_{\mathsf{M}} \frac{e^{-\frac{m_i y_i}{G_{\mathsf{t}}\Omega_i}}}{G_{\mathsf{t}}^{m_i}} + (1-p_{\mathsf{M}})\,\frac{e^{-\frac{m_i y_i}{g_{\mathsf{t}}\Omega_i}}}{g_{\mathsf{t}}^{m_i}}\right] u(y_i), \tag{2.13}$$

$\delta(y_i)$ is the Dirac delta function, and $u(y_i)$ is the unit step function. Substituting (2.12) into (2.11) and utilizing the independence of the $\{\mathsf{Y}_i\}$, (2.9) may be written as

$$P_{\mathsf{c}}(\beta, \mathbf{\Omega}) = \sum_{\ell=0}^{m_0-1} \frac{(\beta_0\sigma^2)^\ell}{\ell! e^{\beta_0\sigma^2}} \sum_{t=0}^{\ell} \binom{\ell}{t} \frac{t!}{\sigma^{2t}} \sum_{\mathcal{S}_t} \left(\prod_{i=1}^K \mathcal{G}_{t_i}(\Omega_i)\right), \tag{2.14}$$

where

$$\mathcal{G}_{t_i}(\Omega_i) = (1-p_{\mathsf{t}})\,\delta[t_i] + p_{\mathsf{t}} \left(\frac{\Omega_i}{m_i}\right)^{t_i} \frac{\Gamma(m_i+t_i)}{t_i!\Gamma(m_i)} \left[p_{\mathsf{M}} \mathcal{Q}_{t_i}(G_{\mathsf{t}}) + (1-p_{\mathsf{M}})\,\mathcal{Q}_{t_i}(g_{\mathsf{t}})\right]. \tag{2.15}$$

In (2.15), $\delta[t_i]$ is the function defined as

$$\delta[t_i] = \begin{cases} 1 & \text{if } t_i = 0 \\ 0 & \text{if } t_i \neq 0 \end{cases} \tag{2.16}$$

$$\text{and} \quad \mathcal{Q}_{t_i}(x) = x^{t_i} \left(1 + \frac{\beta_0 x \Omega_i}{m_i}\right)^{-(m_i+t_i)}. \tag{2.17}$$

The assumption of an integer value for m_0 is key to the derivation of the exact expression for the SINR coverage probability in (2.14). When m_0 is not an integer, such an exact evaluation is not possible to the best of our knowledge. Only an upper-bound using the results from [44] can be obtained for a general real-valued m_0.

2.4.2 Ergodic Spectral Efficiency

When the SINR is β, the spectral efficiency in bits per channel use is

$$\eta \;=\; \log_2(1+\beta). \tag{2.18}$$

The CCDF of the spectral efficiency is found by defining the equivalent events

$$\{\gamma > \beta \mid \mathbf{\Omega}\} \;\Leftrightarrow\; \underbrace{\{\log_2(1+\gamma) > \eta \mid \mathbf{\Omega}\}}_{\{\gamma > 2^\eta - 1 \mid \mathbf{\Omega}\}}. \tag{2.19}$$

The event on the left corresponds to the coverage probability $P_{\mathsf{c}}(\beta, \mathbf{\Omega})$, while the event on the right corresponds to the CCDF of the spectral efficiency, $P_\eta(\eta, \mathbf{\Omega})$, also called the *rate coverage probability* for a given $\mathbf{\Omega}$. Since equivalent, the two events have the same probability, and it follows that

$$P_\eta(\eta, \mathbf{\Omega}) \;=\; P_{\mathsf{c}}\left(2^\eta - 1, \mathbf{\Omega}\right). \tag{2.20}$$

See also Lemma 5 of [12].

Using the fact that, for a non-negative X, $\mathbb{E}[X] = \int_0^\infty (1 - F(x))\mathrm{d}x$ (see (5-33) in [45]), the *ergodic spectral efficiency* conditioned on $\mathbf{\Omega}$ can be found from

$$\mathbb{E}[\eta] = \frac{1}{\log(2)} \int_0^\infty \frac{P_{\mathsf{c}}\left(\beta, \mathbf{\Omega}\right)}{1+\beta} \mathrm{d}\beta, \tag{2.21}$$

where the last step uses the change of variables $\beta = 2^\eta - 1 \rightarrow \mathrm{d}\eta = \frac{1}{\log(2)} \mathrm{d}\beta/(1+\beta)$.

In practice, there is a maximum and minimum rate, and hence, a maximum and minimum SINR thresholds β_{max} and β_{min}, respectively. This maximum may be imposed by the modulation order of the constellation used and distortion limits in

Table 2.2: Antenna Parameters

Number of antenna elements	1	4	16
Half-power beamwidth (in degrees)	360	49.6	24.8
Main-lobe gain (in dB)	0	6	12
Side-lobe gain (in dB)	0	-0.8839	-1.1092

the RF front end while minimum due to the receiver sensitivity. In this case, the limits of the integral are β_{min} and β_{max}, and

$$\mathbb{E}[\eta] \;=\; \int_{\beta_{\mathsf{min}}}^{\beta_{\mathsf{max}}} \frac{P_{\mathsf{c}}\left(\beta, \mathbf{\Omega}\right)}{\log(2)(1+\beta)} \mathrm{d}\beta. \tag{2.22}$$

The quickest way to compute (2.22) is to simply compute $P_{\mathsf{c}}\left(\beta, \mathbf{\Omega}\right)$ for a finely spaced β and then use the trapezoidal rule to numerically solve the integral.

2.5 Numerical Results for Fixed Geometry

In this section, we provide numerical results for coverage probability and ergodic spectral efficiency. The users are located at fixed locations, but to enable a comparison against random topologies (see Section 2.7), their placement is confined to an annulus $\mathcal{A}$ having inner radius r_{in} and outer radius r_{out}. Conditioned on the fixed locations of the interferers and the blockages, the exact expression for the SINR coverage probability can be derived using (2.14). We assume there are K interfering transmitters, neglect self-blocking, and assume that the blockage and transmitter associated with each user are co-located; i.e., $B_i = X_i$ for each i. It is assumed that the P_i are all the same; i.e., all transmitters transmit at the same power.

The values of the antenna half-power beamwidths, main-lobe and side-lobe gains are summarized in Table 2.2. Note that it is possible to get desired side-lobe

Table 2.3: Parameters used to obtain numerical results for fixed geometry

Parameter	Value	Description
R_0	0.3 m	Reference link length
ϕ_0, ψ_0	0^o	Reference receiver antenna main-lobe orientation
m_{L}	4	Nakagami parameter for LOS link
m_{N}	2	Nakagami parameter for NLOS link
α_{L}	2	Path-loss exponent for LOS link
α_{N}	4	Path-loss exponent for NLOS link
W	0.3 m	Width of the human-body blockages
σ^2	-20 dB	Normalized noise power
K	36	Number of potential interferers

isolation by carefully designing the array response via windowing similar to filter design [41]. This would also add complexity to the array design and configuration. Since power and heating issues are critical for wearable devices, it is yet to be determined if such techniques would indeed be considered in future gadgets. To quantify the effect of antenna directivity and as an example, we chose a uniform planar array described in Table 2.1. The network and signal parameters used to obtain the results in this section are summarized in Table 2.3. The Nakagami parameters and the path-loss exponents assumed are the ones used in [12]. For simplicity and to ensure the interferers are uniformly spread out in the network region, we let the user locations to be on a $n \times n$ square lattice restricted to the annulus $\mathcal{A}$. The network region under this assumption is shown in Fig. 2.3a where the 7×7 grid locations and the user locations in the network region $\mathcal{A}$ are shown. We let the minimum distance of two nodes in the grid be $2R_0$. For example, when the lattice points are separated by 0.6 m ($R_0 = 0.3$ m as in Table 2.3) and $n = 7$, we get $K = 36$ with $r_{\mathsf{in}} = 0.3$ m and $r_{\mathsf{out}} = 2.1$ m, which corresponds to an interferer density $\lambda = 2.25$ (passengers/m^2),

a typical density scenariothat approximates the peak-hour passenger load in urban train cars [46].

Fig. 2.3 shows users placed according to Fig. 2.3a along with the blocking cones (Fig. 2.3b) assuming that each user is associated with a blockage of width $W = 0.3$ m. The blocked users are indicated by filled circles. We next provide numerical results for this fixed geometry. The dependence of coverage probability on the transmission probability $p_{\mathtt{t}}$ of the interferers for a fixed transmitter and receiver antenna array configuration is shown in Fig. 2.4 for the case when the transmitters and the receiver use omni-directional antenna. It is seen that, as expected, a higher value of $p_{\mathtt{t}}$ leads to lower coverage probability for a given SINR threshold. We observe similar results for other antenna configurations as well. The CCDF of spectral efficiency for different antenna configurations is shown in Fig. 2.5 for a given random-access probability. Here we let $p_{\mathtt{t}} = 1$. Clearly, using more antennas at the transmitters and the receiver results in significant improvement in the rate. This is because larger antenna arrays provide more directed transmission and reception, thus improving the SINR due to the increased antenna gains of the reference link as well as the reduced beamwidth of the interfering receivers, which reduces the likelihood that the reference receiver falls within a randomly oriented receiver's main-lobe. The ergodic spectral efficiency for various antenna configurations when $p_{\mathtt{t}} = 1$ is summarized in Table 2.4. It can be seen that having larger N_{t} is more advantageous than having a larger N_{r} for the fixed geometry considered in this section. We attribute the asymmetric behavior with respect to N_{t} and N_{r} in Table 2.4 to the fact that the interferers have smaller probability of pointing their main-lobes to the reference receiver when N_{t} is large.

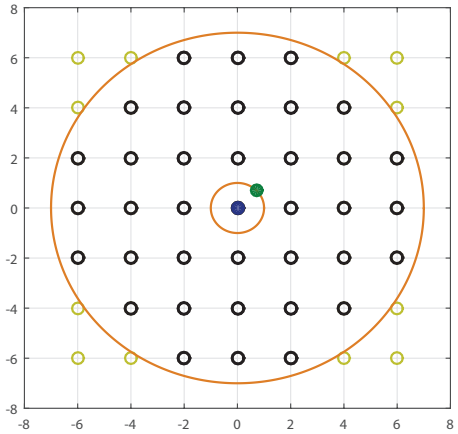

(a) The locations of the users in a uniform grid of size 7×7 restricted to an annulus. The twelve users located outside the circle are deleted from the network.

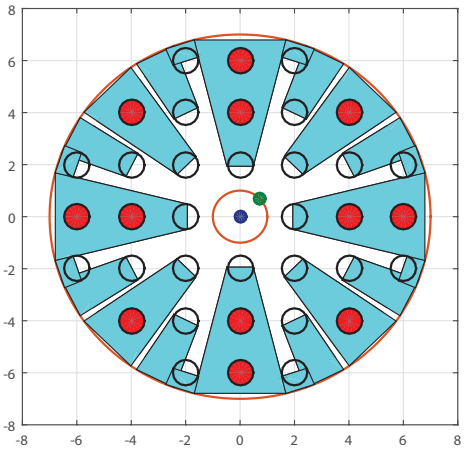

(b) The blocking cones associated with the blockages and the blocked users (filled circles).

Figure 2.3: The fixed geometry considered in Section 2.5 and the blocking cones associated with the users. The reference receiver and the projection of the transmitter onto $\mathcal{A}$ are shown in blue and green, respectively.

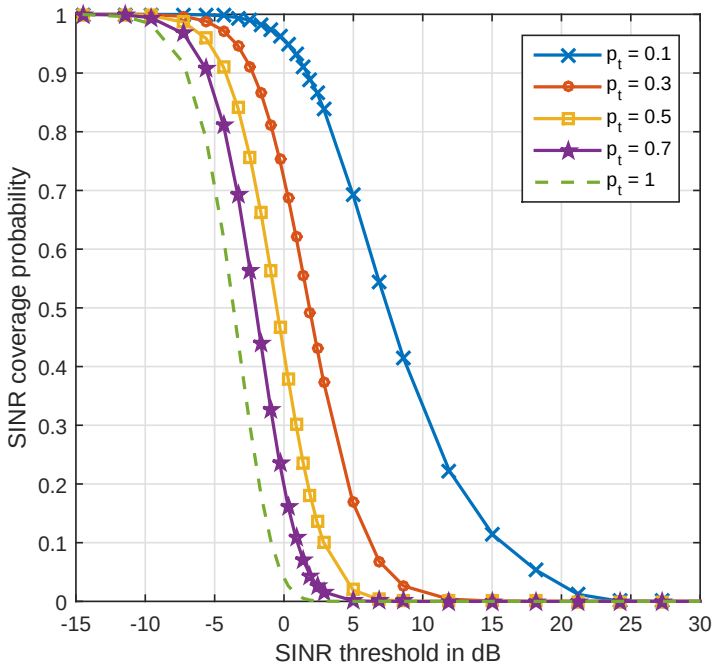

Figure 2.4: SINR coverage probability when the users are placed in the fixed positions indicated in Fig. 2.3a for different transmission probabilities p_{t}, with $N_{\mathrm{t}} = N_{\mathrm{r}} = 1$. Larger p_{t} results in smaller coverage probability.

Table 2.4: Ergodic spectral efficiency for various antenna configurations

N_{t} \ N_{r}	1	4	16
1	0.1762	0.8710	1.5481
4	1.0880	2.3282	3.2820
16	2.6734	4.2190	5.2850

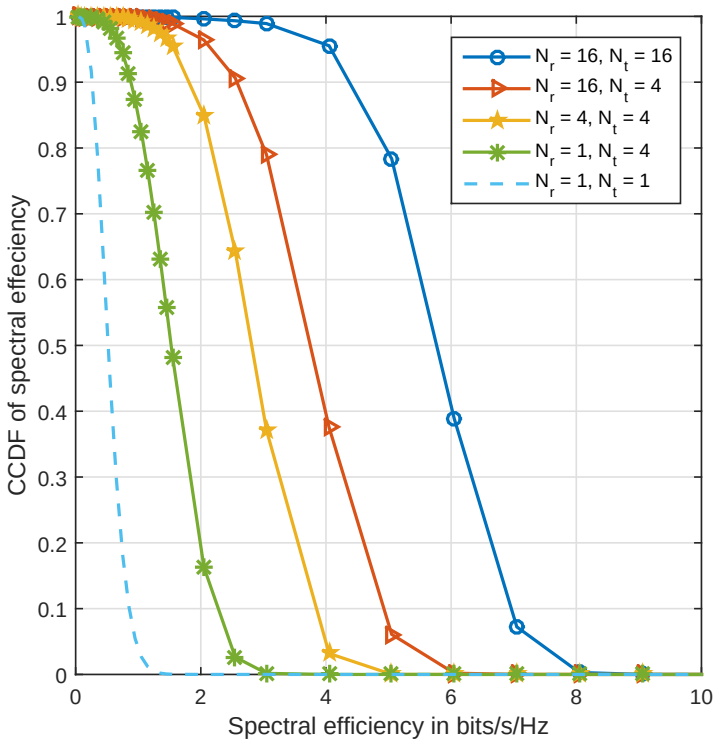

Figure 2.5: CCDF of spectral efficiency for different antenna configurations when $p_{\mathrm{t}} = 1$ and the fixed network geometry in Fig. 2.3a. Spectral efficiency is improved significantly with more antennas.

2.6 Spatial Averaging for Random Geometries

Infinite-sized networks are usually analyzed by assuming the interferers are drawn from a point process, then determining the coverage and rate of a typical user by averaging over the network geometry. Intuitively, this can be thought of as the performance seen by a user that wanders throughout the network, and thus sees many different network topologies. In this section, we outline the approach we take to analyze the interference in a finite sized mmWave-based device-to-device network when the users are located at random locations. While in reality, users are generally spaced far enough apart that their bodies don't overlap, for mathematical tractability we assume that the users are independently placed (which include cases with overlaps).

The spatially averaged CCDF of the SINR can be derived by taking the expectation of $P_{\mathsf{c}}(\beta, \mathbf{\Omega})$ ((2.14) in Section 2.4) with respect to $\mathbf{\Omega}$

$$P_{\mathsf{c}}(\beta) = \mathbb{P}[\gamma > \beta] = \mathbb{E}_{\mathbf{\Omega}}[P_{\mathsf{c}}(\beta, \mathbf{\Omega})]. \tag{2.23}$$

This can be performed in two ways: (1) through the use of simulation, and (2) analytically. In the former method, we can determine the coverage and rate as follows. We randomly place the K potentially interfering users drawn from a binomial point process (BPP) and compute the corresponding coverage and rate for each network realization. This is repeated a large number of times to obtain the spatial average. While in the limit of an infinite number of trials, this approach provides the exact spatially averaged performance, the downside is that it is computationally expensive to obtain. The second method is similar to the approach in [47], which however only

considered Rayleigh fading for the links. The spatially averaged outage probability is found in this approach by unconditioning the results we obtained in Section 2.4 that were conditioned on the location of the interferers and the blockages. Using this approach, we develop closed-form expression for the spatially averaged CCDF of the SINR, which is then validated against the results obtained via simulation.

2.6.1 Assumptions

Taking the expectation is complicated by a number of factors that arise primarily due to the coupling of interferers and blockages, since each user is not only a potential source of interference, but is also a potential source of blockage. To make the problem more tractable, we adopt a sequence of assumptions, with each assumption building upon the previous one. Simulation results show the validity of the assumptions.

Assumption 1: **The locations of the blockages and interferers are related by an orbital model.** Even if a user B_i (which also denotes blockage) is in a fixed location, its transmitter X_i could be randomly positioned around it. Hence, we specify the location of X_i in the 2-D plane relative to B_i by placing it randomly on a circle of radius $d > W/2$ and center B_i. Self-blocking is now inherent in the model, i.e., if X_i is behind B_i, then it is blocked. We refer to this model as the *orbital model*. This is illustrated in Fig. 2.6.

Assumption 2: **The locations of the blockages and interferers are drawn from independent point processes.** Though this assumption is not by itself that useful, it is a stepping stone towards a tractable analysis. With this as-

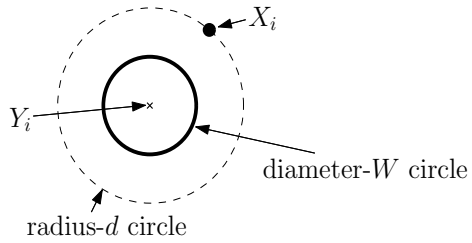

Figure 2.6: An illustration of the orbital model with the locations of blockage B_i and the interferer X_i.

sumption we can still obtain the corresponding coverage and rate using the aforementioned simulation, only now the simulation can lay out K interferers and K blockers independently.

Assumption 3: **The blockage states of the interferers are independent.** This assumes that there is no correlation in the blockage process, even though in reality a transmitter that is close to a blocked transmitter is likely to also be blocked. With this assumption we first determine the blockage probability $p_{\mathsf{b}}(r)$, which gives the probability of blockage arising from other users as a function of distance r to the reference receiver. We can determine $p_{\mathsf{b}}(r)$ either empirically (through running simulations of the blockage process) or by using results from random shape theory [36]. Then, having established $p_{\mathsf{b}}(r)$, we run a new simulation whereby we first place the interferers according to a BPP, then we independently mark each interferer as being blocked with probability $p_{\mathsf{b}}(r)$. Note that now, we need not place the blockages in the simulation.

Assumption 4: **All interferers beyond some distance r_{B} are NLOS and those closer than r_{B} are LOS.** Here, we replace the irregular and random LOS boundary with an equivalent ball. The value of r_{B} can be found by matching the

first moments (Criterion 1 of [12]), or alternatively, it could be found by matching the average rate.

2.6.2 Analysis of Blocking Probability

Lemma 1 *When the network region $\mathcal{A}$ is an annulus with inner radius r_{in} and outer radius r_{out} and blockages have diameter W, the probability that an interferer at distance r from the reference receiver is blocked by any of the K blockages that are independently and uniformly distributed over $\mathcal{A}$ is*

$$p_{\mathsf{b}}(r) = \begin{cases} 1 - \left(1 - \frac{rW + \frac{\pi W^2}{8} - \mu}{|\mathcal{A}|}\right)^K & \text{if } r_{\mathsf{in}} \le r \le r_{\mathsf{out}} - \frac{W}{2} \\ 1 - \left(1 - \frac{rW - \mu + \nu}{|\mathcal{A}|}\right)^K & \text{if } r_{\mathsf{out}} - \frac{W}{2} \le r \le r_{\mathsf{out}} \end{cases}$$

where

$$\mu = \frac{W}{2}\sqrt{{r_{\mathsf{in}}}^2 - \left(\frac{W}{2}\right)^2} + {r_{\mathsf{in}}}^2 \arcsin\left(\frac{W}{2r_{\mathsf{in}}}\right) \text{ and}$$

$$\nu = \begin{cases} \left(\frac{W}{2}\right)^2 \arcsin\left(\frac{{r_{\mathsf{out}}}^2 - \left(\frac{W}{2}\right)^2 - r^2}{rW}\right) + \\ {r_{\mathsf{out}}}^2 \arccos\left(\frac{{r_{\mathsf{out}}}^2 - \left(\frac{W}{2}\right)^2 + r^2}{2rr_{\mathsf{out}}}\right) - \\ 2\sqrt{s(s-r)(s-\frac{W}{2})(s-\frac{r_{\mathsf{out}}}{2})} \end{cases}$$

with $s = \frac{r_{\mathsf{out}} + r + W/2}{2}$.

Proof: The blockages are drawn from a BPP. Consider a transmitter X_i located at distance $|X_i| = r$ from the reference receiver. Its signal will be blocked if there is a blockage inside a certain subregion of $\mathcal{A}$, which we will call the *blocking region* of X_i (i.e., X_i is blocked if there is an object in its blocking region). Since $\mathcal{A}$ is a circular disk with inner radius r_{in} and outer radius r_{out}, the blocking region looks like Fig. 2.7a if $r_{\mathsf{in}} \le r \le r_{\mathsf{out}} - \frac{W}{2}$ and like Fig. 2.7b if $r_{\mathsf{out}} - \frac{W}{2} < r \le r_{\mathsf{out}}$.

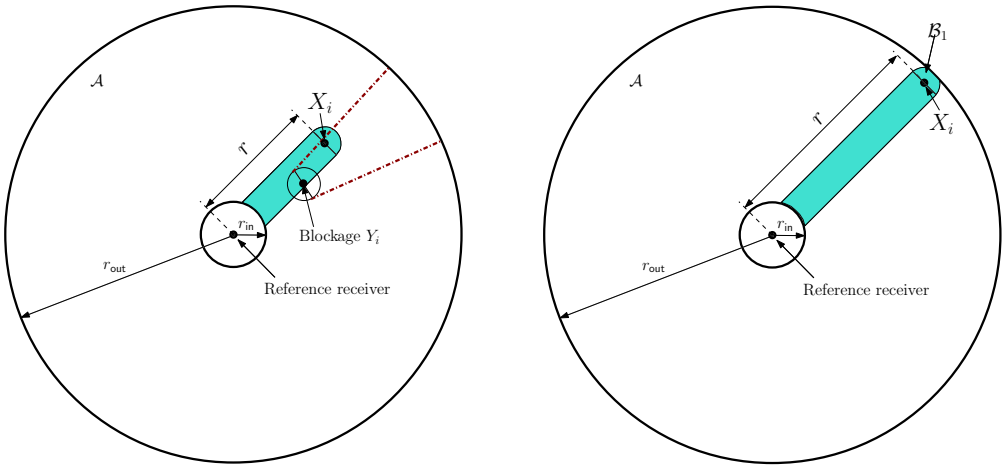

(a) Case when $r_{\mathsf{in}} \leq r \leq r_{\mathsf{out}} - \frac{W}{2}$ (b) Case when $r_{\mathsf{out}} - \frac{W}{2} < r \leq r_{\mathsf{out}}$

Figure 2.7: Figure showing the blocking region for interferer X_i with $|X_i| = r$ for two different cases. The blocking cone of a blockage B_i of diameter W that lies within the blocking region of X_i is also shown for illustration

Let $p_{\mathsf{b}}(i,j)$ be the probability that blockage B_j blocks transmitter X_i with $|X_i| = r$. Since the blockages are placed uniformly at random, the probability that the blockage is inside the blocking region is equal to the ratio of the area of the corresponding blocking region and the overall network. For $r_{\mathsf{in}} \leq r \leq r_{\mathsf{out}} - \frac{W}{2}$, the area of the blocking region can be evaluated as follows. The area can be split into regions as shown in Fig. 2.8, where region $\mathcal{A}_1$ is a sector of the circle with radius r_{in} and subtended angle $\psi = 2\arcsin\frac{W}{2r_{\mathsf{in}}}$. Region $\mathcal{A}_2$ corresponds to two identical right triangles with base length $W/2$ and height $\sqrt{r_{\mathsf{in}}^2 - \left(\frac{W}{2}\right)^2}$ and region $\mathcal{A}_3$ is a semicircular disk of radius $W/2$. Hence, the area of the shaded region in Fig. 2.7a is $rW + \frac{\pi W^2}{8} - |\mathcal{A}_1| - 2|\mathcal{A}_2|$, where $|\mathcal{A}_2| = \frac{W}{4}\sqrt{{r_{\mathsf{in}}}^2 - \left(\frac{W}{2}\right)^2}$ and $|\mathcal{A}_1| = {r_{\mathsf{in}}}^2 \arcsin\left(\frac{W}{2r_{\mathsf{in}}}\right)$. For the two cases shown in Fig. 2.7, we would then have

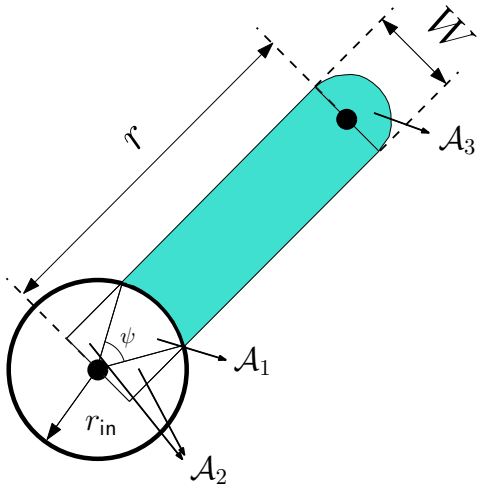

Figure 2.8: Evaluation of area of blocking region for $r_{\mathsf{in}} \leq r \leq r_{\mathsf{out}} - \frac{W}{2}$

$$p_{\mathsf{b}}(i,j) = \begin{cases} \frac{rW - |\mathcal{A}_1| - 2|\mathcal{A}_2| + \frac{\pi W^2}{8}}{|\mathcal{A}|} & \text{if } r_{\mathsf{in}} \leq r \leq r_{\mathsf{out}} - \frac{W}{2} \\ \frac{rW - |\mathcal{A}_1| - 2|\mathcal{A}_2| + \nu}{|\mathcal{A}|} & \text{if } r_{\mathsf{out}} - \frac{W}{2} \leq r \leq r_{\mathsf{out}} \end{cases}$$

where ν, as defined in Lemma 1, is the area of region $\mathcal{B}_1$ indicated in Fig. 2.7b. Since the blockages are independent, the transmitter will be blocked if there are *any* blockages — or, equivalently, will not be blocked only if there are no blockages in its blocking region, Thus, the probability that X_i located at $|X_i| = r$ is blocked is

$$p_{\mathsf{b}}(r) \;\; = \;\; 1 - \prod_{j=1}^{K} \left(1 - p_{\mathsf{b}}(i,j)\right), \tag{2.24}$$

resulting in the form given in Lemma 1. □

The distance-dependent blockage probability $p_{\mathsf{b}}(r)$ is shown for an annulus of inner radius $r_{\mathsf{in}} = 1$ and outer radius $r_{\mathsf{out}} = 7$ in Fig. 2.9 along with that obtained via simulation. The simulation results closely match the analytical approximations derived using Assumptions 1-3. Also, as expected, the probability that an interferer

is blocked increases as the distance r between the interferer and the reference receiver is increased. The dependence of $p_{\mathsf{b}}(r)$ on K, the number of interferers is shown when $W = 1$ in Fig. 2.9a and the dependence on the width of the blockages W is shown when $K = 36$ in Fig. 2.9b. It is seen that with larger values for K and W the blockage probability is more for any given distance r from the reference receiver.

To evaluate r_{B} under Assumption 4, we compute the mean number of interferers that are not blocked as

$$\rho \;=\; 2\pi \frac{K}{|\mathcal{A}|} \int_{r_{\mathsf{in}}}^{r_{\mathsf{out}}} (1 - p_{\mathsf{b}}(r))\, r \mathrm{d}r. \tag{2.25}$$

Equating this average number of non-blocked interferers to the number of interferers in an equivalent LOS ball of radius r_{B} leads to the expression

$$r_{\mathsf{B}} \;=\; \left(2 \int_{r_{\mathsf{in}}}^{r_{\mathsf{out}}} (1 - p_{\mathsf{b}}(r))\, r \mathrm{d}r + {r_{\mathsf{in}}}^2 \right)^{0.5}. \tag{2.26}$$

Now $p_{\mathsf{b}}(r)$ is approximated by $\tilde{p}_{\mathsf{b}}(r)$, which is a step function with a step up at distance r_{B},

$$\tilde{p}_{\mathsf{b}}(r) = \begin{cases} 0 & \text{if } r_{\mathsf{in}} \leq r \leq r_{\mathsf{B}} \\ 1 & \text{if } r_{\mathsf{B}} < r \leq r_{\mathsf{out}} \end{cases}. \tag{2.27}$$

2.6.3 Analysis of Coverage Probability

Under assumptions 1 – 4, we can derive the probability distribution of $f_{\Omega_i}(w)$ of Ω_i which are now independent random variables that depend on the location of X_i for $\{1,\ 2, ...,\ K\}$ as follows

$$\Omega_i = \mathfrak{g}_1(\phi_i) R_i^{-\mathfrak{g}_2(R_i)}, \tag{2.28}$$

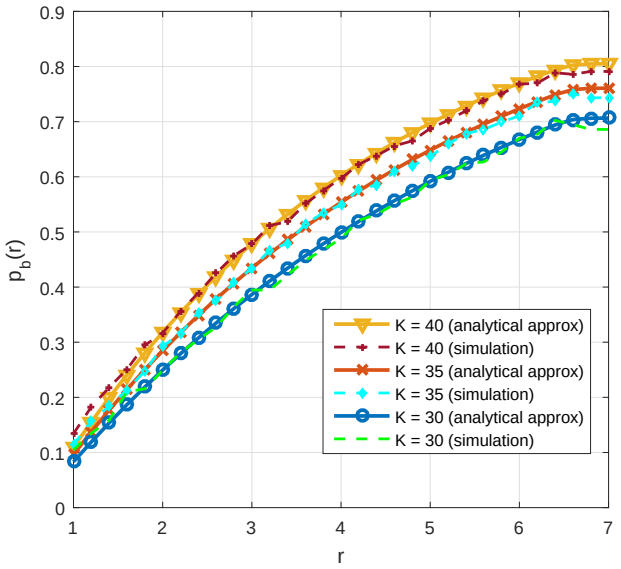

(a) $p_{\mathsf{b}}(r)$ vs r for different values of K when $W = 1$.

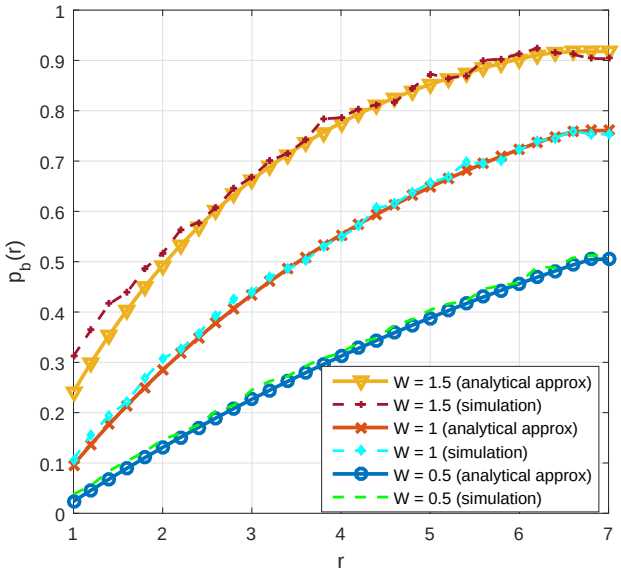

(b) $p_{\mathsf{b}}(r)$ vs r for different values of W when $K = 36$.

Figure 2.9: The distance-dependent blockage probability as K and W are varied. Here we assume $r_{\mathsf{in}} = 1$ and $r_{\mathsf{out}} = 7$.

where

$$\mathfrak{g}_1(\phi_i) = \begin{cases} a_i & \text{if } |\phi_i - \phi_0| \leq \frac{\theta_{\mathsf{r}}^{(\mathsf{a})}}{2} \\ b_i & \text{otherwise} \end{cases}, \tag{2.29}$$

and

$$\mathfrak{g}_2(R_i) = \begin{cases} \alpha_{\mathsf{L}} & \text{if } R_i \leq r_{\mathsf{B}} \\ \alpha_{\mathsf{N}} & \text{if } R_i > r_{\mathsf{B}} \end{cases}, \tag{2.30}$$

$a_i = \frac{P_i}{P_0} G_{\mathsf{r}}$ and $b_i = \frac{P_i}{P_0} g_{\mathsf{r}}$. Additionally, we have

$$m_i \;\; = \;\; \begin{cases} m_{\mathsf{L}} & \text{if } R_i \leq r_{\mathsf{B}} \\ m_{\mathsf{N}} & \text{if } R_i > r_{\mathsf{B}} \end{cases}. \tag{2.31}$$

For X_i drawn from a BPP, ϕ_i is uniform random variable in the interval $[0, 2\pi)$ and R_i has pdf

$$f_{R_i}(r) = \;\; \frac{2\pi r}{|\mathcal{A}|} \;\; r_{\mathsf{in}} \leq r \leq r_{\mathsf{out}}. \tag{2.32}$$

Next, note that for $|\phi_i - \phi_0| \leq \frac{\theta_{\mathsf{r}}^{(\mathsf{a})}}{2}$ and $r_{\mathsf{in}} \leq R_i \leq r_{\mathsf{B}}$, $\Omega_i = a_i R_i^{-\alpha_{\mathsf{L}}}$ has conditional pdf

$$f_{\Omega_i}(\omega) = \frac{2\pi \omega^{-\frac{2+\alpha_{\mathsf{L}}}{\alpha_{\mathsf{L}}}}}{\alpha_{\mathsf{L}} |\mathcal{A}| \left(\frac{\pi(r_{\mathsf{B}}^2 - r_{\mathsf{in}}^2)}{|\mathcal{A}|} \right)} a_i^{2/\alpha_{\mathsf{L}}}, \;\; \frac{a_i}{r_{\mathsf{B}}^{\alpha_{\mathsf{L}}}} \leq w \leq \frac{a_i}{r_{\mathsf{in}}^{\alpha_{\mathsf{L}}}}. \tag{2.33}$$

When $|\phi_i - \phi_0| > \frac{\theta_{\mathsf{r}}^{(\mathsf{a})}}{2}$, a_i in (2.33) is replaced with b_i, while the α_{L} in (2.33) is replaced with α_{N} when $r_{\mathsf{B}} < R_i \leq r_{\mathsf{out}}$. These four cases can be captured by defining a function

$$\mathcal{D}\left(\omega; [\omega_1, \omega_2]; c; \alpha\right) = \frac{2\pi \omega^{-\frac{2+\alpha}{\alpha}}}{\alpha |\mathcal{A}| c^{-2/\alpha}}, \;\; \omega_1 \leq \omega \leq \omega_2. \tag{2.34}$$

It follows therefore that the pdf of Ω_i has the form $f_{\Omega_i}(w) =$

$$\left(1 - \frac{\theta_{\mathsf{r}}^{(\mathsf{a})}}{2\pi}\right) \left[\begin{array}{c} \mathcal{D}\left(\omega; \left[\frac{b_i}{r_{\mathsf{B}}^{\alpha_{\mathsf{L}}}}, \frac{b_i}{r_{\mathsf{in}}^{\alpha_{\mathsf{L}}}}\right]; b_i; \alpha_{\mathsf{L}}\right) \\ + \\ \mathcal{D}\left(\omega; \left[\frac{b_i}{r_{\mathsf{out}}^{\alpha_{\mathsf{N}}}}, \frac{b_i}{r_{\mathsf{B}}^{\alpha_{\mathsf{N}}}}\right]; b_i; \alpha_{\mathsf{N}}\right) \end{array} \right] + \frac{\theta_{\mathsf{r}}^{(\mathsf{a})}}{2\pi} \left[\begin{array}{c} \mathcal{D}\left(\omega; \left[\frac{a_i}{r_{\mathsf{B}}^{\alpha_{\mathsf{L}}}}, \frac{a_i}{r_{\mathsf{in}}^{\alpha_{\mathsf{L}}}}\right]; a_i; \alpha_{\mathsf{L}}\right) \\ + \\ \mathcal{D}\left(\omega; \left[\frac{a_i}{r_{\mathsf{out}}^{\alpha_{\mathsf{N}}}}, \frac{a_i}{r_{\mathsf{B}}^{\alpha_{\mathsf{N}}}}\right]; a_i; \alpha_{\mathsf{N}}\right) \end{array} \right]. \tag{2.35}$$

Using the definition in (2.7) and the expression in (2.14), we can write the spatially averaged CCDF of the SINR by taking an expectation with respect to $\{\Omega_i\}$ as

$$P_{\mathsf{c}}(\beta) = \mathbb{E}_{\mathbf{\Omega}}[P_{\mathsf{c}}(\beta, \mathbf{\Omega})] = \sum_{\ell=0}^{m_0-1} \frac{(\beta_0\sigma^2)^\ell}{\ell! e^{\beta_0\sigma^2}} \sum_{t=0}^{\ell} \binom{\ell}{t} \frac{t!}{\sigma^{2t}} \sum_{\mathcal{S}_t} \left(\prod_{i=1}^{K} \mathbb{E}_{\Omega_i} \left[\mathcal{G}_{t_i}(\Omega_i) \right] \right). \quad (2.36)$$

To evaluate $\mathbb{E}_{\Omega_i} \left[\mathcal{G}_{t_i}(\Omega_i) \right]$, we note that the integral

$$\int_0^\infty \mathcal{D}\left(\omega; [\omega_1, \omega_2]; c; \alpha\right) \mathcal{G}_{t_i}(\Omega_i) \mathrm{d}\omega = \int_{\omega_1}^{\omega_2} \frac{2\pi\omega^{-\frac{2+\alpha}{\alpha}}}{\alpha|\mathcal{A}|c^{-2/\alpha}} \mathcal{G}_{t_i}(\Omega_i) \mathrm{d}\omega$$

simplifies to the form

$$(1-p_{\mathsf{t}}) \frac{c^{2/\alpha}}{|\mathcal{A}|} \left[\frac{1}{{\omega_1}^{2/\alpha}} - \frac{1}{{\omega_2}^{2/\alpha}} \right] \delta[t_i] + \left\{ p_{\mathsf{M}} \left[\frac{\mathcal{M}_{t_i}\left(G_{\mathsf{t}}\omega_1; \alpha\right)}{{\omega_1}^{2/\alpha}} - \frac{\mathcal{M}_{t_i}\left(G_{\mathsf{t}}\omega_2; \alpha\right)}{{\omega_2}^{2/\alpha}} \right] + \right.$$
$$\left. (1-p_{\mathsf{M}}) \left[\frac{\mathcal{M}_{t_i}\left(g_{\mathsf{t}}\omega_1; \alpha\right)}{{\omega_1}^{2/\alpha}} - \frac{\mathcal{M}_{t_i}\left(g_{\mathsf{t}}\omega_2; \alpha\right)}{{\omega_2}^{2/\alpha}} \right] \right\} p_{\mathsf{t}} \mathcal{K}_{t_i}(\alpha, c), \quad (2.37)$$

where

$$\mathcal{K}_{t_i}(\alpha, c) = \frac{2\pi m_i^{m_i} \Gamma(m_i+t_i) \beta_0^{-(m_i+t_i)} c^{2/\alpha}}{\Gamma(m_i)|\mathcal{A}|(t_i!)\alpha},$$

$$\mathcal{M}_{t_i}(x; \alpha) = \frac{{}_2F_1\left(m_i+t_i, m_i+\frac{2}{\alpha}; m_i+\frac{2}{\alpha}+1; -\frac{m_i}{x\beta_0}\right)}{x^{m_i}\left(m_i+\frac{2}{\alpha}\right)},$$

m_i is as given by (2.31) and ${}_2F_1\left(a, b; c; z\right)$ is the Gauss hypergeometric function. Using the formulation in (2.37) for every term in (2.35), $\mathbb{E}_{\Omega_i} \left[\mathcal{G}_{t_i}(\Omega_i) \right]$ can be evaluated so that a closed-form expression for the spatially averaged CCDF of the SINR can be computed from (2.36). Solving (2.22) through numerical integration, but with (2.36) in the integrand, we can get the spatially averaged ergodic spectral efficiency.

2.7 Results for Random Geometry

This section gives simulation and numerical results for coverage probability and spectral efficiency, which confirm the validity of assumptions made for spatial

averaging. Results generated using assumptions 1 to 3 are all done using a Monte Carlo simulation (which operates by randomly placing the interferers and blockages according to the spatial model, but then computing the conditional outage using (2.14)). Results generated under assumption 4 can be generated using either a simulation or the analytical expression, and the methodology used will be clarified when the result is presented. The antenna parameters are assumed to be the same as that used earlier, as summarized in Table 2.2. The network region $\mathcal{A}$ considered here is an annulus with inner radius $r_{\mathsf{in}} = 0.3$ m and outer radius $r_{\mathsf{out}} = 2.1$ m. The users are assumed to be randomly distributed in $\mathcal{A}$ according to a BPP. The simulation parameters used are summarized in Table 2.3. These are the values used if not otherwise stated. The quantities K, W and σ^2 are parameters we vary for comparison later on. Varying K is equivalent to changing the interferer density λ since $|\mathcal{A}|$ is assumed to be fixed. Similarly, varying W amounts to changing the parameters for blockages. Finally, increasing σ^2 captures the effect of more noise in the receiver or a lower transmit power.

To understand the significance of scaling of the size of the antenna arrays, we plot coverage probability against SINR for 3 cases that have the same product of $N_{\mathrm{t}} \times N_{\mathrm{r}}$. This is shown in Fig. 2.10 where we let $p_{\mathsf{t}} = 0.5$ under only Assumption 1. As observed for the fixed geometry case in Section 2.5, we see that using more transmit antennas is better than having more receive antennas. This is also seen in Table 2.5 which summarizes the ergodic spectral efficiency for various antenna array configurations. The reason for the asymmetrical behavior with respect to N_{t} and N_{r} is that while larger N_{t} results in reduced probability $p_{\mathsf{M}} \propto \frac{1}{N_{\mathrm{t}}}$ that interferers radiate

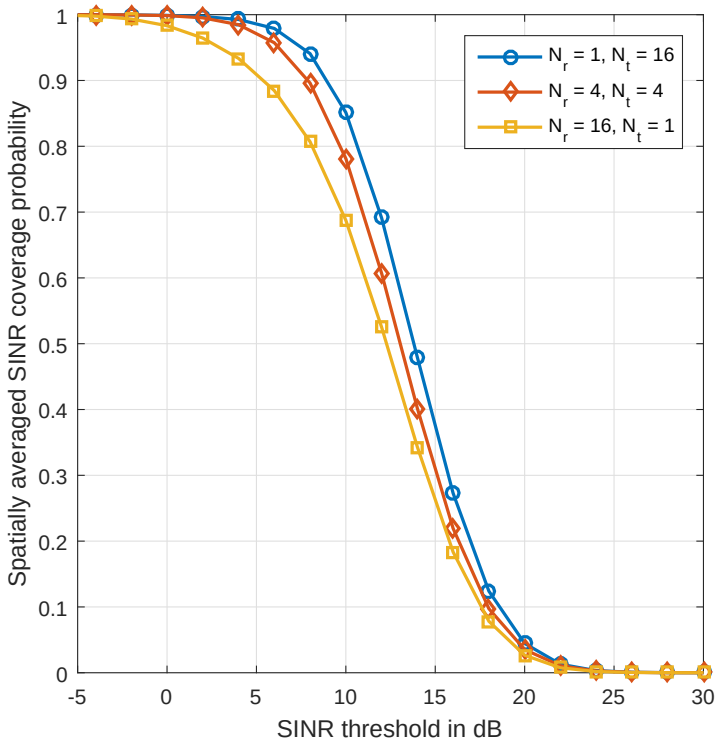

Figure 2.10: Spatially averaged SINR coverage probability obtained via simulation for three different antenna configurations - 4×4, 16×1, 1×16 and assumption 1 with $p_{\mathtt{t}} = 0.5$. Larger N_{t} is advantageous and the performance is not symmetric with respect to N_{t} and N_{r}.

with larger power $G_{\mathtt{t}}$, increasing N_{r} results in a decreased fraction of interferers falling within the receiver main-lobe which is proportional to $\theta_{\mathtt{r}}^{(\mathsf{a})} \propto \frac{1}{\sqrt{N_{\mathrm{r}}}}$.

We validate Assumptions 2 – 4 in Fig. 2.11. The plots for the CCDF of spectral efficiency with and without the assumptions are shown for $N_{\mathrm{t}} = N_{\mathrm{r}} = 4$ and $N_{\mathrm{t}} = N_{\mathrm{r}} = 16$ with $p_{\mathtt{t}} = 1$. We observe that, though the location of the blockages and the users are dependent in reality (as described by the *orbital model*), the assumptions

Table 2.5: Spatially averaged ergodic spectral efficiency for various antenna configurations

N_t \ N_r	1	4	16
1	0.6465	1.7459	3.2844
4	2.0526	3.5963	5.3523
16	3.8697	5.5886	7.4071

of treating the blockages and users as two independent BPPs (Assumption 2), associating a distance dependent blockage probability $p_{\mathtt{b}}(r)$ (Assumption 3) and defining the LOS ball (Assumption 4) are all reasonable. The plots of spectral efficiency for each of assumptions 1-4 when $p_{\mathtt{t}} = 1$ are shown in Fig. 2.12.

The plots in Fig. 2.13 show the CCDF of the SINR obtained using the analytic expressions derived in Section 2.6.3 and compares it with the actual simulation results under Assumptions 1 and 4. It is seen that the analytic expressions match exactly with the setting under Assumption 4 wherein we consider all the interferers within the LOS ball as unblocked and those outside as blocked from the reference receiver.

Next we look at the dependence of the system performance on W, the diameter of the blockages. We define the throughput as the product of $p_{\mathtt{t}}$ and the ergodic spectral efficiency. The plot of throughput versus W in Fig. 2.14 shows that as W is increased, the throughput improves. This is because, with larger W and for a fixed interferer density, the interfering signals get more blocked thus improving the SINR. The plots in Fig. 2.14 are for $N_{\mathrm{t}} = N_{\mathrm{r}} = 4$ and using the analytic expressions derived in Section 2.6.3.

In Fig. 2.15, the variation of SINR coverage probability is plotted as a function

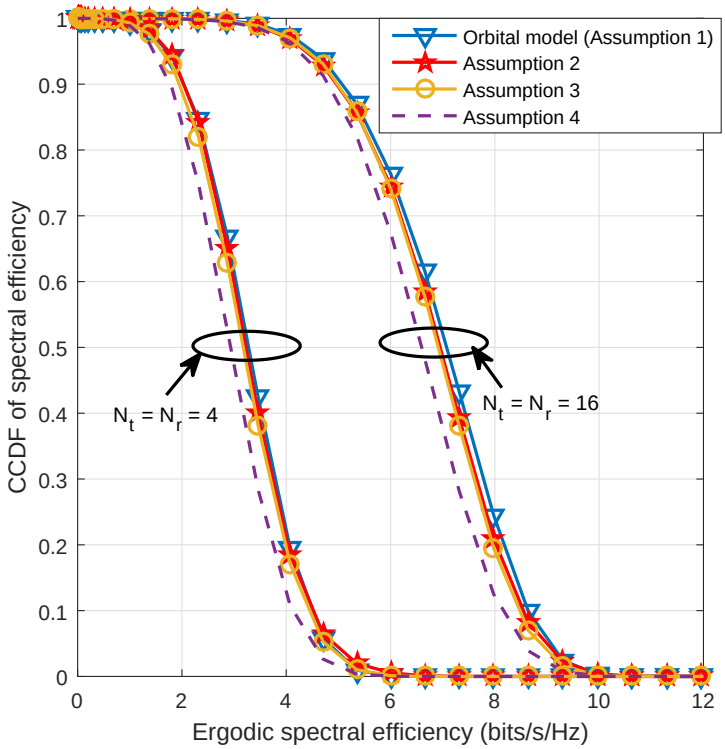

Figure 2.11: CCDF of spatially averaged ergodic spectral efficiency obtained via simulation for various transmitter and receiver antenna configurations $N_{\mathrm{t}} \times N_{\mathrm{r}}$ with $p_{\mathrm{t}} = 1$.

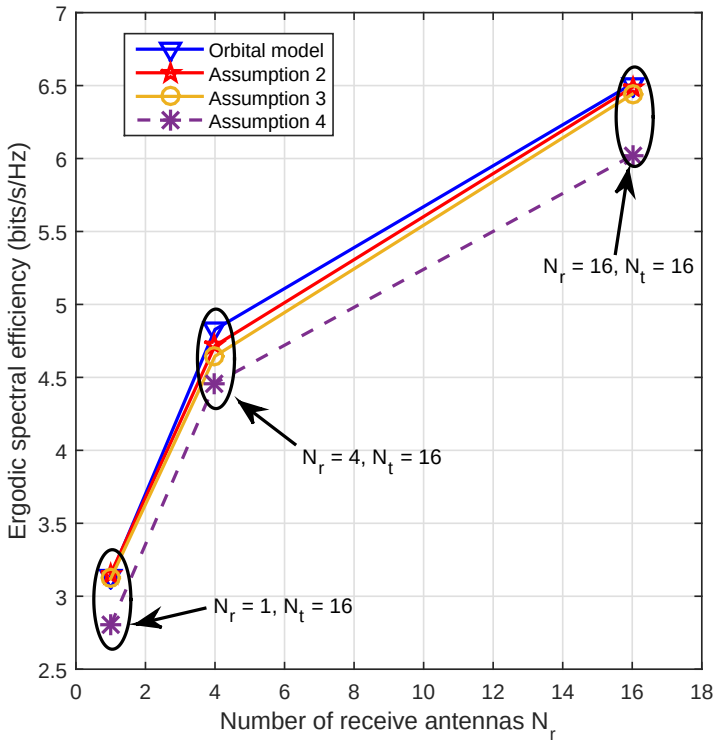

Figure 2.12: Spatially averaged ergodic spectral efficiency from simulation when $p_t = 1$ for various receiver antenna configurations and $N_t = 16$ with and without Assumptions 2 – 4 in Section 2.6.1.

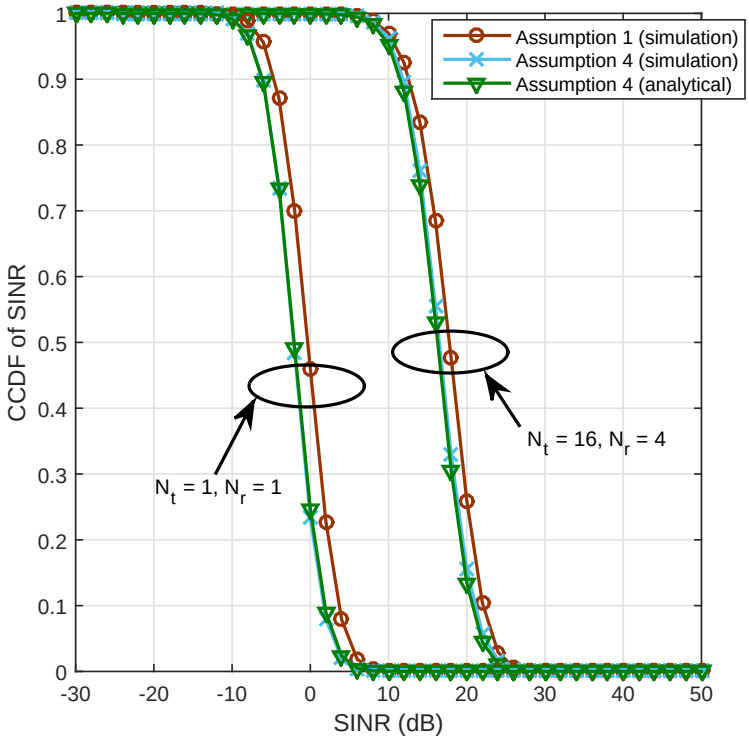

Figure 2.13: Plot showing the CCDF of spatially averaged SINR obtained from simulation and analytic closed-form expressions for different antenna configuration with $p_{\mathrm{t}} = 0.7$.

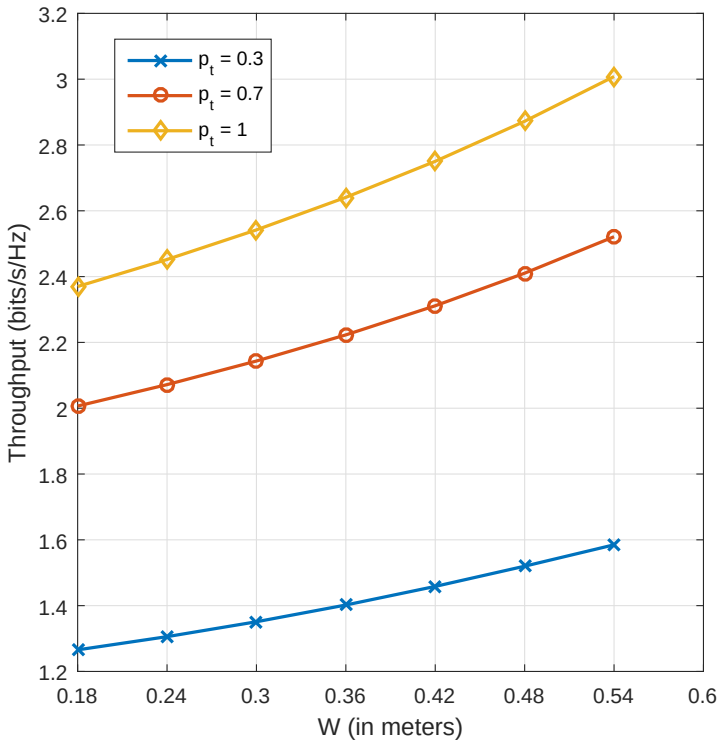

Figure 2.14: Spatially averaged throughput vs. W for different values of random-access probability p_{t} using the analytic expressions. Larger blockage diameter results in better throughput as the interferers are effectively blocked.

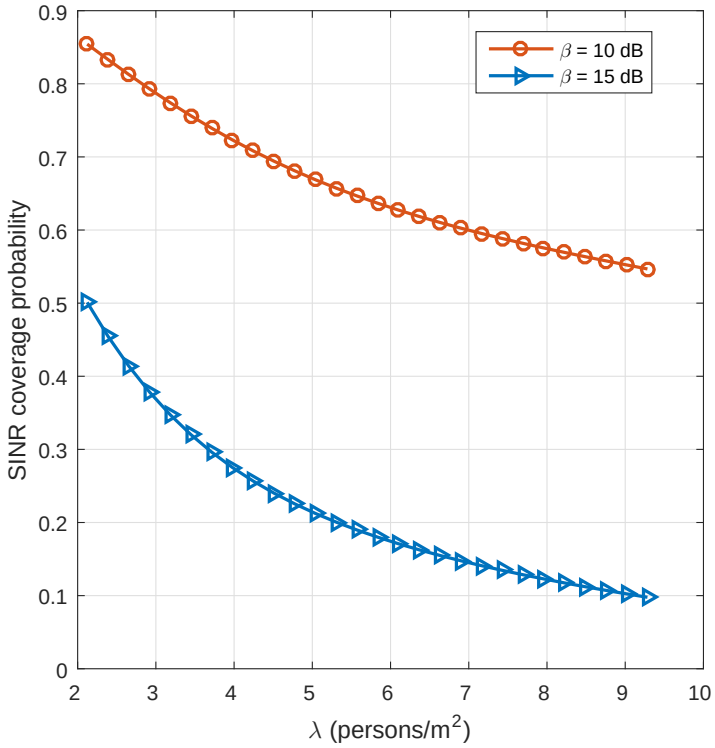

Figure 2.15: Spatially averaged SINR coverage probability vs. λ for different values of SINR threshold β using the analytic expressions. Here, we let $N_{\mathrm{t}} = 4$, $N_{\mathrm{r}} = 16$ and $p_{\mathrm{t}} = 1$.

of λ, the interferer density. We fix $N_{\mathrm{t}} = 4$, $N_{\mathrm{r}} = 16$ and $p_{\mathrm{t}} = 1$ for comparison and use the previously derived analytic expressions for the plots. It is seen that as λ is increased the SINR coverage decreases rapidly initially. However, with very high density, blocking probability also increases, hence showing lower rate of decrease with increasing λ in the plots later on. This also corroborates our assumption that (the users wearing) the interferers are also the source of blockages in the indoor wearables environment.

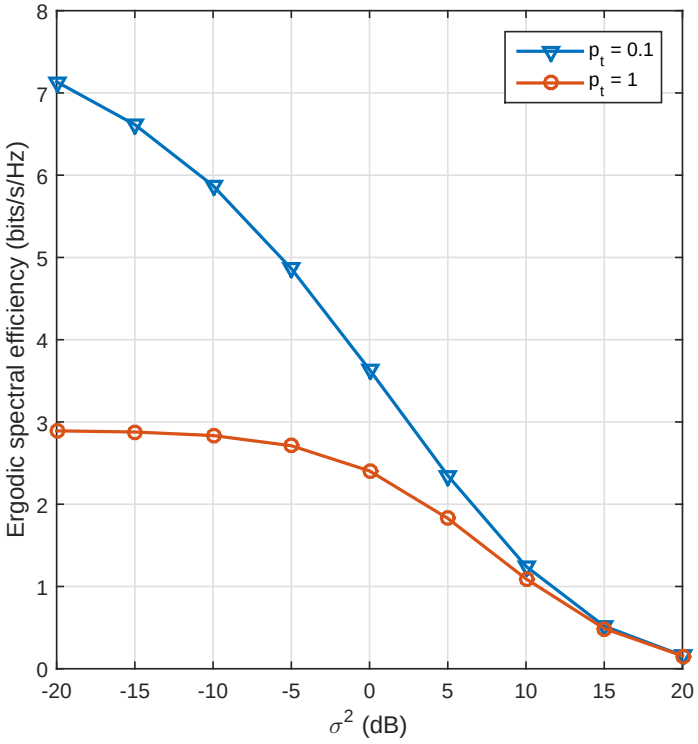

Figure 2.16: Spatially averaged ergodic spectral efficiency vs σ^2 for two different values of p_{t} using the analytic expressions when $N_{\mathrm{t}} = N_{\mathrm{r}} = 4$.

Fig. 2.16 shows the variation of ergodic spectral efficiency as we vary σ^2. Here we let $N_{\mathrm{t}} = N_{\mathrm{r}} = 4$ and use the analytic results in Section 2.6.3. It is seen that for smaller values of σ^2, the system is indeed interference limited as changing p_{t} results in significant change in the system performance. However as σ^2 is increased, the system becomes noise limited and different values for random-access probabilities of the interferers result in little change in the SINR distribution and hence the ergodic spectral efficiency.

2.8 Conclusion

In this chapter, we analyzed the performance of a mmWave wearable communication network operating in a finite region like that inside a train car. To model the sensitivity of mmWave signal propagation to the presence of human bodies in the network, we incorporated different path-loss and small-scale fading parameters depending on whether a link is blocked or not. It was seen that both interference and the probability of blockage of the interference signals are large when the crowd density is high, so that the SINR coverage probability decreases at a much lower rate with higher crowd density. We considered fixed as well as random positions for the interfering transmitters and assessed the impact of antenna parameters such as array gain and beamwidth on coverage and ergodic spectral efficiency of the system. It was seen that antenna main-lobe directivity and array gain play a crucial role in achieving giga-bits per second performance for wearable networks in a crowd. We proposed several assumptions and a model to analyze the system performance when the interferers are located at random locations. These gave closed-form expressions for spatially averaged coverage probability for mmWave wearable communication network when the user is located at the center of a dense crowd and the number of users is finite. The validity of the closed-form analytic results and the assumptions were confirmed against simulations. The analytic modeling presented in this chapter serves as a first step towards characterizing SINR performance of mmWave based ad-hoc networks in a finite but crowded environment, and enables one to avoid simulations to predict performance. The rate performance plots showed that coordination across users is not necessarily required for mmWave network operation in crowded scenarios,

thanks to the inherent isolation properties of mmWave signals.

The work in this chapter can easily be extended to the case that the reference link can be blocked by the user's own body. The procedure would involve finding two conditional outage probabilities, one conditioned on the link not being blocked by the user (using the procedure outlined in this chapter) and the other conditioned on the link being blocked by the user (adapting the procedures so that the reference link's path loss is α_{N} and Nakagami factor is m_{N}). The two probabilities can then be weighted by the probability of self-blockage, which can be determined based on the assumed spatial models. Using a more refined model to capture this self-blockage and incorporating it in the analysis is an interesting topic for future work.

Chapter 3

Practical Aspects of Indoor MmWave Coverage: Self-blockage and Surface Reflections

3.1 Overview

Supporting high data rate wireless connectivity among mmWave wearable devices in a dense indoor environment is challenging in indoor environments. This is primarily due to bandwidth scarcity when many users operate multiple devices simultaneously, and the added impact of reflections from walls. In this chapter[1], to provide a means for concrete analysis, we present a system model that admits easy analysis of dense, indoor mmWave wearable networks. We evaluate the performance of the system while considering the unique propagation features at mmWave frequencies, such as human body blockages and reflections from walls. One conclusion is that the non-isotropy of the surroundings relative to a reference user causes variations in system performance depending on the user location, body orientation, and the density of the network. The impact of using antenna arrays is quantified through analytic closed-form expressions that incorporate antenna gain and directivity. It is shown that using

[1]This chapter is based on the work published in the journal paper: K. Venugopal, and R. W. Heath, Jr., "Millimeter wave networked wearables in dense indoor environments," IEEE Access, vol. 4, pp. 1205-1221, 2016. This work was supervised by Prof. Robert Heath. Alexander Pyattaev and Dr. Kerstin Johnsson gave valuable suggestions and inputs from ray-tracing data to model human user self-blockage and reflections in indoor mmWave wearable networks.

directional antennas, positioning the transceiver devices appropriately, and orienting the human user body in certain directions depending on the user location result in gigabits-per-second achievable ergodic rates for mmWave wearable networks.

3.2 Indoor Wearable Networks

A typical example of a dense indoor environment is shown in Fig. 3.1, where the user density could be as high as three users per square meter [48]. In conventional wireless BANs, this is not a major issue as the data-rate requirements are much lower. For high-end devices in a wearable network, coordination across users could reduce interference. But this would increase the overhead data and may add to the complexity and cost of the devices [26]. An abrupt change in the high crowd density may also be detrimental to the existing connections. A desirable feature of a wearable network, thus, is to support intra-network communication between devices in a way that is independent of other users' wearable networks. Since the mmWave signals are blocked by human body and objects, the mmWave band is an ideal candidate to deliver high data rates in wireless personal area networks [9]. This is promising for dense deployments of wearable networks involving simultaneous operation of many devices [26, 49].

There is limited prior analytic work related to mmWave wearable networking in indoor environment. A comparison between body area networks at 2.5 GHz and 60 GHz in terms of inter-network interference in indoor environment using CAD model and simulation was reported in [49]. Their study concluded that significant amount of interference mitigation can be achieved by using the mmWave band, allowing a

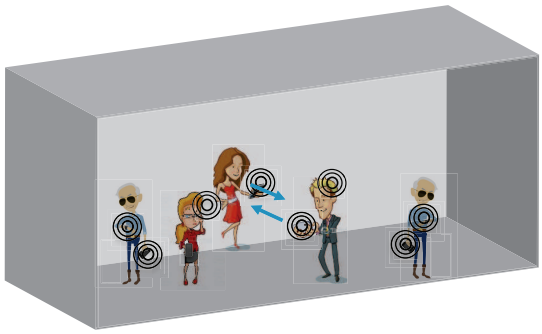

Figure 3.1: Figure illustrating a typical crowded indoor scenario such as a train car with several users operating their respective wearable networks.

greater number of collocated wearable networks. Prior work in [26] used ray tracing tool to show that the use of mmWave is critical to support massive deployment of wearable networks with high-end devices in indoor commuter train scenario. It was also noted that the existing mmWave technologies have to be enhanced to efficiently handle the scenarios where several neighboring users' networks overlap. In [17], the effect of first order reflections for mmWave signal propagation in indoor operations of wearable networks was characterized and system performances when a user is located at the center and a corner of an indoor enclosure were evaluated using simulations.

In this chapter, we present a system model to study the feasibility of mmWave wearable networks in the absence of coordination across the users. Unlike the contributions in Chapter 2, in this chapter, we also explicitly model signal reflections due to the enclosed space (network boundaries) and the impact of self-body blockage on mmWave signals. The model can be used to evaluate the worst case performance of a mmWave-based indoor single-hop communication system when crowd density is high and in the absence of an advanced medium access (MAC) protocol. Our model can

be used to identify *predominant interferers* using an approach similar to [19]. This classification can be used in future work for MAC and physical layer system design to reduce interference via coordination and further improve performance. Unlike [19], the proposed model is more general as our approach does not restrict the typical user to the center of the crowd. We incorporate the effect of user density and orientation of the user body relative to the wearable devices in the model to understand the best conditions for achieving maximum system performance. Using directional antennas in the wearable devices, and assuming the users are randomly located in the indoor environment, we analyze performance of a typical user's on-body mmWave communication link. Using the analytic results, we show how system performance is non-isotropic in an indoor environment and varies as a function of both location as well as body orientation of the reference user.

The rest of the chapter is organized as follows: In Section 3.3, we first review key prior work related to modeling wireless networks and then proceed to explain the proposed system model. This is followed by the derivation of spatially averaged signal-to-noise-plus-interference-ratio (SINR) distribution in Section 3.4 which leads to closed-form expressions for system performance. In Section 3.5, we provide simulation results to validate the analysis done in Section 3.4. We summarize the main results of the chapter in Section 3.6.

3.3 Modeling mmWave Wearable Networks with Stochastic Geometry

Developing tractable models to characterize performance of mmWave-based wearable networks is key to understanding the impact of crowd density and the necessity of coordination across users via advanced protocols if the performance without inter-user coordination is poor. In this section, we elaborate on the analytic approach used in the chapter to model wearable networks. The network geometry, blockage model and the propagation features assumed are explained and the intuitive reasoning for the assumptions made are provided at relevant places. The performance analysis and modeling leverage tools from stochastic geometry which is reviewed next.

3.3.1 Background on Stochastic Geometry

Stochastic geometry provides a mathematical approach for modeling wireless networks, which has been used to study outdoor systems. The transceiver nodes in the network are modeled as randomly located in the 2-D plane to form a point process of known intensity, and the distribution of the interference field as seen by a typical user is analyzed. Stochastic geometry allows derivation of analytic expressions for average performance metrics like the SINR, spectral efficiency, and the sum throughput for infinite networks [30, 32, 33].

In the context of mmWave-based cellular systems, [14, 38] used results from stochastic geometry to characterize network coverage and capacity. The important propagation features of the mmWave signal, especially signal blockage due to buildings and human user body were modeled in [12,38]. In [12], a distance-dependent blockage

model was first derived using results from random shape theory, and was then used to derive analytic expressions for SINR coverage. An important assumption for these derivations was that the sources of signal blockages (buildings) and the communication devices are drawn from independent Poisson Point Processes (PPP).

For dense indoor operations using mmWave, human bodies of the users are the main source of blockages and can result in 30-60 dB of attenuation for mmWave signals [37, 50, 51]. The users that carry potentially interfering devices, hence, also potentially block the interference from other users. This is a key difference compared to outdoor cellular based mmWave systems where independent spatial distribution assumption for blockages and interferers is easier to justify. Another point of difference between outdoor cellular systems and indoor mmWave systems is the spatial extent and number of transceiver devices considered in the analysis. While an infinite region of operation and infinite number of users could be justified in a cellular setting, system models for indoor operation have to consider finite geometry and number of users.

The exact effects of first order reflections from all the six faces of a cuboidal enclosure were considered for the simulation results in [17]. This provided valuable insight into the nature of surface reflections in the indoor mmWave setup. While it was assumed that the reflections from the ceilings were never blocked and the self-body human blockage was characterized, [17] does not consider directional antennas at the devices and also does not report closed-form analytic expressions for spatially averaged system performance. The system model that we explain next leads to closed-form expressions for spatially averaged performance of a typical user's wearable network communication link.

3.3.2 Network Model

To model a train car, we consider an enclosed space $\mathcal{T}$ of dimensions $L \times B \times H$ as shown in Fig. 3.2a which has highly reflective walls and ceiling, and a non-reflective floor. Such a model is similar to that used in [17], with the exception that we assume the floor to be non-reflecting as the material used for flooring is generally rougher, and different from the smooth surfaces of the walls and ceiling [46]. Note that seating arrangements and other finer details of the interior of a typical train car are neglected in this model. The users are assumed distributed randomly within $\mathcal{T}$ and are modeled as cylinders $\mathcal{U}$ of a fixed diameter W, ideally characterizing the width of the human body torso including the legs. Each user is assumed to be equipped with one high-end wearable receiver and one controlling hub (smartphone) which acts as the device-to-device communication transmitter.

All the mmWave wearable transmitter devices are assumed to be positioned at a depth d_{h} from the ceiling of $\mathcal{T}$ along the plane denoted as $\mathcal{P}$ (Fig. 3.2a) and positioned randomly on a circle of radius $d \geq W/2$ concentric with their associated user. Typical values for d can vary from 2-30 centimeters depending on whether the device is placed on the body surface or held on stretched hand. The interfering transmitters and their locations are denoted as $\mathsf{T}_i = x_i + \mathrm{j}y_i$. In this representation, the point $\mathcal{O}$ as shown in Fig. 3.2, is assumed to be the origin. We denote the reference receiver and its location by R_0 which is also assumed to be at a distance d from the reference user's body. Further, the separation between R_0 and the reference transmitter T_0 is assumed to be r_0 in the azimuth and z_0 in the elevation plane. The geometry of the reference transmitter-receiver is illustrated in Fig. 3.3. The

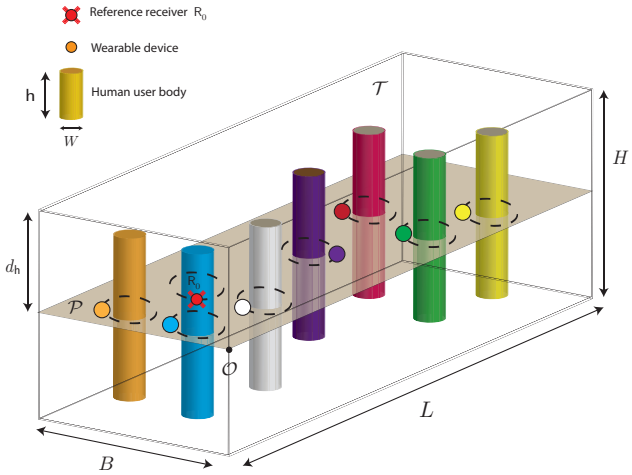

(a) 3-D model showing the enclosed region $\mathcal{T}$ and the wearable transmitters positioned in the plane $\mathcal{P}$.

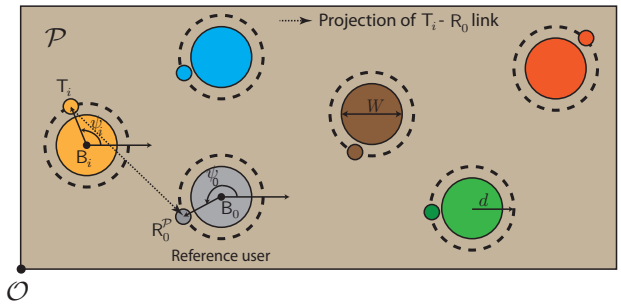

(b) 2-D model in $\mathcal{P}$ illustrating the user-body orientation representation used in this chapter.

Figure 3.2: Network model showing the human users, reference receiver R_0, reference and interfering transmitters. All the wearable devices are at a distance d around the diameter-W user body.

projection of the reference receiver onto $\mathcal{P}$, the plane containing the transmitters is denoted by the complex number $\mathsf{R}_0^{\mathcal{P}} = x_0 + \mathrm{j}y_0$, so that $|\mathsf{R}_0^{\mathcal{P}} - \mathsf{T}_0| = r_0$. We use the following notations (see Fig. 3.3) for the azimuth and elevation angles of the reference transmitter relative to the reference receiver.

$$\phi_0^{\mathsf{a}} = \measuredangle(\mathsf{T}_0 - \mathsf{R}_0^{\mathcal{P}}) \text{ and} \tag{3.1}$$

$$\phi_0^{\mathsf{e}} = -\arctan\left(\frac{z_0}{r_0}\right). \tag{3.2}$$

User bodies $\mathcal{U}$ intersect with $\mathcal{P}$ to form diameter-W disks. We use the notation B_i to denote both this disk as well as its center for the i^{th} user. We assume $\{\mathsf{B}_i\}$ are drawn from a non-homogeneous PPP that has intensity λ in the region of interest, and zero outside it. This assumption eases analysis for mmWave wearable networks in crowded environment [19] and also captures the uniform but random crowd distribution inside a public transportation system during rush hours. Since the transceivers are located relative to the users carrying them, we say user i is facing towards a direction $\psi_i = \measuredangle(\mathsf{T}_i - \mathsf{B}_i)$. The reference receiver R_0 is assumed to be facing towards the direction $\psi_0 = \measuredangle\left(\mathsf{R}_0^{\mathcal{P}} - \mathsf{B}_0\right)$. This is illustrated in Fig. 3.2b.

3.3.3 Signal Model

The Nakagami distribution has been used to model small scale fading for indoor mmWave propagation in prior work [52, 53] . The received power gain due to fading is then a Gamma distributed random variable. We assume the power gains $\{h_i\}$ due to fading for the wireless links from $\{\mathsf{T}_i\}$ to the reference receiver are independent and identically distributed normalized Gamma random variable with parameter m.

The reference signal link of (fixed) length $d_0 = \sqrt{r_0^2 + z_0^2}$ is assumed to be unblocked by the reference user's body. Given the reference user's on-body signal link length is small (typically less than one meter) this assumption is reasonable. We would like to point out here that, in practice, the signal link can still be occluded by the reference user's physical activity like hand movements, gait, posture etc. In the absence of a more elaborate but tractable stochastic model to incorporate these aspects based on measurement data, we assume the on-body reference signal link is unblocked. With the assumed human body model in Fig. 3.3 and given d, ψ_0, r_0 and W, in order for the reference signal to be unblocked, the following condition must hold:

$$r_0 \;\leq\; 2\sqrt{d^2 - \left(\frac{W}{2}\right)^2}. \tag{3.3}$$

Additionally, letting $r_0 = \sqrt{d^2 - \left(\frac{W}{2}\right)^2}$, we have

$$\phi_0^{\mathsf{a}} \;=\; \psi_0 - \frac{\pi}{2} - \arcsin\left(\frac{r_0}{2d}\right). \tag{3.4}$$

The condition in (3.3) and the derivation of (3.4) can be understood using the illustration of reference signal link's geometry in Fig. 3.3

The path-loss exponent of the signal link is denoted α_{L}, where the subscript L denotes line-of-sight (LOS). This is in line with our assumption that the on-body reference signal link is unblocked. The non-LOS (NLOS) path-loss exponent is denoted as α_{N}, the relevance of which is explained momentarily. Such a differentiation in the path-loss exponents has been supported by indoor measurement campaigns [54]. The power gain h_0 due to fading in the reference link is also assumed to be a normalized Gamma distributed random variable with parameter m. The path-loss function

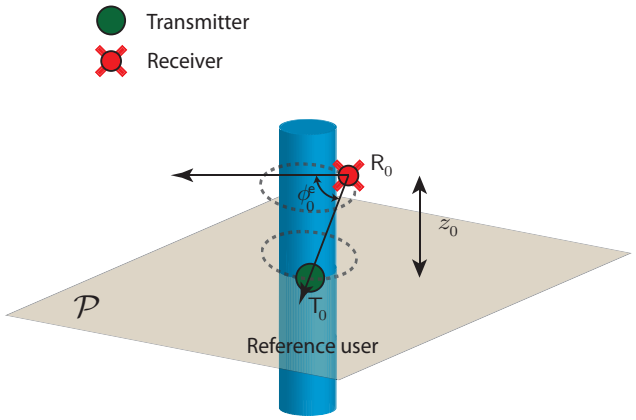

(a) Reference signal link in 3D. The reference receiver is at a height z_0 above the reference transmitter and forms an elevation angle ϕ_0^{e} with the plane containing the transmitters $\mathcal{P}$.

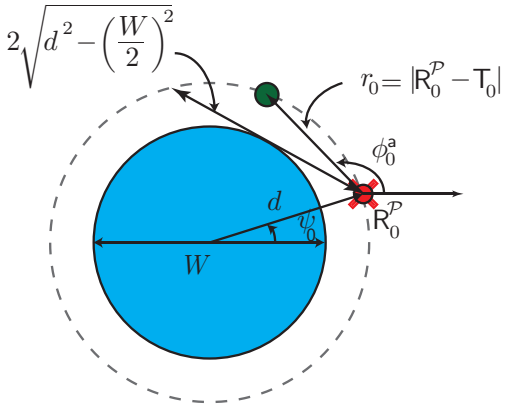

(b) Projection of the reference receiver onto $\mathcal{P}$ showing the azimuth angle ϕ_0^{a} between the reference user's devices and the horizontal separation r_0. The reference link is unblocked whenever (3.3) holds.

Figure 3.3: Illustration showing the reference signal link's geometry.

for the link from T_i to the reference receiver depends on the relative position of T_i with respect to R_0 and is denoted as $\ell(\mathsf{R}_0, \mathsf{T}_i)$. All transmitters are assumed to be transmitting at a constant transmit power. For example, this could be the maximum transmit power of devices as set out by regulations, in which case this would be a worst case scenario. The noise power normalized by the signal power observed at a reference distance is denoted as σ^2.

The receiver-transmitter pair associated with user i are assumed to be aligned. From the reference receiver's perspective, this assumption leads to a random transmit gain for the interference from T_i as seen at R_0. Defining p_{M}, as in before (2.4), the transmit antenna gain from the i^{th} interferer can be represented using a discrete random variable $G_{\mathsf{t},i}$ as follows

$$G_{\mathsf{t},i} \;=\; \begin{cases} G_{\mathsf{t}} & \text{w.p.} \quad p_{\mathsf{M}} \\ g_{\mathsf{t}} & \text{w.p.} \quad 1-p_{\mathsf{M}} \end{cases}. \tag{3.5}$$

The reference receiver's antenna main-lobe is pointed towards (fixed) azimuth angle $\phi_0^{(\mathsf{a})}$ and elevation angle $\phi_0^{(\mathsf{e})}$, the location where the reference transmitter is positioned. Since the beam-width of the receiver antenna is $\theta_{\mathsf{r}}^{(\mathsf{a})}$ and $\theta_{\mathsf{r}}^{(\mathsf{e})}$ in the azimuth and elevation, respectively, the signals from all the interferers that are within an elevation angle $\phi_0^{(\mathsf{e})} \pm \frac{\theta_{\mathsf{r}}^{(\mathsf{e})}}{2}$ and azimuth angle $\phi_0^{(\mathsf{a})} \pm \frac{\theta_{\mathsf{r}}^{(\mathsf{a})}}{2}$ relative to the reference receiver R_0 are amplified by G_{r}, the main-lobe gain of R_0. Specifically, interference from the i^{th} user's transmitter T_i is amplified by a factor $G_{\mathsf{r},i}$ at the reference receiver, where

$$G_{\mathsf{r},i} = \begin{cases} G_{\mathsf{r}} & \text{if } \; |\measuredangle\left(\mathsf{T}_i - \mathsf{R}_0^{\mathcal{P}}\right) - \phi_0^{(\mathsf{a})}| \leq \frac{\theta_{\mathsf{r}}^{(\mathsf{a})}}{2} \text{ and } \; |\arctan\left(\frac{z_0}{|\mathsf{T}_i - \mathsf{R}_0^{\mathcal{P}}|}\right) - \phi_0^{(\mathsf{e})}| \leq \frac{\theta_{\mathsf{r}}^{(\mathsf{e})}}{2} \\ g_{\mathsf{r}} & \text{else} \end{cases}. \tag{3.6}$$

3.3.4 Modeling Interference and Blockages

The signal from an interferer T_i to R_0 can be potentially blocked by user i, the reference user, and/or user $j,\ j \neq i$. The blockage by user i and the reference (termed self-blockage in [38]) can occur irrespective of the locations of T_i and R_0. Specifically, self-blockage depends on whether user i and the reference user are facing each other or not. The blockage by user $j \neq i$, depends on the relative separation between T_i and $\mathsf{R}_0^{\mathcal{P}}$, and their individual positions with respect to the reflecting walls of the enclosure. For this reason, self-blockage and blockage by user $j \neq i$ are treated separately.

3.3.4.1 Blockage of T_i's signal by user $j \neq i$

To see if user $j,\ j \neq i$ blocks T_i, we use the approach in [1] and define a region $\mathcal{C}(\mathsf{B}_j) \in \mathcal{P}$ for each user relative to $\mathsf{R}_0^{\mathcal{P}}$ in $\mathcal{P}$. This region falls behind user j's body B_j as seen from the reference receiver. Mathematically,

$$\mathcal{C}(\mathsf{B}_j) = \Bigg\{ z \in \mathcal{P} : |z - \mathsf{R}_0^{\mathcal{P}}|^2 \geq |\mathsf{B}_j - \mathsf{R}_0^{\mathcal{P}}|^2 - \left(\frac{W}{2}\right)^2, \\ |\measuredangle(z - \mathsf{R}_0^{\mathcal{P}}) - \measuredangle(\mathsf{B}_j - \mathsf{R}_0^{\mathcal{P}})| \leq \arcsin\left(\frac{W}{2|\mathsf{B}_j - \mathsf{R}_0^{\mathcal{P}}|}\right) \Bigg\}, \tag{3.7}$$

and we refer this region as the *blocking cone* of B_j. The concept of blocking cone is illustrated in Fig. 3.4. Note that, using (3.7), we can also define the blocking cone of the reference user which is denoted as $\mathcal{C}(\mathsf{B}_0)$. We denote T_i as *strong* if its direct and wall reflected paths do not fall in the blocking cone $\mathcal{C}(\mathsf{B}_j),\ j \neq i$. Otherwise, T_i is denoted as a *weak* interferer. Since B_j is uniformly distributed in $\mathcal{P}$, the interfering transmitters located farther away from $\mathsf{R}_0^{\mathcal{P}}$ have a higher chance

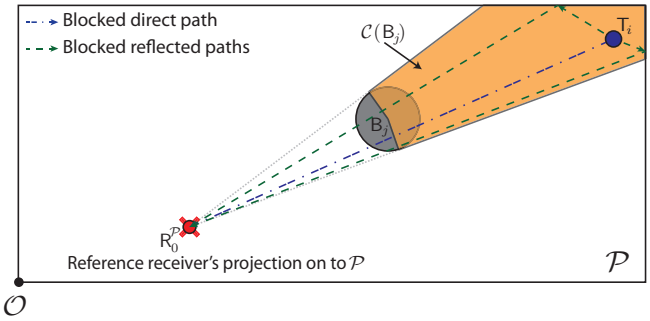

Figure 3.4: Illustration of a blocking cone showing the direct and wall-reflected paths of T_i getting blocked by B_j.

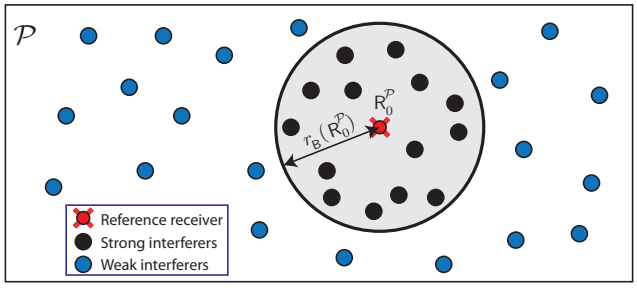

Figure 3.5: Illustration showing the threshold distance $r_{\mathsf{B}}(\mathsf{R}_0^{\mathcal{P}})$ based classification of interferers into strong and weak interferers. Interferes whose horizontal separation from the reference receiver is smaller than $r_{\mathsf{B}}(\mathsf{R}_0^{\mathcal{P}})$ are strong.

of being a weak interferer. For analytic tractability, we define a threshold distance $r_{\mathsf{B}}(\mathsf{R}_0^{\mathcal{P}})$ around $\mathsf{R}_0^{\mathcal{P}}$ in $\mathcal{P}$ such that if $|\mathsf{R}_0^{\mathcal{P}} - \mathsf{T}_i| \leq r_{\mathsf{B}}(\mathsf{R}_0^{\mathcal{P}})$, T_i is a strong interferer. Having $|\mathsf{R}_0^{\mathcal{P}} - \mathsf{T}_i| > r_{\mathsf{B}}(\mathsf{R}_0^{\mathcal{P}})$ implies that there always exists some user $j \neq i$ that blocks the direct and wall-reflected propagation paths from T_i to R_0. An illustration describing this modeling assumption is shown in Fig. 3.5. This threshold-distance-based model captures the blockage effects due to a third user j for the interference signal from user i as experienced at the reference receiver.

By definition, T_i is a strong interferer whenever $|\mathsf{R}_0^{\mathcal{P}} - \mathsf{T}_i| \leq r_{\mathsf{B}}(\mathsf{R}_0^{\mathcal{P}})$, and

there exists no $\mathsf{B}_j, j \neq i$ in the path from T_i to $\mathsf{R}_0^{\mathcal{P}}$. To evaluate $r_{\mathsf{B}}(\mathsf{R}_0^{\mathcal{P}})$, we use the illustration in Fig. 3.6a, which shows T_i getting blocked by a user $j \neq i$ whenever user j (center of B_j) is located anywhere in the region $\mathcal{A}(\mathsf{R}_0^{\mathcal{P}}, \mathsf{T}_i)$ [18]. Since the users are assumed to be drawn from $\mathbf{\Phi}$, the probability that there is no user in the region $\mathcal{A}(\mathsf{R}_0^{\mathcal{P}}, \mathsf{T}_i)$ is $\exp(-\lambda|\mathcal{A}(\mathsf{R}_0^{\mathcal{P}}, \mathsf{T}_i)|)$, where $|\mathcal{A}(\mathsf{R}_0^{\mathcal{P}}, \mathsf{T}_i)|$ is the area of $\mathcal{A}(\mathsf{R}_0^{\mathcal{P}}, \mathsf{T}_i)$. The shape of $\mathcal{A}(\mathsf{R}_0^{\mathcal{P}}, \mathsf{T}_i)$ varies with $\mathsf{R}_0^{\mathcal{P}}$ (and T_i). In particular, the variation in the shape and hence the area $|\mathcal{A}(\mathsf{R}_0^{\mathcal{P}}, \mathsf{T}_i)|$ is more pronounced when one or both of $\mathsf{R}_0^{\mathcal{P}}$ and T_i are near the walls as shown in Fig. 3.6b. Hence, the quantity $|\mathcal{A}(\mathsf{R}_0^{\mathcal{P}}, \mathsf{T}_i)|$ required to evaluate the probability that the interferer T_i is blocked from the reference receiver is not fully defined by the distance between $\mathsf{R}_0^{\mathcal{P}}$ and T_i. This implies the distance-dependent blockage model used in prior work to characterize mmWave outdoor network may not directly apply to indoor communication using mmWave. For indoor mmWave communication, however, the effect of wall-reflections - which results in a near LOS signal propagation - is higher when the receiver and/or the interfering transmitter are closer to the wall (Fig. 3.7a). In a densely crowded environment, since the reflected interference signals need to propagate through a longer path, the probability that the onward and reflected paths for the interference bouncing off a wall are not blocked is higher. This results in a larger area $\mathcal{A}'(\mathsf{R}_0^{\mathcal{P}}, \mathsf{T}_i)$ as illustrated in Fig. 3.7b.

Assumption 1: The actual area of $\mathcal{A}'(\mathsf{R}_0^{\mathcal{P}}, \mathsf{T}_i)$ can be approximated by the area seen by receiver-transmitter pair positioned away from the reflecting walls so that

$$|\mathcal{A}'(\mathsf{R}_0^{\mathcal{P}}, \mathsf{T}_i)| \approx |\mathsf{R}_0^{\mathcal{P}} - \mathsf{T}_i|W + \frac{\pi W^2}{4}. \tag{3.8}$$

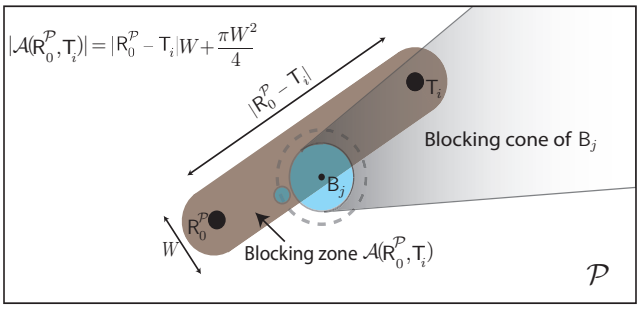

(a) Case when T_i and $\mathsf{R}_0^{\mathcal{P}}$ are away from the reflecting walls. The wall-reflected paths have lengths far larger than the direct path length and hence are not considered.

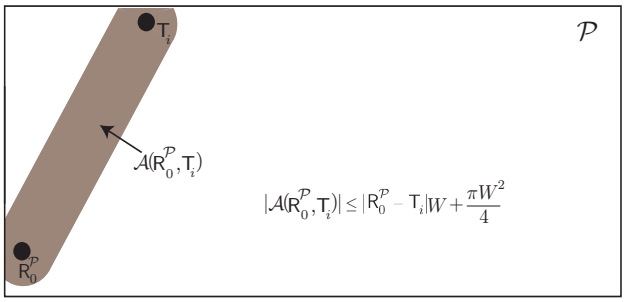

(b) Case when T_i and $\mathsf{R}_0^{\mathcal{P}}$ are near the reflecting walls. The area of the region $\mathcal{A}(\mathsf{R}_0^{\mathcal{P}}, \mathsf{T}_i)$ is not fully defined by the horizontal separation between $\mathsf{R}_0^{\mathcal{P}}$ and T_i now.

Figure 3.6: Figures showing the blocking zone $\mathcal{A}(\mathsf{R}_0^{\mathcal{P}}, \mathsf{T}_i)$ when the devices are away from the reflecting walls, and otherwise. A potential blockage B_j within $\mathcal{A}(\mathsf{R}_0^{\mathcal{P}}, \mathsf{T}_i)$ and its blocking cone (cf [1] for definition of blocking cone) are also shown for illustration.

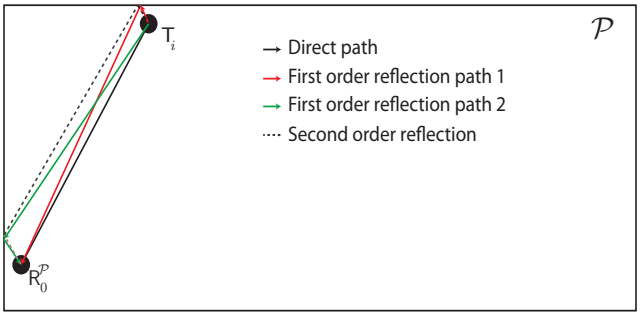

(a) The predominant 1^{st} and 2^{nd} order reflections when T_i and $\mathsf{R}_0^{\mathcal{P}}$ are near the walls. Only those reflected paths whose path lengths are close to the direct path length are shown.

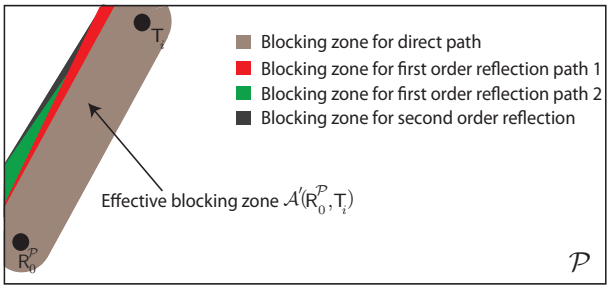

(b) The actual blocking zone $\mathcal{A}'(\mathsf{R}_0^{\mathcal{P}}, \mathsf{T}_i)$ when T_i and $\mathsf{R}_0^{\mathcal{P}}$ are near the reflecting walls.

Figure 3.7: Figures showing the effective blocking zone $\mathcal{A}'(\mathsf{R}_0^{\mathcal{P}}, \mathsf{T}_i)$ when T_i and $\mathsf{R}_0^{\mathcal{P}}$ are near from the walls.

With this assumption, the blockage probability $p_{\mathsf{b}}\left(\mathsf{R}_0^{\mathcal{P}}, \mathsf{T}_i\right)$ of a user i due to user $j \neq i$ is a function of only the separation between $\mathsf{R}_0^{\mathcal{P}}$ and T_i. This is evaluated as

$$p_{\mathsf{b}}\left(\mathsf{R}_0^{\mathcal{P}}, \mathsf{T}_i\right) = 1 - \exp\left(-\lambda\left(|\mathsf{R}_0^{\mathcal{P}} - \mathsf{T}_i|W + \frac{\pi W^2}{4}\right)\right). \tag{3.9}$$

We next evaluate the threshold distance $r_{\mathsf{B}}(\mathsf{R}_0^{\mathcal{P}})$. This is computed in such a way that the average number of interferers whose direct and reflected paths are not blocked are preserved. The average number of strong interferers $\rho(\mathsf{R}_0)$ as seen from R_0 is

$$\begin{aligned}\rho(\mathsf{R}_0) &= \lambda \int_{z\in\mathcal{P}} \left(1 - p_{\mathsf{b}}(\mathsf{R}_0^{\mathcal{P}}, z)\right) \mathrm{d}z \qquad (3.10)\\ &= \lambda \int_{x=0}^{L}\int_{y=0}^{B} \exp\left(-\lambda\left(|\mathsf{R}_0^{\mathcal{P}} - (x + \mathrm{j}y)|W + \frac{\pi W^2}{4}\right)\right) \mathrm{d}y\mathrm{d}x.\end{aligned}$$

The mean number of interferers in a disk of radius $r_{\mathsf{B}}(\mathsf{R}_0^{\mathcal{P}})$ around $\mathsf{R}_0^{\mathcal{P}}$ is $\lambda\pi r_{\mathsf{B}}^2(\mathsf{R}_0^{\mathcal{P}})$, so that equating the mean number of strong interferers leads to

$$r_{\mathsf{B}}(\mathsf{R}_0^{\mathcal{P}}) = \left[\frac{\rho(\mathsf{R}_0)}{\pi\lambda}\right]^{\frac{1}{2}}. \tag{3.11}$$

We denote this disk around $\mathsf{R}_0^{\mathcal{P}}$ as $\mathcal{B}\left(\mathsf{R}_0^{\mathcal{P}}, r_{\mathsf{B}}(\mathsf{R}_0^{\mathcal{P}})\right)$. When $\mathsf{R}_0^{\mathcal{P}}$ is near the boundary of $\mathcal{P}$, parts of $\mathcal{B}\left(\mathsf{R}_0^{\mathcal{P}}, r_{\mathsf{B}}(\mathsf{R}_0^{\mathcal{P}})\right)$ lie outside $\mathcal{P}$. In such a scenario, given that the impact of reflections from the walls is significant, we continue to assume that $\mathcal{B}\left(\mathsf{R}_0^{\mathcal{P}}, r_{\mathsf{B}}(\mathsf{R}_0^{\mathcal{P}})\right)$ is a complete disk and allow T_i to lie outside $\mathcal{P}$. This is tantamount to modeling the wall reflections as signals emanating from shadow transmitters located at the reflection image locations corresponding to the actual strong interferers in $\mathcal{P}$. Note that when $\mathsf{R}_0^{\mathcal{P}}$ is close to a corner, there can be first and second order reflection sources within $\mathcal{B}\left(\mathsf{R}_0^{\mathcal{P}}, r_{\mathsf{B}}(\mathsf{R}_0^{\mathcal{P}})\right)$. For ease of analysis, we further assume that (reflection images and actual) strong interferers are independently and uniformly distributed within $\mathcal{B}\left(\mathsf{R}_0^{\mathcal{P}}, r_{\mathsf{B}}(\mathsf{R}_0^{\mathcal{P}})\right)$. This is illustrated in Fig 3.8.

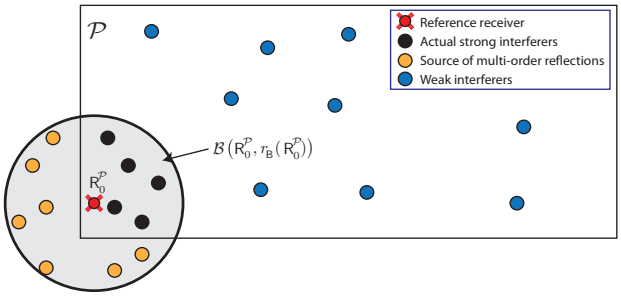

Figure 3.8: Plot showing the region $\mathcal{B}\left(\mathsf{R}_0^{\mathcal{P}}, r_{\mathsf{B}}(\mathsf{R}_0^{\mathcal{P}})\right)$, when the reference user is near a reflecting wall.

3.3.4.2 Self body-blockage

Self-blockage of the $\mathsf{T}_i - \mathsf{R}_0$ link occurs if $\mathsf{T}_i \in \mathcal{C}(\mathsf{B}_i)$ and/or $\mathsf{T}_i \in \mathcal{C}(\mathsf{B}_0)$. This results in a constant attenuation of B_{L} (linear scale), for each number of self-blockages. Such a model has been used in [38] in the context of mmWave cellular systems. In [38], self-blockage accounts for roughly 40 dB loss in SINR. Unlike the cellular case where the number of self-blockages in a link can be 0 or 1, in the mmWave wearables context, the number of self-blockages in a link can be either 0, 1 or 2. Self-blockage is the only source of blockage for strong interferers in our model. For a weak interferer, self-blockage further degrades the signal strength in addition to blockages due to other users. Hence, we assume the propagation is NLOS with a path-loss exponent $\alpha_{\mathsf{N}} > \alpha_{\mathsf{L}}$. If a weak interferer is not self-blocked, we assume the propagation path via ceiling reflection prevents the channel from being NLOS.

We summarize our blockage-based path-loss model for a general $\mathsf{T}_i \in \mathcal{P}$ next. The path length of the ceiling reflected signal from T_i to R_0 is denoted by

$$\|\mathsf{R}_0 - \mathsf{T}_i\|_c \;=\; \sqrt{|\mathsf{R}_0^{\mathcal{P}} - \mathsf{T}_i|^2 + (2d_{\mathsf{h}} - z_0)^2}, \tag{3.12}$$

and the Euclidean distance between T_i and R_0 is denoted by

$$\|\mathsf{R}_0 - \mathsf{T}_i\| \;=\; \sqrt{|\mathsf{R}_0^{\mathcal{P}} - \mathsf{T}_i|^2 + z_0^2}. \tag{3.13}$$

Denoting the number of self-blockages in the $\mathsf{T}_i - \mathsf{R}_0$ link by s and using $\mathbf{1}_A$ to denote the indicator function of event A, the path-loss function $\ell(\mathsf{R}_0, \mathsf{T}_i)$ can be classified into any one of the following:

Case A: When T_i is a strong interferer,

$$\ell(\mathsf{R}_0, \mathsf{T}_i) = \|\mathsf{R}_0 - \mathsf{T}_i\|^{-\alpha_{\mathsf{L}}} \mathsf{B}_{\mathsf{L}}^{-s}. \tag{3.14}$$

Case B: When T_i is a weak interferer

$$\ell(\mathsf{R}_0, \mathsf{T}_i) = \|\mathsf{R}_0 - \mathsf{T}_i\|_c^{-\alpha_{\mathsf{L}}} \mathbf{1}_{\{s=0\}} + \|\mathsf{R}_0 - \mathsf{T}_i\|^{-\alpha_{\mathsf{N}}} \mathbf{1}_{\{s\neq 0\}}. \tag{3.15}$$

Note that we do not consider the reflection from ceiling in Case A. This is in line with our assumption that when T_i is a strong interferer located within close proximity to $\mathsf{R}_0^{\mathcal{P}}$ in $\mathcal{P}$, the signal bouncing off the ceiling is less significant compared to the direct and wall-reflected signals. The effect of reflections from the ceiling is assumed to be substantial only when the users are facing each other and when $|\mathsf{R}_0^{\mathcal{P}} - \mathsf{T}_i| > r_{\mathsf{B}}(\mathsf{R}_0^{\mathcal{P}})$. The NLOS propagation in Case B-2 coarsely also accounts for all possible scattering and diffraction that dominates when an interferer is weak and self-blocked. This is the intuition behind the different cases for the path-loss function.

To conclude the discussion on interference and blockage modeling, we note that now we have a region $\mathcal{B}\left(\mathsf{R}_0^{\mathcal{P}}, r_{\mathsf{B}}(\mathsf{R}_0^{\mathcal{P}})\right)$ around $\mathsf{R}_0^{\mathcal{P}}$ such that the interference signal

(direct or wall-reflected) from T_i located within $\mathcal{B}\left(\mathsf{R}_0^{\mathcal{P}}, r_{\mathsf{B}}(\mathsf{R}_0^{\mathcal{P}})\right)$ is never blocked by $\mathsf{B}_j,\ j \neq i$. Further, the direct and wall-reflected paths for the interference from T_i outside $\mathcal{B}\left(\mathsf{R}_0^{\mathcal{P}}, r_{\mathsf{B}}(\mathsf{R}_0^{\mathcal{P}})\right)$ is always blocked by some user $j \neq i$.

3.4 SINR Coverage Probability

In this section, the reliability of the mmWave link of the reference user is characterized by evaluating the SINR distribution of the reference link as a function of the reference user's location within the enclosure. The SINR coverage probability for an SINR threshold γ is defined as the probability that the receiver SINR is greater than γ. Denoting the marked PPP as $\mathbf{\Phi}$, with the marks corresponding to fading power gains, distance-dependent pathloss and antenna gains, the SINR seen at the reference receiver R_0 when its body is facing in the direction ψ_0 is

$$\Gamma(\mathsf{R}_0, \psi_0) = \frac{h_0 G_{\mathsf{t}} G_{\mathsf{r}} d_0^{-\alpha_{\mathsf{L}}}}{\sigma^2 + \sum_{i \in \mathbf{\Phi}} G_{\mathsf{t},i} G_{\mathsf{r},i} h_i \ell(\mathsf{R}_0, \mathsf{T}_i)}. \tag{3.16}$$

Note that in (3.16), the term $\ell(\mathsf{R}_0, \mathsf{T}_i)$ captures the effect of the reference user's body orientation ψ_0 as defined in (3.14)-(3.15). Denoting $\tilde{\gamma} = \frac{d_0^{\alpha_{\mathsf{L}}}}{G_{\mathsf{t}} G_{\mathsf{r}}}$, the complementary cumulative distribution function (CCDF) of SINR, which is also referred to as the SINR coverage probability [12], is

$$\begin{aligned}\mathbb{P}\left(\Gamma(\mathsf{R}_0, \psi_0) > \gamma\right) &= \mathbb{P}\left(h_0 > \tilde{\gamma}\left(\sigma^2 + \sum_{i \in \mathbf{\Phi}} G_{\mathsf{t},i} G_{\mathsf{r},i} h_i \ell(\mathsf{R}_0 - \mathsf{T}_i)\right)\right) \\ &\leq 1 - \mathbb{E}_{\mathbf{\Phi}}\left[\left(1 - e^{-m\tilde{m}\tilde{\gamma}\left(\sigma^2 + \sum_{i \in \mathbf{\Phi}} G_{\mathsf{t},i} G_{\mathsf{r},i} h_i \ell(\mathsf{R}_0, \mathsf{T}_i)\right)}\right)^m\right]. \end{aligned} \tag{3.17}$$

In (3.17), we have used a tight lower bound for the CDF of the normalized gamma random variable [44], with $\tilde{m} = (m!)^{\frac{-1}{m}}$. Denoting

$$I_{\mathbf{\Phi}}^{\mathsf{SI}} = \sum_{i \in \mathcal{B}\left(\mathsf{R}_0^{\mathcal{P}}, r_{\mathsf{B}}(\mathsf{R}_0^{\mathcal{P}})\right)} G_{\mathsf{t},i} G_{\mathsf{r},i} h_i \ell(\mathsf{R}_0, \mathsf{T}_i) \text{ and} \tag{3.18}$$

$$I_{\mathbf{\Phi}}^{\mathsf{WI}} = \sum_{i \in \mathbf{\Phi} \setminus \mathcal{B}\left(\mathsf{R}_0^{\mathcal{P}}, r_{\mathsf{B}}(\mathsf{R}_0^{\mathcal{P}})\right)} G_{\mathsf{t},i} G_{\mathsf{r},i} h_i \ell(\mathsf{R}_0, \mathsf{T}_i), \tag{3.19}$$

and using the binomial expansion followed by splitting the strong and weak interference terms, we can write (3.17) as

$$\mathbb{P}\left(\Gamma(\mathsf{R}_0, \psi_0) > \gamma\right) = \sum_{k=1}^{m} \binom{m}{k} (-1)^{k+1} e^{-km\tilde{m}\tilde{\gamma}\sigma^2} \mathbb{E}_{\mathbf{\Phi}}\left[e^{-km\tilde{m}\tilde{\gamma} I_{\mathbf{\Phi}}^{\mathsf{SI}}}\right] \mathbb{E}_{\mathbf{\Phi}}\left[e^{-km\tilde{m}\tilde{\gamma} I_{\mathbf{\Phi}}^{\mathsf{WI}}}\right]. \tag{3.20}$$

The expectation terms in (3.20) are as given in Theorem 4 and Theorem 5, which make use of the following lemmas.

Lemma 2 *The probability p_s that $\mathsf{T}_i \in \mathcal{B}\left(\mathsf{R}_0^{\mathcal{P}}, r_{\mathsf{B}}(\mathsf{R}_0^{\mathcal{P}})\right)$ experiences s human body self blockages is given by*

$$p_s = \begin{cases} (1 - p_{\mathsf{b}}^{\text{self}})^2 & s = 0 \\ 2p_{\mathsf{b}}^{\text{self}}(1 - p_{\mathsf{b}}^{\text{self}}) & s = 1 \\ \left(p_{\mathsf{b}}^{\text{self}}\right)^2 & s = 2 \end{cases}, \tag{3.21}$$

where $p_{\mathsf{b}}^{\text{self}} = \frac{1}{\pi} \arcsin\left(\frac{W}{2d}\right)$, and the probability $q(\mathsf{R}_0, \psi_0)$ that both T_i and R_0 are facing each other when $\mathsf{T}_i \in \mathcal{P} \setminus \mathcal{B}\left(\mathsf{R}_0^{\mathcal{P}}, r_{\mathsf{B}}(\mathsf{R}_0^{\mathcal{P}})\right)$ is given by

$$q(\mathsf{R}_0, \psi_0) = \left(1 - p_{\mathsf{b}}^{\text{self}}\right)\left(1 - q_1(\mathsf{R}_0, \psi_0)\right), \tag{3.22}$$

where

$$q_1(\mathsf{R}_0, \psi_0) = \frac{|\mathcal{C}(\mathsf{B}_0) \setminus \mathcal{B}\left(\mathsf{R}_0^{\mathcal{P}}, r_{\mathsf{B}}(\mathsf{R}_0^{\mathcal{P}})\right)|}{LB - |\mathcal{P} \cap \mathcal{B}\left(\mathsf{R}_0^{\mathcal{P}}, r_{\mathsf{B}}(\mathsf{R}_0^{\mathcal{P}})\right)|}, \tag{3.23}$$

with L and B denoting the dimensions of the enclosed region.

Proof: See Appendix A.1. □

The term $q_1(\mathsf{R}_0, \psi_0)$ in (3.23) denotes the probability that a weak interferer is in the blocking cone of B_0 given that it lies outside $\mathcal{B}\left(\mathsf{R}_0^{\mathcal{P}}, r_{\mathsf{B}}(\mathsf{R}_0^{\mathcal{P}})\right)$ in $\mathcal{P}$. This probability is obtained as the ratio of the two areas given in the numerator and denominator in (3.23). Note that, for a given $\mathcal{B}\left(\mathsf{R}_0^{\mathcal{P}}, r_{\mathsf{B}}(\mathsf{R}_0^{\mathcal{P}})\right)$ (computed using (3.11)), these areas (3.23) need to be evaluated via numerical integration.

We use the following notation ((3.24) - (3.27)) in Lemma 3:

$$r_{\max} = z_0 \cot\left(\phi_0^{(\mathsf{e})} - \frac{\theta_{\mathsf{r}}^{(\mathsf{e})}}{2}\right), \tag{3.24}$$

$$r_{\min} = z_0 \cot\left(\phi_0^{(\mathsf{e})} + \frac{\theta_{\mathsf{r}}^{(\mathsf{e})}}{2}\right). \tag{3.25}$$

Quantities in (3.24) and (3.25) together define a region in $\mathcal{P}$ which falls within the elevation beam-width of reference receiver's antenna.

$$\hat{\mathcal{P}} = \mathcal{P} \setminus \mathcal{B}\left(\mathsf{R}_0^{\mathcal{P}}, r_{\mathsf{B}}(\mathsf{R}_0^{\mathcal{P}})\right) \text{ and} \tag{3.26}$$

$$\Upsilon(\phi_0^{(\mathsf{a})}) = \left\{ z \in \hat{\mathcal{P}} : \measuredangle z \in \left[\phi_0^{(\mathsf{a})} - \frac{\theta_{\mathsf{r}}^{(\mathsf{a})}}{2}, \phi_0^{(\mathsf{a})} + \frac{\theta_{\mathsf{r}}^{(\mathsf{a})}}{2}\right] \right\}. \tag{3.27}$$

The set in (3.27) denotes a region outside $\mathcal{B}\left(\mathsf{R}_0^{\mathcal{P}}, r_{\mathsf{B}}(\mathsf{R}_0^{\mathcal{P}})\right)$ in $\mathcal{P}$ that falls in the main-lobe of the reference receiver in the azimuth.

Lemma 3 *The probability $p_{\mathrm{rx}}^{\mathsf{SI}}$ that a strong interferer is within the main-lobe of the reference receiver is*

$$p_{\mathrm{rx}}^{\mathsf{SI}} = \frac{\theta_{\mathsf{r}}^{(\mathsf{a})}}{2\pi}\left(\frac{\min\left(r_{\mathsf{B}}(\mathsf{R}_0^{\mathcal{P}}), r_{\max}\right)^2 - r_{\min}^2}{r_{\mathsf{B}}^2(\mathsf{R}_0^{\mathcal{P}})}\right). \tag{3.28}$$

The probability $p_{\text{rx}}^{\mathsf{WI}}$ *that a weak interferer is within the main-lobe of the reference receiver is*

$$p_{\text{rx}}^{\mathsf{WI}} = \frac{|\Upsilon(\phi_0^{(\mathsf{a})})|}{|\hat{\mathcal{P}}|}\left(1 - \frac{|\mathcal{P} \setminus \mathcal{B}\left(\mathsf{R}_0^{\mathcal{P}}, \max(r_{\mathsf{B}}(\mathsf{R}_0^{\mathcal{P}}), r_{\mathsf{max}})\right)|}{|\mathcal{P} \setminus \mathcal{B}\left(\mathsf{R}_0^{\mathcal{P}}, r_{\mathsf{B}}(\mathsf{R}_0^{\mathcal{P}})\right)|}\right). \tag{3.29}$$

Proof: See Appendix A.2. □

In (3.29), areas of regions have to be evaluated numerically. We define the following vectors for ease of notation in Theorem 4 and Theorem 5:

$$\mu = \begin{bmatrix} p_{\mathsf{M}} p_{\text{rx}}^{\mathsf{SI}} \\ (1-p_{\mathsf{M}})\, p_{\text{rx}}^{\mathsf{SI}} \\ p_{\mathsf{M}}\left(1 - p_{\text{rx}}^{\mathsf{SI}}\right) \\ (1-p_{\mathsf{M}})\left(1 - p_{\text{rx}}^{\mathsf{SI}}\right) \end{bmatrix}, \quad \nu = \begin{bmatrix} p_{\mathsf{M}} p_{\text{rx}}^{\mathsf{WI}} \\ (1-p_{\mathsf{M}})\, p_{\text{rx}}^{\mathsf{WI}} \\ p_{\mathsf{M}}\left(1 - p_{\text{rx}}^{\mathsf{WI}}\right) \\ (1-p_{\mathsf{M}})\left(1 - p_{\text{rx}}^{\mathsf{WI}}\right) \end{bmatrix}, \tag{3.30}$$

$$\mathcal{G} = \begin{bmatrix} G_{\mathsf{t}}G_{\mathsf{r}} & g_{\mathsf{t}}G_{\mathsf{r}} & G_{\mathsf{t}}g_{\mathsf{r}} & g_{\mathsf{t}}g_{\mathsf{r}} \end{bmatrix}. \tag{3.31}$$

We use subscript j to denote a vector's j^{th} entry.

Theorem 4 *Denoting* $\tilde{R} = r_{\mathsf{B}}(\mathsf{R}_0^{\mathcal{P}})$ *for simplicity, and*

$$A_{j,s} = \frac{\tilde{R}^2}{2} - \int_0^{\tilde{R}} \left(1 + \frac{k\tilde{m}\tilde{\gamma}\mathcal{G}_j}{(r^2 + z_0^2)^{\frac{\alpha_{\mathsf{L}}}{2}}\, \mathsf{B}_{\mathsf{L}}^s}\right)^{-m} r\mathsf{d}r, \tag{3.32}$$

the expectation term corresponding to the strong interferers in (3.20) *can be expressed as follows*

$$\begin{aligned} \mathbb{E}_{\mathbf{\Phi}}\left[e^{-km\tilde{m}\tilde{\gamma}I_{\mathbf{\Phi}}^{\mathsf{SI}}}\right] &= \exp\left[-2\pi\lambda\left(p_0\sum_{j=1}^{4}\mu_j A_{j,0} + \frac{p_1}{2}\sum_{j=1}^{4}\mu_j A_{j,1}\right.\right. \\ &\quad \left.\left. + \frac{p_1}{2\left(1-p_{\text{rx}}^{\mathsf{SI}}\right)}\sum_{j=3}^{4}\mu_j A_{j,1} + \frac{p_2}{\left(1-p_{\text{rx}}^{\mathsf{SI}}\right)}\sum_{j=3}^{4}\mu_j A_{j,2}\right)\right]. \end{aligned} \tag{3.33}$$

Proof: See Appendix A.3. □

Theorem 5 *Defining*

$$C_1 = |\hat{\mathcal{P}}| - \sum_{j=1}^{4} \nu_j \int_{z \in \hat{\mathcal{P}}} \left(1 + \frac{k\tilde{m}\tilde{\gamma}\mathcal{G}_j}{\|\mathsf{R}_0 - z\|_c^{\alpha_\mathsf{L}}}\right)^{-m} \mathsf{d}z, \tag{3.34}$$

$$\& \; C_2 = |\hat{\mathcal{P}}| - \sum_{j=3}^{4} \frac{\nu_j}{(1 - p_{\mathrm{rx}}^{\mathsf{WI}})} \int_{z \in \hat{\mathcal{P}}} \left(1 + \frac{k\tilde{m}\tilde{\gamma}\mathcal{G}_j}{\|\mathsf{R}_0 - z\|^{\alpha_\mathsf{N}}}\right)^{-m} \mathsf{d}z, \tag{3.35}$$

the expectation term corresponding to the weak interferers in (3.20) *simplifies to*

$$\mathbb{E}_{\mathbf{\Phi}}\left[e^{-km\tilde{m}\tilde{\gamma}I_{\mathbf{\Phi}}^{\mathsf{WI}}}\right] = \exp\left[-\lambda\left(q(\mathsf{R}_0, \psi_0)C_1 + (1 - q(\mathsf{R}_0, \psi_0))C_2\right)\right]. \tag{3.36}$$

Proof: See Appendix A.4. □

To evaluate the analytic plots of the SINR distribution for a given network dimension and user density, the threshold distance $r_{\mathsf{B}}(\mathsf{R}_0^{\mathcal{P}})$ is first computed for a given R_0. Next, based on the given body orientation ψ_0 of the reference user, the self blocking probability and the probability that an interferer falls in the main-lobe of the reference receiver are computed analytically for the strong interferers (using (3.21) and (3.28), respectively). The corresponding quantities for the weak interferers are computed using geometry and numerical integration based on (3.23) and (3.29). Using these computations and plugging the results from Theorem 1 and Theorem 2 ((3.33) and (3.36)) into (3.20), we compute the spatially averaged SINR coverage probability for a given receiver location R_0 and orientation angle ψ_0. Note that the results implicitly incorporate the direction in 3D where the receiver antenna is pointed, i.e., $(\phi_0^{(\mathsf{a})}, \phi_0^{(\mathsf{e})})$, though we do not explicitly denote that in (3.20). The spectral efficiency $\eta(\mathsf{R}_0, \psi_0)$ for a given SINR can be computed as $\log_2(1 + \Gamma(\mathsf{R}_0, \psi_0))$. With the knowledge of the CCDF of SINR, the ergodic spectral efficiency $\mathbb{E}[\eta(\mathsf{R}_0, \psi_0)]$

Table 3.1: Default values of parameters used for simulation

Parameter	Value	Description
L	15 m	Length of the enclosure
B	5 m	Breadth of the enclosure
H	2.5 m	Height of the enclosure
d_{h}	1.5 m	Transmitters' vertical distance from ceiling
W	0.45 m	Width of user body
d	0.325 m	Distance between body center and wearable
z_0	0.5 m	Height at which receiver is positioned
r_0	0.2345 m	Horizontal separation between R_0 and T_0
λ	2 m^{-2}	Crowd density
α_{L}	2	LOS path-loss exponent
α_{N}	4	NLOS path-loss exponent
m	7	Nakagami parameter of small scale fading
B_{L}	40 dB	Self-body blockage loss

of the reference user's communication link can be evaluated as a function of the reference receiver location and orientation of its body.

3.5 System Validation and Plots

In this section, simulation and numerical results that shed insights into the proposed model are discussed. Simulation results to validate the analytic expressions for spatial averages are also provided in this section. The parameters used for the results are summarized in Table 3.1. The default value used for $r_0 = \sqrt{d^2 - \left(\frac{W}{2}\right)^2}$, so that the reference signal link is unblocked by the reference user's body. This is also shown in Table 3.1. The values of the reference antenna pointing angles ϕ_0^{a} and ϕ_0^{e} are computed according to (3.2) and (3.4).

3.5.1 Validation of the Analytic Model via Simulation

The expression derived in Section 3.4, is validated against simulation and is shown in Fig. 3.9. As discussed earlier, the impact of reflections due to the walls of the enclosure is non-trivial for the indoor mmWave wearable network setting. Therefore, to obtain the simulation plots, phantom transmitters and user bodies were assumed to be located at the mirror image locations of the actual interferers and their corresponding human body locations, respectively using using ray optics. This effectively modeled the impact of reflection due to the walls and the ceiling of the enclosure $\mathcal{T}$ similar to [17]. To see if an interferer (actual or phantom transmitter) is blocked from the reference user's receiver, the approach elaborated in [1] was used. Note that we do not account for the actual reflection coefficient associated with the walls which is a function of the angle of incidence of the signal. Analysis in [17], however, shows that for highly reflective surfaces, the reflection coefficient is close to unity and more or less independent of the angle of incidence. Hence, merely placing phantom transmitters at the mirror image locations and assuming the same transmit power as that of the actual interferers are justified. The CCDF of the SINR is then obtained by averaging the random geometry of the user locations, small scale fading and random body orientation of the interfering users. It is seen that the analytic expression for the upper bound of SINR coverage probability is very tight and matches the simulation results very well.

Fig. 3.9 also shows the SINR distribution for different antenna configurations. It is seen that having larger antenna gains and highly directed transmissions and reception improve the performance significantly. This is because directional antennas

reduce the probability that interferers point their main-lobes in the direction of the reference receiver's antenna main-lobe, thus reducing the effective interference, while boosting the antenna gains in the reference signal link.

3.5.2 Numerical Results

A plot of the mean number of strong interferers as a function of the location of the reference receiver is shown in Fig. 3.10. When the reference receiver is near the walls of the enclosure, the mean number of strong interferers is lower compared to that when at the center. This implies that reflections due to the walls are less significant than the direct interference caused by other users when the user density is high.

The dependence of system performance on the reference user body orientation is studied by plotting the average achievable rate for the cases when the reference user is at the center and near a corner (we assume $\mathsf{R}_0^{\mathcal{P}} = 0.5 + \mathrm{j}0.5$ in this case). For this, the analytic expressions derived in Section 3.4 are used to compute the ergodic spectral efficiency of the reference link. The average achievable rate is then computed by multiplying the ergodic spectral efficiency with the system bandwidth which is taken to be 2.16 GHz assuming an IEEE 802.11ad like setup. The plots are shown in Fig. 3.11 for omni-directional antennas at the transmitters and the receivers, from which we see that the sensitivity to body orientation is more pronounced when the reference user is at corner. This means that when at a corner, turning the body to face away from the interfering crowd ($\psi_0 = 225^o$ for $\mathsf{R}_0^{\mathcal{P}} = 0.5 + \mathrm{j}0.5$) gives the best performance thanks to the body blockage due to the reference user's body for the

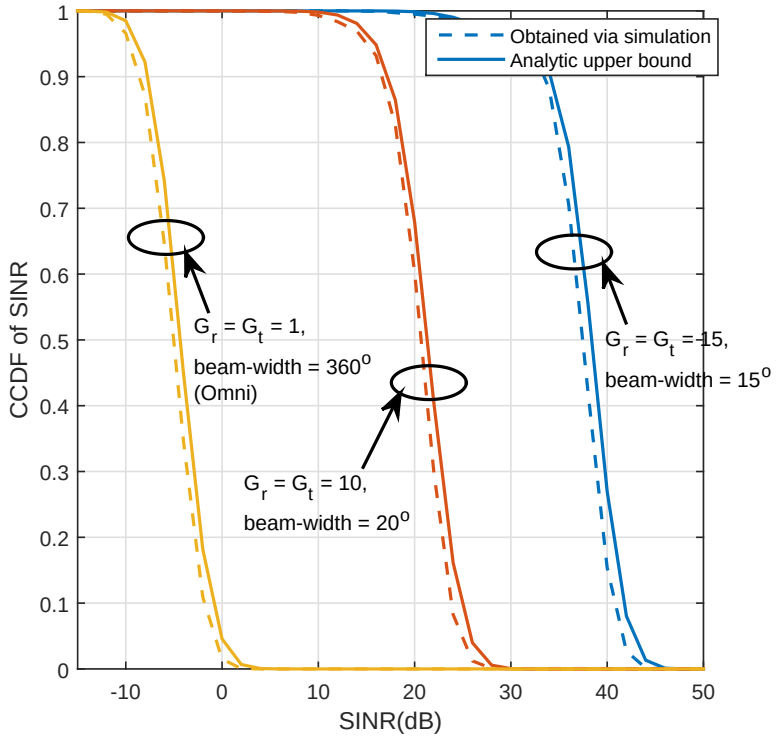

Figure 3.9: SINR distribution obtained through simulation and analytic expression when the receiver is at a corner $0.5 + \mathrm{j}0.5$ for different antenna configurations. Our proposed analytic model match well with simulation results which account for random geometry for interfering users, reflections due to the finite enclosure and small scale fading. With directional antennas, significant improvement in performance is seen.

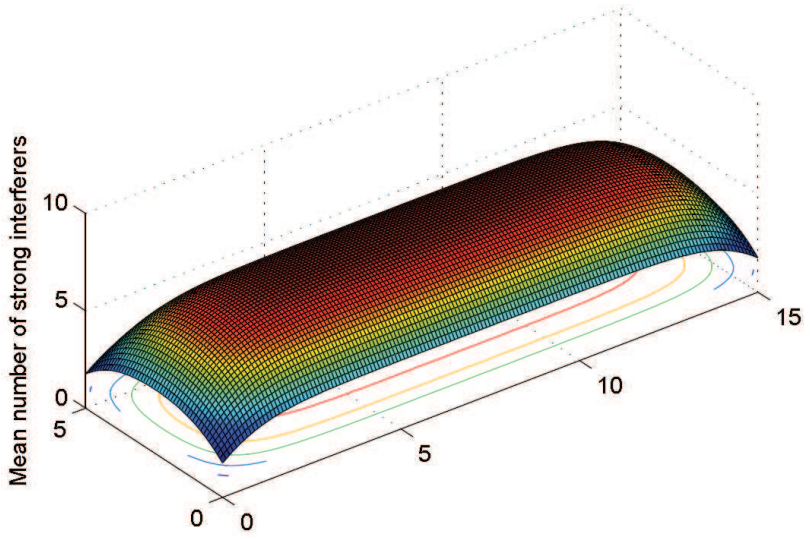

Figure 3.10: Plot showing the variation in the mean number of strong interferers seen be the reference user at various locations within the enclosure. The mean number of strong interferers is smaller when the reference user is near the walls of the enclosed region.

mmWave interference signals.

The performance of the reference link as the reference user is positioned at various locations of the enclosure is investigated next. The location dependent SINR coverage probability is shown in Fig. 3.12 in the form of a heat map which is a graphical representation of data where the individual values contained in a matrix are represented as colors. In Fig. 3.12, an SINR threshold of -5 dB and $\psi_0 = 0^o$ are assumed for representing the SINR coverage probability as a color at reference receiver location in $\mathcal{P}$ (projection) specified by the x and y coordinates. It is seen that the best performance is obtained when the reference receiver is near the corner and facing away from the interfering crowd. This is the case when all the interferers are shielded by the reference user's body. From Fig. 3.12 we can also see how the

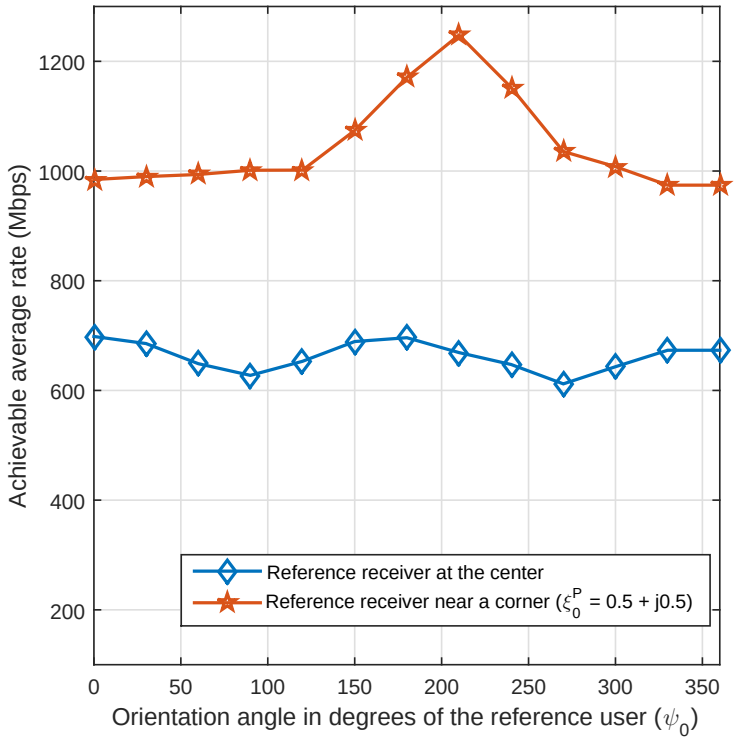

Figure 3.11: Plot showing the variation in the average achievable rate as a function of the body orientation of the reference user when located at the center and near a corner assuming omni-directional antennas are used at the devices. When the reference user is at the corner location, body orientation plays a significant role in improving achievable rate.

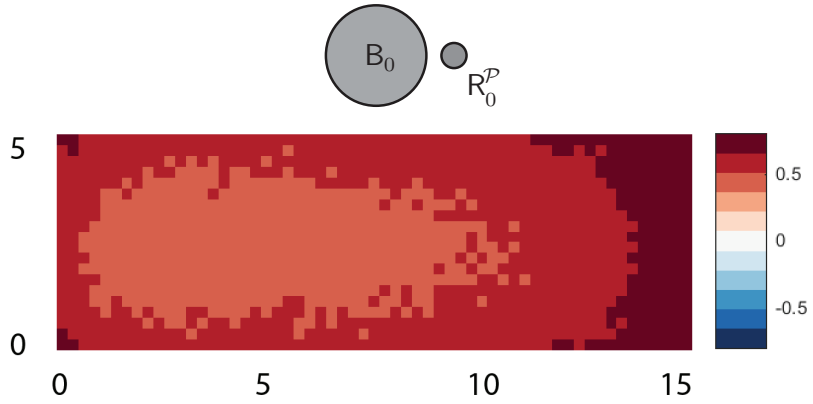

Figure 3.12: Plot showing SINR coverage probability heat map as a function of the reference location position when the reference user is facing to the right, i.e. $\psi_0 = 0^o$ and with omni-directional transceivers. The body orientation of the reference user is also shown in the figure. System performance of mmWave wearable networks in dense indoor environments heavily depends on the location.

interplay of reference user's body blockage and the reflections from the enclosure result in significant variation in the performance seen at the reference receiver as the user moves around the crowd.

The dependence of system performance with respect to d, the relative separation between the user body and the wearable device is shown in Fig. 3.13 for omni-directional antennas used at the devices. We let $\mathsf{R}_0^{\mathcal{P}} = 0.5 + \mathrm{j}4.5$ which is a corner location and take $\psi_0 = 135^o$ so that the user is facing away from the interfering crowd. The plots in Fig. 3.13 show that for getting improved performance in a crowded environment, the device must be positioned closer to the user. This is because the self-body blockage better helps in attenuating the interference from other wearable networks when wearable devices are held close to the user body.

To understand the interplay between the horizontal and vertical separation

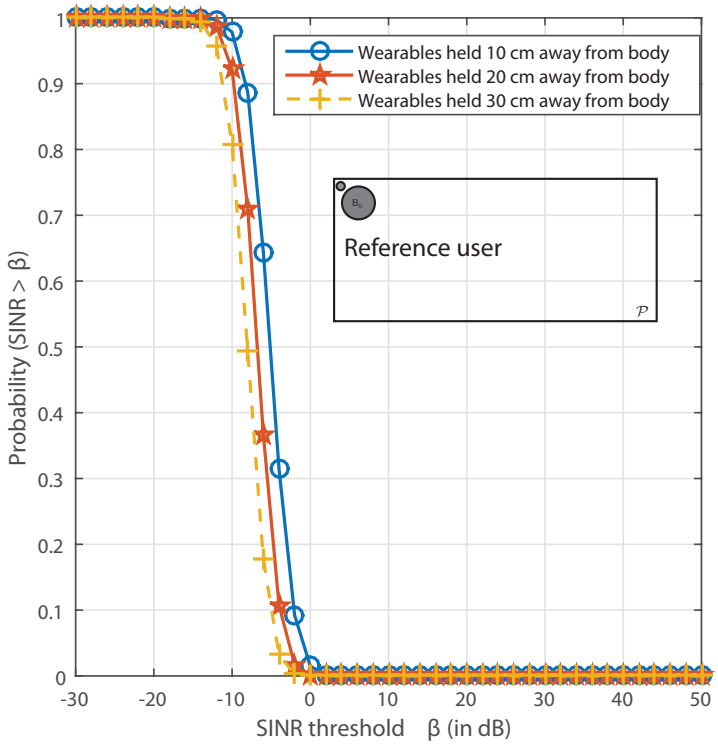

Figure 3.13: Plot showing the variation in system performance as a function of the relative separation between the user body and the wearable device. $\mathsf{R}_0^{\mathcal{P}}$ is assumed to be located at $0.5 + \mathrm{j}4.5$ (see inset picture) and the transceivers are assumed to be omni-directional. Holding the wearable devices closer to the human body improves the SINR coverage probability.

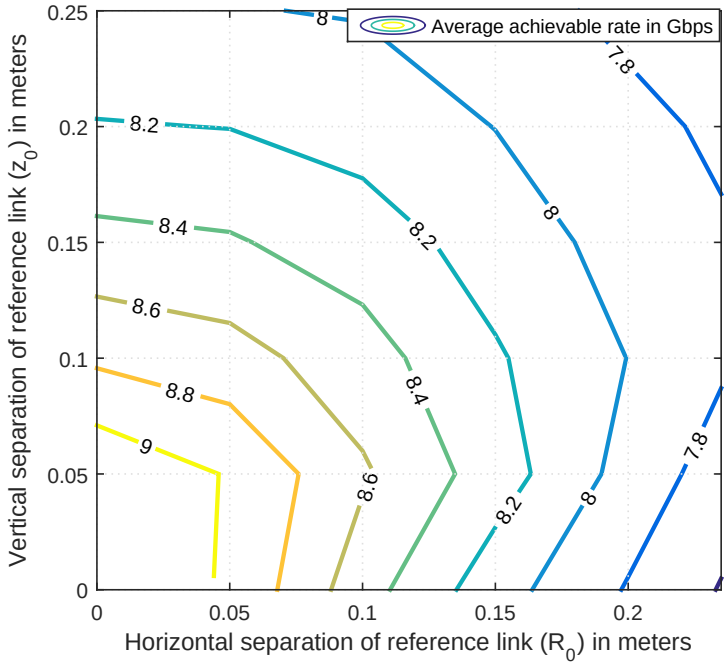

Figure 3.14: Contour plot showing the variation in average achievable rates in Gbps as a function of the horizontal and vertical separation distance between the reference receiver and reference transmitter. Vertically positioning the reference transmitter (below) and receiver (above) gives the best ergodic rate performance.

distance of the reference link, we show a contour plot of the average achievable rate in Fig. 3.14 as a function of the horizontal separation r_0 and the vertical separation z_0 of the reference signal link when the reference user is at the center of the enclosure. It is seen that the combination $z_0 > 0$ and $r_0 = 0$ gives the best performance. This scenario corresponds to having the reference receiver vertically placed above the reference receiver. It can also be seen from Fig. 3.14 that when $r_0 > 0$, having z_0 slightly above 0 is more advantageous than having $z_0 = 0$, i.e., having both the receiver and transmitter in the same plane ($\mathcal{P}$) is not recommended for rate performance as this scenario does not utilize the receiver antenna directivity in the elevation plane. The results in Fig. 3.14 assume $G_{\mathsf{r}} = G_{\mathsf{t}} = 10$, $g_{\mathsf{r}} = g_{\mathsf{t}} = 0.5$ and beam-width $= 20^o$ in the azimuth and elevation. We also assume the reference receiver is located at the center and facing towards right (i.e., $\psi_0 = 0$).

The variation of SINR coverage probability for an SINR threshold of $\gamma = 32$ dB as the self-body blockage loss $\mathsf{B_L}$ is varied is shown in Fig. 3.15 when $\psi_0 = 0$. We let $G_{\mathsf{r}} = G_{\mathsf{t}} = 15$, $g_{\mathsf{r}} = g_{\mathsf{t}} = 0.1$ and beam-width $= 15^o$ in the azimuth and elevation. Two locations - one near a corner $(12.5 + \mathrm{j}0.5)$ and at the center are considered in Fig. 3.15. It is observed that while increasing $\mathsf{B_L}$ improves the coverage probability of the reference signal link, the improvement is higher when the reference receiver is at the center. This is because, since the amount of interference is more pronounced at the center, the self-blody blockage shields the reference signal better thus resulting in better SINR performance improvement compared to a corner location.

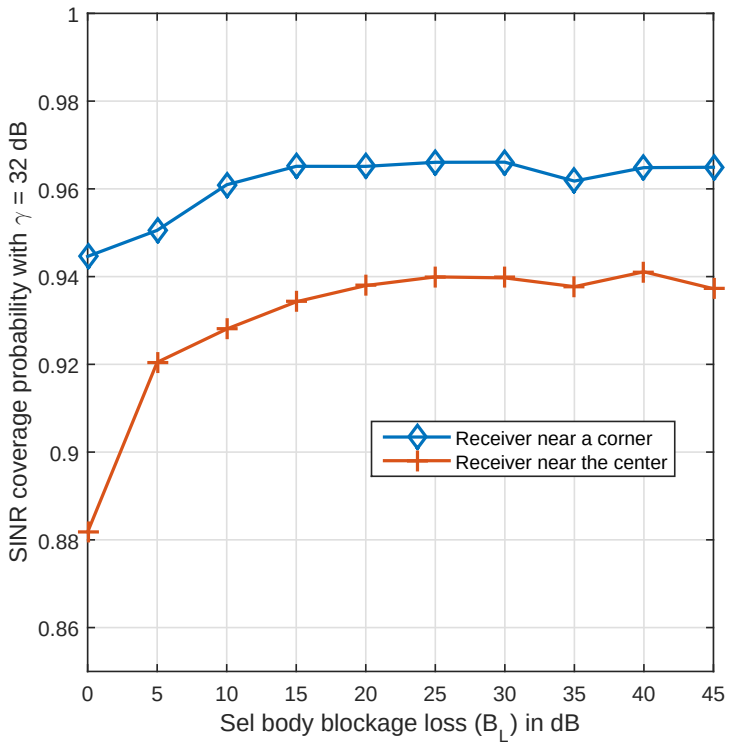

Figure 3.15: Plot showing the variation of SINR coverage probability as the self-blockage attenuation $\mathsf{B_L}$ is varied. Larger $\mathsf{B_L}$ is more helpful when the reference user is at the center.

3.6 Conclusions

In this chapter, we developed a tractable system model to analyze the performance of mmWave-based wearable network in a densely crowded indoor environment when there is no coordination between users to control interference. We modeled the effects of human-body blockages due to other users and also the reference user. The proposed system model also captured the predominant effects of wall and ceiling reflections when the user density is high. The proposed analytic model is validated against simulations. Using the proposed path-loss model, we derived closed-form expressions for spatially averaged system performance in terms of SINR coverage and rate that can be computed as a function of location and body orientation of the reference user. We observed that the effect of body orientation is significant when the reference user is located at a corner. The peak average rate for the system was obtained when the reference user is near the corner and facing away from the interferers. Further, since the net interference is enhanced due to reflections from walls and ceiling during indoor mmWave wearable operation, it is seen that channel knowledge and correctly pointing the beams are critical while still assuming there is no coordination across users as concluded from Chapter 2. We showed that when the reference receiver is placed vertically above the reference transmitter, maximum gain in performance is obtained using narrow beam directional antennas at the transmitter and receiver.

Chapter 4

Channel Estimation for Hybrid Architecture Based Wideband Millimeter Wave Systems

4.1 Overview

Hybrid analog and digital precoding allows millimeter wave (mmWave) systems to achieve both array and multiplexing gain. The design of the hybrid precoders and combiners, though, is usually based on knowledge of the channel. Prior work on mmWave channel estimation with hybrid architectures focused on narrowband channels. Since mmWave systems will be wideband with frequency selectivity, it is vital to develop channel estimation solutions for hybrid architectures based wideband mmWave systems. In this chapter[1], we develop a sparse formulation and compressed sensing based solutions for the wideband mmWave channel estimation problem for hybrid architectures. First, we leverage the sparse structure of the frequency selective mmWave channels' representation and formulate the channel estimation problem as a sparse recovery in both time and frequency domains. Then, we propose explicit channel estimation techniques for purely time or frequency domains and for combined

[1]This chapter is based on the work accepted for publication in the journal paper: K. Venugopal, A. Alkhateeb, N. González-Prelcic and R. W. Heath, Jr., "Channel Estimation for Hybrid Architecture Based Wideband Millimeter Wave Systems," IEEE Journal of Selected Areas in Communications, special issue on "Millimeter wave communications for future mobile networks", March 2017. This work was supervised by Prof. Robert Heath. Dr. Ahmed Alkhateeb and Prof. Nuria González-Prelcic gave important feedback related to the development and presentation of the ideas.

time/frequency domains. Simulation results show that the proposed solutions achieve good channel estimation quality, while requiring small training overhead. Leveraging the hybrid architecture at the transceivers gives further improvement in estimation error performance and achievable rates.

4.2 Introduction

Channel estimation in millimeter wave MIMO systems allows flexible design of hybrid analog/digital precoders and combiners under different optimization criteria. Unfortunately, the hybrid constraint makes it challenging to directly estimate the channels, due to the presence of the analog beamforming / combining stage to avoid the power consumption of the typical all-digital solution used at lower frequencies [55–57]. Further, operating at mmWave frequencies complicates the estimation of the channel because the signal-to-noise-ratio (SNR) before beamforming is low and the dimensions of the channel matrices associated with mmWave arrays [55, 58] are large. While mmWave channel estimation has extensively been studied in the last few years, most prior work assumed a narrowband channel model. Since mmWave systems are attractive due to their wide bandwidth, developing efficient mmWave channel estimation for frequency-selective channels is of great importance.

To avoid the explicit estimation of the channel, analog beam training solutions were proposed [59–61]. In beam training, the transmitter and receiver iteratively search for the beam pair that maximizes the link SNR [59, 61, 62]. This approach is used in IEEE standards like 802.11ad [11] and 802.15.3c [63]. The directional antenna patterns can be realized using a network of phase shifters. While analog beam

training works for both narrowband and wideband systems, the downside is that the solution supports mainly a single communication stream; extensions to multi-stream and multi-user communication are possible but generally incur much higher overhead.

Exploiting sparsity has been critical in formulating practical channel estimators in the hybrid MIMO architecture [57,64]. The reason is that the analog precoding and combing stages act to perform spatial compression, reducing the dimensions of the channel observed in the digital domain compared to the channel at the antennas. When sparsity is employed, a succession of different precoders and combiners are used to make the compressive measurements. Then, decomposing the uncompressed channel to expose the dictionary in which the channel parameters are sparse, an optimization problem is solved to determine the locations of the sparse coefficients and their values. This approach is different from beam training [59,61,62], which attempts to find the beams that point in the most promising directions and not estimating the channel. In compressive methods, the analog beamformers and combiners are selected to make measurements in several directions.

There are several solutions for compressive channel estimation in frequency-flat mmWave channels [64–72]. In the frequency-flat, narrowband case, the sparsity in the angular domain is exploited by making use of the extended virtual channel model [55]. Essentially, the MIMO channel is written in terms of dictionary matrices built from the transmit and receive steering vectors evaluated on a uniform grid of possible angles of arrival and departure (AoA/AoD). These dictionary matrices operate as a sparsifying basis for the channel matrix. Using that formulation, several channel estimation algorithms that use compressed sensing (CS) tools have been developed for

hybrid architectures [64–68], where the training / measurement matrices are designed using hybrid precoders and combiners. These techniques differ in the way these measurement matrices search for the dominant angles of arrival and departure. Solutions that make use of adaptive compressed sensing [64, 69, 70], random compressed sensing [65–67, 71, 72], joint random and adaptive compressed sensing [67] were studied. Other non-compressed sensing techniques were also developed for mmWave channel estimation using subspace estimation [73], overlapped beams [74], and auxiliary beams [75]. A main limitation of [64–67, 73–75] is that mmWave channel bandwidths will be large (in fact the main motivation for using millimeter wave) and the underlying channels are better modeled as frequency-selective.

In this chapter, we propose and evaluate a new approach for estimating wideband mmWave channels based on sparse recovery. Unlike prior work for narrowband and frequency-flat channels [64–67, 73–75], we redefine the sparsifying dictionaries to account for the sparse nature of wideband frequency-selective mmWave channels in both the angular and the delay domains. Our formulation explicitly accounts for bandlimiting filtering, which spreads the contributions of multi-paths in the channel among several discrete-time channel taps. Once the channel is written in terms of the sparsifying dictionary matrices, the hardware constraints associated with the analog precoding stage are also introduced into the formulation of the channel estimation problem. This allows application of various algorithms on sparse reconstruction from the CS literature.

In formulating our algorithm, we incorporate key system constraints associated with the analog precoders and combiners. As with prior work in the narrowband

case [66], we assume that the precoders and combiners are frequency flat and are generated using a fully connected architecture with digitally controlled quantized phase shifters. Unlike other work, though, we also account for the finite switching time required to reconfigure the phase shifters from one value to another [76]. As a result, our proposed system performs training using a series of zero-padded Single Carrier - Frequency Domain Equalization (SC-FDE) frames or Orthogonal Frequency-Division Multiplexing (OFDM) symbols. Each SC-FDE frame or OFDM symbol is transmitted using a single analog precoder and received with a single analog combiner; the analog portions are reconfigured during the guard interval. By using zero padding instead of a cyclic prefix, the distortion incurred during switching can be neglected. This changes the effective received signal model and means that prior work assuming the usual cyclic prefix during training like [77–79] does not apply. To the best of our knowledge there are no prior work on wideband millimeter channel estimation that identify the hardware limitations and the subsequent signal processing necessary to circumvent them. The main contributions of this chapter are summarized next.

We define an appropriate sparsifying dictionary for frequency-selective mmWave channels. This dictionary depends on the transmit and receive array steering vectors evaluated on a uniform grid of possible AoAs/AoDs, and also on a band-limiting filter evaluated on a uniform grid of possible delays. This key step leads to a sparse representation of the MIMO channel matrix in both the angular and delay domains. Unlike the prior work in [77, 79], we do not limit the channel model to a virtual channel model, wherein the sparsifying dictionary is square. Note that with the virtual channel model, the additional step of shaping may be used to avoid the error due to

quantization, as elaborated in [79]. Our representation is more general and gives better flexibility to define the sparsifying dictionary to get the required level of accuracy for the channel estimates.

We present an algorithm for estimating the wideband mmWave channel in the time-domain. Important practical features critical for mmWave system modeling are incorporated in our sparse formulation. The proposed formulation simultaneously leverages the structure of the frequency-selective large antenna mmWave channel in both the delay and angular domains. This avoids the multiple measurement problem in the frequency-domain. Unlike prior work which either relies on fully-digital and/or OFDM systems for wideband channel estimation [77–79], our proposed approach works both for SC-FDE and OFDM based frequency-selective hybrid mmWave systems. To our knowledge there is no previous work in mmWave channel estimation that also uses a grid in the delay domain along with the angle domain.

We present an algorithm for estimating the wideband mmWave channel in the frequency-domain, for an OFDM system. A critical step in this formulation is the use of zero padding, instead of cyclic prefixing. Zero padding helps analog circuitry reconfiguration from one OFDM symbol to the next, without corrupting the training data at the symbol edges. Most prior work, including [77, 78], did not exploit the fact that baseband channel is band-limited and assumed perfect frequency domain equalization, or OFDM where the cyclic prefixing is not corrupted – thanks to perfect analog circuitry reconfiguration. Note also that not considering the band-limiting filter response in the effective baseband channel model artificially enhances the sparsity level in the channel as we explain later in the manuscript. In practice, these

constraints necessitate additional change in the receiver chain, making the proposed frequency-domain formulation of the channel estimation problem novel.

We propose explicit algorithms to solve the sparse recovery problems in (1) purely time-domain, (2) purely frequency-domain, and (3) combined time-frequency domains. The different approaches proposed in this chapter can be suitably used for different scenarios based on system level constraints and implementation. Our proposed time-domain algorithms leverage the dictionary formulation that accounts for the sparsity in the delay domain, while the frequency-domain techniques work independent of the delay domain sparsity constraints. These proposed algorithms could serve as a baseline for future work that model a practical hardware-constrained wideband mmWave hybrid system.

It is explained through simulation results that the proposed algorithms require significantly less training than when beam training (eg. IEEE 802.11ad) is used for estimating the dominant angles of arrival and departure of the channel. A strict comparison with existing beam training algorithms in terms of rate performance is not reasonable since they focus, not on estimating the explicit frequency selective mmWave MIMO channel, but on estimating beam pairs that give good link SNR. Ensuring low estimation error rates in our proposed algorithms, however, implies that efficient hybrid precoders and combiners can be designed to support rates similar to all-digital solutions [80]. We therefore rely mainly on the average error rates to compare the efficiency of our approaches. We show that utilizing multiple RF chains at the transceivers further reduces the estimation error and the training overhead. Simulation results compare the three proposed techniques. The performance of the

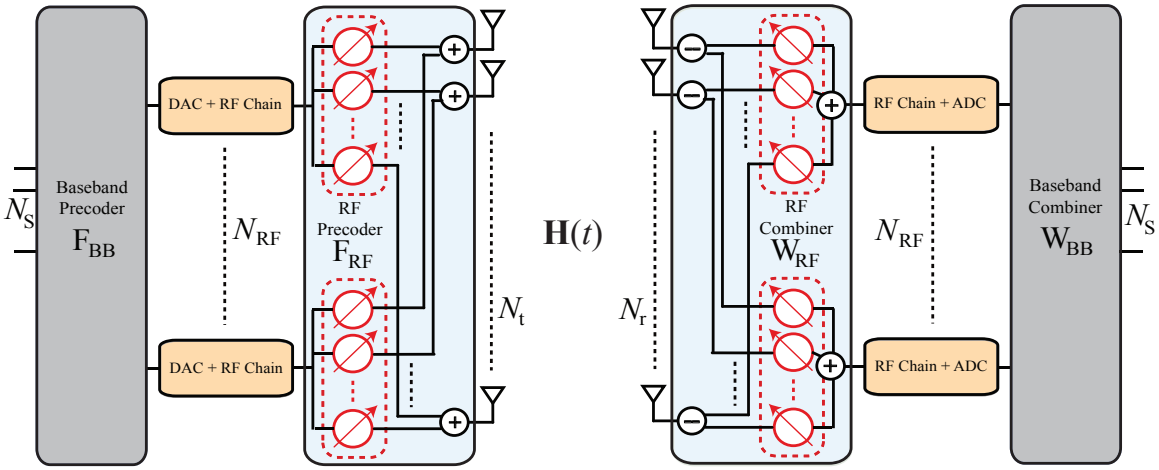

Figure 4.1: Figure illustrating the transmitter and receiver structure assumed for the hybrid precoding and combining in this chapter. The RF precoder and the combiner are assumed to be implemented using a network of fully connected phase shifters.

proposed techniques as system and channel parameters are varied are presented to identify which approach suits better for a given scenario.

4.3 System and Channel Models

In this section, we present the SC-FDE hybrid architecture based system model, followed by a description of the adopted wideband mmWave channel model. The time domain channel estimation algorithm proposed in Section 4.4 operates on this kind of SCE-FDE hybrid system, while the frequency domain approach described in Section 4.5 can be applied to OFDM-based hybrid MIMO systems as that in [80].

4.3.1 System Model

Consider a single-user mmWave MIMO system with a transmitter having N_{t} antennas and a receiver with N_{r} antennas. Both the transmitter and the receiver are assumed to have N_{RF} RF chains as shown in Fig. 4.1. The hybrid precoder and combiner used in the frequency selective mmWave system is generally of the form $\mathbf{F}^{\mathrm{fd}}[k] = \mathbf{F}_{\mathrm{RF}}\mathbf{F}_{\mathrm{BB}}^{\mathrm{fd}}[k] \in \mathbb{C}^{N_{\mathrm{t}} \times N_{\mathrm{s}}}$ and $\mathbf{W}^{\mathrm{fd}}[k] = \mathbf{W}_{\mathrm{RF}}\mathbf{W}_{\mathrm{BB}}^{\mathrm{fd}}[k] \in \mathbb{C}^{N_{\mathrm{r}} \times N_{\mathrm{s}}}$, respectively for the kth subcarrier [80]. In this chapter, we focus on the channel estimation having the training precoders/combiners done in the time domain, so we will use $\mathbf{F}$ and $\mathbf{W}$ (without k) to denote the time domain training precoders/combiners. Accordingly, the transmitter uses a hybrid precoder $\mathbf{F} = \mathbf{F}_{\mathrm{RF}}\mathbf{F}_{\mathrm{BB}} \in \mathbb{C}^{N_{\mathrm{t}} \times N_{\mathrm{s}}}$, N_{s} being the number of data streams that can be transmitted. Denoting the symbol vector at instance n as $\mathbf{s}[n] \in \mathbb{C}^{N_{\mathrm{s}} \times 1}$, satisfying $\mathbb{E}[\mathbf{s}[n]\mathbf{s}[n]^*] = \frac{1}{N_{\mathrm{s}}}\mathbf{I}$, the signal transmitted at discrete-time n is $\tilde{\mathbf{s}}[n] = \mathbf{F}\mathbf{s}[n]$.

The $N_{\mathrm{r}} \times N_{\mathrm{t}}$ channel matrix between the transmitter and the receiver is assumed to be frequency selective, having a delay tap length N_{c} and is denoted as $\mathbf{H}_d,\ d = 0,\ 1,\ ...,\ N_{\mathrm{c}} - 1$. With $\mathbf{v}[n] \sim \mathcal{N}(0, \sigma^2\mathbf{I})$ denoting the additive noise vector, the received signal can be written as

$$\mathbf{r}[n] = \sqrt{\rho} \sum_{d=0}^{N_{\mathrm{c}}-1} \mathbf{H}_d\mathbf{F}\mathbf{s}[n-d] + \mathbf{v}[n]. \tag{4.1}$$

The noise sample variance $\sigma^2 = N_{\mathrm{o}}B$, where B is the wideband system bandwidth, so that the received signal SNR $= \rho/\sigma^2$. The receiver applies a hybrid combiner $\mathbf{W} = \mathbf{W}_{\mathrm{RF}}\mathbf{W}_{\mathrm{BB}} \in \mathbb{C}^{N_{\mathrm{r}} \times N_{\mathrm{s}}}$, so that the post combining signal at the receiver is

$$\mathbf{y}[n] = \sqrt{\rho} \sum_{d=0}^{N_{\mathrm{c}}-1} \mathbf{W}^*\mathbf{H}_d\mathbf{F}\mathbf{s}[n-d] + \mathbf{W}^*\mathbf{v}[n]. \tag{4.2}$$

There are several RF precoder and combiner architectures that can be implemented [65]. In this chapter, we assume a fully connected phase shifting network [65]. We also consider the constraint so that only quantized angles in

$$\mathcal{A} = \left\{ 0,\ \frac{2\pi}{2^{N_{\mathrm{Q}}}},\ \cdots,\ \frac{\left(2^{N_{\mathrm{Q}}}-1\right)2\pi}{2^{N_{\mathrm{Q}}}} \right\} \tag{4.3}$$

can be realized in the phase shifters. Here N_{Q} is the number of angle quantization bits. This implies $[\mathbf{F}]_{i,j} = \frac{1}{\sqrt{N_{\mathrm{t}}}} e^{\mathrm{j}\varphi_{i,j}}$ and $[\mathbf{W}]_{i,j} = \frac{1}{\sqrt{N_{\mathrm{r}}}} e^{\mathrm{j}\omega_{i,j}}$, with $\varphi_{i,j},\ \omega_{i,j} \in \mathcal{A}$.

4.3.2 Channel Model

Consider a geometric channel model [64,79] for the frequency selective mmWave channel consisting of N_{p} paths[2]. The dth delay tap of the channel can be expressed as

$$\mathbf{H}_d = \sum_{\ell=1}^{N_{\mathrm{p}}} \alpha_\ell p(dT_{\mathrm{s}} - \tau_\ell)\mathbf{a}_{\mathrm{R}}(\phi_\ell)\mathbf{a}_{\mathrm{T}}^*(\theta_\ell), \qquad d = 0,\ 1,\ ...,\ N_{\mathrm{c}} - 1, \tag{4.4}$$

where $p(\tau)$ denotes the band-limited pulse shaping filter response evaluated at τ, $\alpha_\ell \in \mathbb{C}$ is the complex gain of the ℓth channel path, $\tau_\ell \in \mathbb{R}$ is the delay of the ℓth path, $\phi_\ell \in [0, 2\pi)$ and $\theta_\ell \in [0, 2\pi)$ are the angles of arrival and departure, respectively of the ℓth path, and $\mathbf{a}_{\mathrm{R}}(\phi_\ell) \in \mathbb{C}^{N_{\mathrm{r}} \times 1}$ and $\mathbf{a}_{\mathrm{T}}(\theta_\ell) \in \mathbb{C}^{N_{\mathrm{t}} \times 1}$ denote the antenna array response vectors of the receiver and transmitter, respectively. As an example, we use uniform linear antenna arrays, whose array response vectors are given in explicit

[2]Typical mmWave channels assume a clustered channel model made up of a few clusters N_{clusters} with $N_{\mathrm{rays},i}$ rays in the ith cluster. In this case, N_{p} paths physically corresponds to $\sum_i = 1^{N_{\mathrm{clusters}}} N_{\mathrm{rays},i}$. In the sparse formulation for the channel estimation problem, however, we say that N_{p} corresponds to the number of resolvable components of the frequency selective channel in terms of a suitably defined sparsifying dictionary.

form in Section 4.8. Note that, the effective baseband channel is seen through the RF front end (analog processing) and hence would include the filter response used for band limiting the signal in the receiver chain, as modeled in (4.4).

The transmitter and the receiver are assumed to know the array response vectors. The proposed estimation algorithm applies to any arbitrary antenna array configuration. The channel model in (4.4) can be written compactly as

$$\mathbf{H}_d = \mathbf{A}_{\mathrm{R}} \mathbf{\Delta}_d \mathbf{A}_{\mathrm{T}}^*, \tag{4.5}$$

where $\mathbf{\Delta}_d \in \mathbb{C}^{N_{\mathrm{p}} \times N_{\mathrm{p}}}$ is diagonal with non-zero entries $\alpha_\ell p(dT_{\mathrm{s}} - \tau_\ell)$, and $\mathbf{A}_{\mathrm{R}} \in \mathbb{C}^{N_{\mathrm{r}} \times N_{\mathrm{p}}}$ and $\mathbf{A}_{\mathrm{T}} \in \mathbb{C}^{N_{\mathrm{t}} \times N_{\mathrm{p}}}$ contain the columns $\mathbf{a}_{\mathrm{R}}(\phi_\ell)$ and $\mathbf{a}_{\mathrm{T}}(\theta_\ell)$, respectively. Under this notation, vectorizing the channel matrix in (4.5) gives

$$\mathrm{vec}(\mathbf{H}_d) = \left(\bar{\mathbf{A}}_{\mathrm{T}} \circ \mathbf{A}_{\mathrm{R}}\right) \begin{bmatrix} \alpha_1 p(dT_{\mathrm{s}} - \tau_1) \\ \alpha_2 p(dT_{\mathrm{s}} - \tau_2) \\ \vdots \\ \alpha_{N_{\mathrm{p}}} p(dT_{\mathrm{s}} - \tau_{N_{\mathrm{p}}}) \end{bmatrix}. \tag{4.6}$$

Note that the ℓth column of $\bar{\mathbf{A}}_{\mathrm{T}} \circ \mathbf{A}_{\mathrm{R}}$ is of the form $\bar{\mathbf{a}}_{\mathrm{T}}(\theta_\ell) \otimes \mathbf{a}_{\mathrm{R}}(\phi_\ell)$. We define the vectorized channel

$$\mathbf{h}_{\mathrm{c}} = \begin{bmatrix} \mathrm{vec}(\mathbf{H}_0) \\ \mathrm{vec}(\mathbf{H}_1) \\ \vdots \\ \mathrm{vec}(\mathbf{H}_{N_{\mathrm{c}}-1}) \end{bmatrix}, \tag{4.7}$$

which is the unknown signal that is estimated using the channel estimation algorithms proposed in the chapter. We assume that the average channel power $\mathbb{E}\left[\|\mathbf{h}_{\mathrm{c}}\|_2^2\right] = N_{\mathrm{r}} N_{\mathrm{t}}$ to facilitate comparison of the various channel estimation approaches proposed next.

4.4 Time-domain Channel Estimation via Compressed Sensing

In this section, we present our proposed time-domain explicit channel estimation algorithm that leverages the sparse representation of the wideband mmWave channel. The hardware constraints on the training frame structure and the precoding-combining beam patterns are also explained. We consider the channel estimation at a single receiver, with the transmitter sending training sequence during each channel coherence time. The same extends directly to training multiple receivers. Further, channel reciprocity may be assumed to estimate the reverse channels.

In the mmWave wearables' setting, typical values of coherence time, which is a function of the Doppler spread due to human users' mobility, is a few milliseconds [81–83]. Even in a highly mobile environment, a minimum coherence time of 32 ms was observed [83]. Given that any proposed channel training would have to get the channel estimates with reasonable error performance within a small time window in a channel coherence period, we set a rather tight limit of 1 ms to perform the channel training. This ensures that reasonably low-error channel estimates are obtained with low training overhead.

4.4.1 Sparse Formulation in the Time Domain

For the sparse formulation of the proposed time domain approach, consider block transmission of training frames, with a zero prefix (ZP) appended to each frame [76, 84]. The frame length is assumed to be N and the ZP length is set to $N_{\mathrm{c}} - 1$, with $N > N_{\mathrm{c}}$, the number of discrete time MIMO channel taps. A hybrid

architecture is assumed at the transmitter and the receiver as shown in Fig. 4.2. The use of block transmission with $N_{\rm c}-1$ zero padding is important here, since it allows reconfiguring the RF circuits from one frame to the other and avoids loss of training data during this reconfiguration. This also avoids inter frame interference. Also note that for symboling rate of 1760 MHZ (the chip rate used in IEEE 802.11ad preamble), it is impractical to use different precoders and combiners for different symbols. It is more feasible, however, to reconfigure the RF circuitry for different frames with $N \sim 16-512$ symbols. Further note that at this chip rate, sending 100 training preambles of length 512, for example, results in a total training period of roughly 0.03 ms. This corresponds to around 3 per cent overhead per channel coherence time for the channel training, assuming a pessimistic lower bound of 1 ms for the coherence time [83].

To formulate the sparse recovery problem, we assume that $N_{\rm RF}$ is the number of RF chains used at the transceivers. For the mth training frame, the transmitter uses an RF precoder $\mathbf{F}_m \in \mathbb{C}^{N_{\rm t}\times N_{\rm RF}}$, that can be realized using quantized angles at the analog phase shifters. Then, the nth symbol of the mth received frame is

$$\mathbf{r}_m[n] = \sum_{d=0}^{N_{\rm c}-1} \mathbf{H}_d \mathbf{F}_m \mathbf{s}_m[n-d] + \mathbf{v}_m[n], \tag{4.8}$$

where $\mathbf{s}_m[n] \in \mathbb{C}^{N_{\rm RF}\times 1}$ is the nth training data symbol of the mth training frame

$$\mathbf{s}_m = [\, \underbrace{0 \ \cdots \ 0}_{N_{\rm c}-1} \ \mathbf{s}_m[1] \ \cdots \ \mathbf{s}_m[N] \,]\,. \tag{4.9}$$

The training data sequence could be designed, for example, to facilitate synchronization as well similar to the complementary Golay sequences used in IEEE 802.11ad [11].

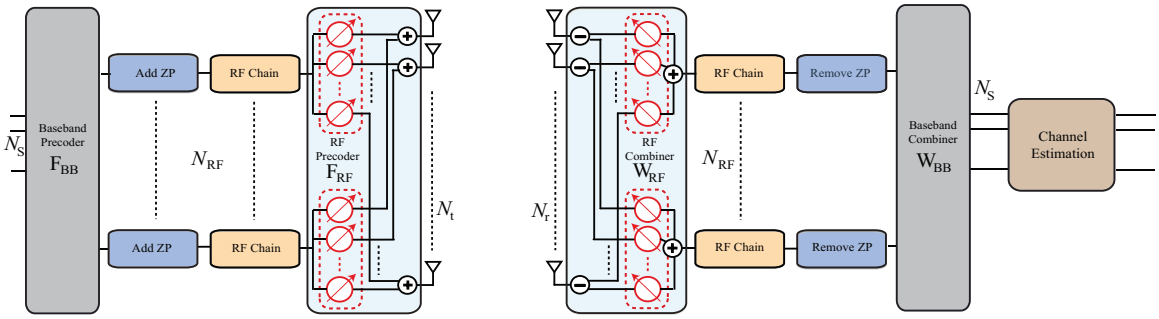

Figure 4.2: Figure illustrating the transceiver chains and the frame structure assumed for the time-domain channel estimation of the frequency selective mmWave system with N_{c} channel taps. Zero padding (ZP) of length at least $N_{\mathrm{c}}-1$ is prefixed to the training symbols of length N for RF chain reconfiguration across frames.

Note from (4.8) that due to multi-path fading the unknown parameters of the channel (contained within $\mathbf{H}_d,\ d=0,\ 1,\ \ldots,\ N_{\mathrm{c}}-1$) are all entangled, and potentially also suppressed, due to adding up non-coherently. The proposed training frame structure and the sparsifying dictionary that we propose in the sequel, still expose the channel to enable sparse recovery.

At the receiver, an RF combiner $\mathbf{W}_m \in \mathbb{C}^{N_{\mathrm{r}} \times N_{\mathrm{RF}}}$ realized using quantized angles at the analog phase shifters is used during the mth training phase. The post combining signal is

$$\begin{bmatrix} \mathbf{y}_m^{\mathrm{T}}[1] \\ \mathbf{y}_m^{\mathrm{T}}[2] \\ \vdots \\ \mathbf{y}_m^{\mathrm{T}}[N] \end{bmatrix}^{\mathrm{T}} = \mathbf{W}_m^{*}\big[\mathbf{H}_0 \ \cdots \ \mathbf{H}_{N_{\mathrm{c}}-1}\big](\mathbf{I}_{N_{\mathrm{c}}} \otimes \mathbf{F}_m)\,\mathbf{S}_m^{\mathrm{T}} + \mathbf{e}_m^{\mathrm{T}} \in \mathbb{C}^{1 \times N N_{\mathrm{RF}}}, \tag{4.10}$$

where

$$\mathbf{S}_m = \begin{bmatrix} \mathbf{s}_m^{\mathrm{T}}[1] & 0 & \cdots & 0 \\ \mathbf{s}_m^{\mathrm{T}}[2] & \mathbf{s}_m^{\mathrm{T}}[1] & \cdots & . \\ \vdots & \vdots & \ddots & \vdots \\ \mathbf{s}_m^{\mathrm{T}}[N] & \cdots & \cdots & \mathbf{s}_m^{\mathrm{T}}[N-N_{\mathrm{c}}+1] \end{bmatrix}, \tag{4.11}$$

is of dimension $N \times N_{\mathrm{c}} N_{\mathrm{RF}}$, and

$$\mathbb{E}\left[\mathbf{e}_m \mathbf{e}_m^*\right] = \sigma^2 \mathbf{I}_N \otimes \mathbf{W}_m^* \mathbf{W}_m. \tag{4.12}$$

Using the matrix equality $\mathrm{vec}\left(\mathbf{ABC}\right) = \left(\mathbf{C}^{\mathrm{T}} \otimes \mathbf{A}\right) \mathrm{vec}\left(\mathbf{B}\right)$ and the notation for the vectorized channel in (4.7), vectorizing (4.10) gives

$$\mathbf{y}_m = \begin{bmatrix} \mathbf{y}_m[1] \\ \mathbf{y}_m[2] \\ \vdots \\ \mathbf{y}_m[N] \end{bmatrix} = \underbrace{\mathbf{S}_m \left(\mathbf{I}_{N_{\mathrm{c}}} \otimes \mathbf{F}_m^{\mathrm{T}}\right) \otimes \mathbf{W}_m^*}_{\mathbf{\Phi}_{\mathrm{td}}^{(m)}} \mathbf{h}_{\mathrm{c}} + \mathbf{e}_m. \tag{4.13}$$

Using the form in (4.6) and denoting $\gamma_{\ell,d} = \alpha_\ell p(dT_{\mathrm{s}} - \tau_\ell)$, (4.13) can be expressed as

$$\mathbf{y}_m = \mathbf{\Phi}_{\mathrm{td}}^{(m)} \left(\mathbf{I}_{N_{\mathrm{c}}} \otimes \bar{\mathbf{A}}_{\mathrm{T}} \circ \mathbf{A}_{\mathrm{R}}\right) \begin{bmatrix} \gamma_{1,0} \\ \vdots \\ \gamma_{N_{\mathrm{p}},0} \\ \vdots \\ \gamma_{1,(N_{\mathrm{c}}-1)} \\ \vdots \\ \gamma_{N_{\mathrm{p}},(N_{\mathrm{c}}-1)} \end{bmatrix} + \mathbf{e}_m. \tag{4.14}$$

In (4.14), the matrices $\mathbf{A}_{\mathrm{T}}$ and $\mathbf{A}_{\mathrm{R}}$ and the complex gains $\{\alpha_i\}$ and delays $\{\tau_i\}$ contained within $\gamma_{\ell,d}$ are all unknowns that need to be estimated to get the explicit multi tap MIMO channel. Accordingly, we first recover the AoAs / AoDs by estimating the columns of $\bar{\mathbf{A}}_{\mathrm{T}} \circ \mathbf{A}_{\mathrm{R}}$ via sparse recovery.

To formulate the compressed sensing problem in the time domain, we first exploit the sparse nature of the channel in the angular domain. Accordingly, we define the matrices $\mathbf{A}_{\mathrm{tx}}$ and $\mathbf{A}_{\mathrm{rx}}$ used for sparse recovery, that can be computed apriori at the receiver. The $N_{\mathrm{t}} \times G_{\mathtt{t}}$ matrix $\mathbf{A}_{\mathrm{tx}}$ consists of columns $\mathbf{a}_{\mathrm{T}}(\tilde{\theta_x})$, with $\tilde{\theta_x}$ drawn from a quantized angle grid of size $G_{\mathtt{t}}$, and the $N_{\mathrm{r}} \times G_{\mathtt{r}}$ matrix $\mathbf{A}_{\mathrm{rx}}$ consists

of columns $\mathbf{a}_{\mathrm{R}}(\tilde{\phi}_x)$, with $\tilde{\phi}_x$ drawn from a quantized angle grid of size G_{r}. Neglecting the grid quantization error, we can then express (4.13) as

$$\mathbf{y}_m = \mathbf{\Phi}_{\mathrm{td}}^{(m)} \left(\mathbf{I}_{N_{\mathrm{c}}} \otimes \bar{\mathbf{A}}_{\mathrm{tx}} \otimes \mathbf{A}_{\mathrm{rx}}\right) \hat{\mathbf{x}}_{\mathrm{td}} + \mathbf{e}_m. \tag{4.15}$$

Note that the actual frequency selective mmWave channel as seen at the baseband has angles of arrival and departure drawn from $[0, 2\pi)$. The quantization used for constructing the dictionary, when fine enough, can ensure that the dominant AoAs and AoDs are captured as columns of $\bar{\mathbf{A}}_{\mathrm{tx}} \otimes \mathbf{A}_{\mathrm{rx}}$. The error incurred due to the angle grid quantization is investigated in Section 4.8, where we assume off grid values for the AoA/AoD in the simulations. With this, the signal $\hat{\mathbf{x}}_{\mathrm{td}}$ consisting of the time domain channel gains and pulse shaping filter response is more sparse than the unknown vector in (4.14), and is of size $N_{\mathrm{c}} G_{\mathsf{r}} G_{\mathsf{t}} \times 1$.

Next, the band-limited nature of the sampled pulse shaping filter is used to operate with an unknown channel vector with a lower sparsity level. For that, we look at the sampled version of the pulse-shaping filter $\mathbf{p}_d$ having entries $p_d(n) = p_{\mathrm{rc}}\left((d - n\frac{N_{\mathrm{c}}}{G_{\mathrm{c}}})T_{\mathrm{s}}\right)$, for $d = 1, 2, \cdots, N_{\mathrm{c}}$ and $n = 1, 2, \cdots, G_{\mathrm{c}}$. Then, neglecting the quantization error due to sampling in the delay domain, we can write (4.15) as

$$\mathbf{y}_m = \mathbf{\Phi}_{\mathrm{td}}^{(m)} \left(\mathbf{I}_{N_{\mathrm{c}}} \otimes \bar{\mathbf{A}}_{\mathrm{tx}} \otimes \mathbf{A}_{\mathrm{rx}}\right) \mathbf{\Gamma} \mathbf{x}_{\mathrm{td}} + \mathbf{e}_m, \tag{4.16}$$

$$\text{where} \qquad \mathbf{\Gamma} = \begin{bmatrix} \mathbf{I}_{G_{\mathrm{r}}G_{\mathrm{t}}} \otimes \mathbf{p}_1^{\mathrm{T}} \\ \mathbf{I}_{G_{\mathrm{r}}G_{\mathrm{t}}} \otimes \mathbf{p}_2^{\mathrm{T}} \\ \vdots \\ \mathbf{I}_{G_{\mathrm{r}}G_{\mathrm{t}}} \otimes \mathbf{p}_{N_{\mathrm{c}}}^{\mathrm{T}} \end{bmatrix}, \tag{4.17}$$

and $\mathbf{x}_{\mathrm{td}} \in \mathbb{C}^{G_{\mathrm{c}} G_{\mathrm{r}} G_{\mathrm{t}} \times 1}$ is the N_{p}-sparse vector containing the time domain complex

channel gains[3].

Stacking M such measurements obtained from sending M training frames and using a different RF precoder and combiner for each frame, we have

$$\mathbf{y}_{\mathrm{td}} = \mathbf{\Phi}_{\mathrm{td}}\mathbf{\Psi}_{\mathrm{td}}\mathbf{x}_{\mathrm{td}} + \mathbf{e}, \tag{4.18}$$

$$\text{where } \mathbf{y}_{\mathrm{td}} = \begin{bmatrix} \mathbf{y}_1 \\ \mathbf{y}_2 \\ \vdots \\ \mathbf{y}_M \end{bmatrix} \in \mathbb{C}^{NMN_{\mathrm{RF}} \times 1} \tag{4.19}$$

is the measured time domain signal,

$$\mathbb{E}\left[\mathbf{e}\mathbf{e}^*\right] = \sigma^2 \mathrm{diag}\left(\mathbf{I}_N \otimes \mathbf{W}_1^*\mathbf{W}_1, \cdots, \mathbf{I}_N \otimes \mathbf{W}_M^*\mathbf{W}_M\right), \tag{4.20}$$

$$\mathbf{\Phi}_{\mathrm{td}} = \begin{bmatrix} \mathbf{S}_1\left(\mathbf{I}_{N_{\mathrm{c}}} \otimes \mathbf{F}_1^{\mathrm{T}}\right) \otimes \mathbf{W}_1^* \\ \mathbf{S}_2\left(\mathbf{I}_{N_{\mathrm{c}}} \otimes \mathbf{F}_2^{\mathrm{T}}\right) \otimes \mathbf{W}_2^* \\ \vdots \\ \mathbf{S}_M\left(\mathbf{I}_{N_{\mathrm{c}}} \otimes \mathbf{F}_m^{\mathrm{T}}\right) \otimes \mathbf{W}_m^* \end{bmatrix} \in \mathbb{C}^{NMN_{\mathrm{RF}} \times N_{\mathrm{c}}N_{\mathrm{r}}N_{\mathrm{t}}} \tag{4.21}$$

is the time domain measurement matrix, and

$$\begin{aligned} \mathbf{\Psi}_{\mathrm{td}} &= \left(\mathbf{I}_{N_{\mathrm{c}}} \otimes \ \bar{\mathbf{A}}_{\mathrm{tx}} \otimes \mathbf{A}_{\mathrm{rx}}\right)\mathbf{\Gamma} \\ &= \begin{bmatrix} \left(\bar{\mathbf{A}}_{\mathrm{tx}} \otimes \mathbf{A}_{\mathrm{rx}}\right) \otimes \mathbf{p}_1^{\mathrm{T}} \\ \left(\bar{\mathbf{A}}_{\mathrm{tx}} \otimes \mathbf{A}_{\mathrm{rx}}\right) \otimes \mathbf{p}_2^{\mathrm{T}} \\ \vdots \\ \left(\bar{\mathbf{A}}_{\mathrm{tx}} \otimes \mathbf{A}_{\mathrm{rx}}\right) \otimes \mathbf{p}_{N_{\mathrm{c}}}^{\mathrm{T}} \end{bmatrix} \in \mathbb{C}^{N_{\mathrm{c}}N_{\mathrm{r}}N_{\mathrm{t}} \times G_{\mathrm{c}}G_{\mathrm{r}}G_{\mathrm{t}}} \end{aligned} \tag{4.22}$$

is the dictionary in the time domain. The beamforming and combining vectors $\mathbf{F}_m,\ \mathbf{W}_m, m = 1,\ 2,\ \cdots,\ M$ used for training have the phase angles chosen uniformly at random from the set $\mathcal{A}$ in (4.3).

[3]In this context, N_{p} denotes the number of resolvable components of the frequency selective channel in terms of the time-domain dictionary.

4.4.2 AoA/AoD and Channel Gain Estimation in the Time Domain

With the sparse formulation of the mmWave channel estimation problem in (4.18), compressed sensing tools can be first used to estimate the AoA and AoD. The support of $\mathbf{x}_{\text{td}}$ corresponds to a particular AoA, AoD and path delay, and hence estimating the support of $\mathbf{x}_{\text{td}}$ amounts to estimating a channel path, and the corresponding non-zero value corresponds to the path gain. Note that we can increase or decrease the angle quantization grid sizes G_{r} and G_{t}, and the delay domain quantization grid size G_{c}, used for constructing the time domain dictionary to minimize the quantization error. As the sensing matrix is known at the receiver, sparse recovery algorithms can be used to estimate the AoA and AoD.

To estimate the support of the sparse vector $\mathbf{x}_{\text{td}}$, we solve the optimization problem

$$\min_{\mathbf{x}_{\text{td}}} \|\mathbf{x}_{\text{td}}\|_1 \quad \text{such that} \quad \|\mathbf{y}_{\text{td}} - \mathbf{\Phi}_{\text{td}}\mathbf{\Psi}_{\text{td}}\mathbf{x}_{\text{td}}\|_2 \leq \epsilon. \tag{4.23}$$

We consider Orthogonal Matching Pursuit (OMP) for solving (4.23), as used previously in [66,85]. There are several stopping criteria for OMP that can be used to solve (4.23). When the sparsity level N_{p} is known apriori, reaching that level could be used to stop the algorithm. When such information cannot be guessed before hand (which itself is an estimation problem), the residual error falling below a certain threshold is often used to terminate the recursive OMP algorithm. Accordingly, in the presence of noise, a suitable choice for the threshold ϵ is the noise variance. Hence, we assume the noise power as the stopping threshold, i.e., $\epsilon = \mathbb{E}[\mathbf{e}^*\mathbf{e}]$.

It is important to note that the performance of OMP algorithm depends on

the properties of sensing matrix, such as mutual coherence and restricted isometry property. In this context, IID Guassian random sensing matrices is beneficial [77]. In a hybrid mmWave system, however, generating IID random sensing matrices is infeasible due to the hardware limitations of the RF precoders and combiners. Considering various hybrid architectures, [86] analyzed the mutual coherence of the sensing matrix for a narrow band sparse formulation. Due to the complicated structure of the sensing matrix, however, only a few special cases are considered in [86]. The wideband sparse formulation does not simplify things any further. Therefore, to understand the performance of the OMP algorithm, we resort to simulations later on.

Instead of OMP, orthogonal least squares (OLS) could also be used for the sparse recovery especially since the sensing matrix does not have orthogonal columns. The performance of OLS is better than OMP when the sparsity level is known [87,88]. We, however, use OMP since it is less computationally complex compared to OLS [88] and since the sparsity level is not assumed to be known apriori. It is shown later using simulations that the low recovery error performance provided by OMP is sufficient to achieve the maximum spectral efficiency using the precoders and combiners designed from the channel estimates.

Following the support estimation via sparse recovery, the channel gains can be estimated. While there are many ways to estimate the gains, even directly from OMP, we only give the details for one approach next – using least squares. The various methods are based on plugging in the columns of the dictionary matrices corresponding to the estimated AoA and AoD. That is, let $\mathcal{S}_{\mathsf{A}}^{\text{td}}$ and $\mathcal{S}_{\mathsf{D}}^{\text{td}}$, respectively be the estimated AoA and AoD using sparse recovery in the proposed time domain

formulation. Then, using (4.15) and stacking the M measurements, we have

$$\mathbf{y}_{\mathrm{td}} = \underbrace{\mathbf{\Phi}_{\mathrm{td}} \left(\mathbf{I}_{N_{\mathrm{c}}} \otimes \left[\bar{\mathbf{A}}_{\mathrm{tx}} \right]_{:, \mathcal{S}_{\mathsf{D}}^{\mathrm{td}}} \otimes \left[\mathbf{A}_{\mathrm{rx}} \right]_{:, \mathcal{S}_{\mathsf{A}}^{\mathrm{td}}} \right)}_{\mathbf{\Omega}_{\mathrm{td}}} \hat{\mathbf{x}}_{\mathrm{td}} + \mathbf{e}, \tag{4.24}$$

so that the channel coefficients via least squares is

$$\hat{\mathbf{x}}_{\mathrm{td}}^{\mathrm{LS}} = \left(\mathbf{\Omega}_{\mathrm{td}}^{*} \mathbf{\Omega}_{\mathrm{td}} \right)^{-1} \mathbf{\Omega}_{\mathrm{td}}^{*} \mathbf{y}_{\mathrm{td}}. \tag{4.25}$$

4.5 Frequency-domain Channel Estimation via Compressed Sensing

In this section, we explain how the compressed sensing problem can be formulated in the frequency domain. The additional modifications needed in the system model, and the corresponding advantages and disadvantages are also explained in this section.

Using the geometric channel model in (4.4), the complex channel matrix in the frequency domain can be written as

$$\begin{aligned} \boldsymbol{H}[k] &= \sum_{d=0}^{N_{\mathrm{c}}-1} \mathbf{H}_d e^{-\mathrm{j}\frac{2\pi k d}{K}} \\ &= \sum_{\ell=1}^{N_{\mathrm{p}}} \alpha_\ell \mathbf{a}_{\mathrm{R}}(\phi_\ell) \mathbf{a}_{\mathrm{T}}^{*}(\theta_\ell) \sum_{d=0}^{N_{\mathrm{c}}-1} p(dT_{\mathrm{s}} - \tau_\ell) e^{-\mathrm{j}\frac{2\pi k d}{K}}. \end{aligned} \tag{4.26}$$

Defining $\beta_{k,\ell} = \sum_{d=0}^{N_{\mathrm{c}}-1} p(dT_{\mathrm{s}} - \tau_\ell) e^{-\mathrm{j}\frac{2\pi k d}{K}}$ a compact expression can be derived

$$\boldsymbol{H}[k] = \sum_{\ell=1}^{N_{\mathrm{p}}} \alpha_\ell \beta_{k,\ell} \mathbf{a}_{\mathrm{R}}(\phi_\ell) \mathbf{a}_{\mathrm{T}}^{*}(\theta_\ell). \tag{4.27}$$

Vectorizing (4.27) gives the unknown signal that is estimated using the frequency domain estimation algorithm,

$$\mathrm{vec}\left(\boldsymbol{H}[k]\right) = \left(\bar{\mathbf{A}}_{\mathrm{T}} \circ \mathbf{A}_{\mathrm{R}}\right) \begin{bmatrix} \alpha_1\beta_{k,1} \\ \alpha_2\beta_{k,2} \\ \vdots \\ \alpha_{N_{\mathrm{p}}}\beta_{k,N_{\mathrm{p}}} \end{bmatrix}. \tag{4.28}$$

Note that the vector channel representation of the kth subcarrier in (4.28), is similar to the time domain vector representation in (4.6). The key difference, however, is that, unlike the time domain approach, each of the unknown vectors corresponding to the K subcarriers can be estimated separately, in parallel as explained next.

4.5.1 Sparse Formulation in the Frequency Domain

For the sparse formulation in the proposed frequency domain approach, appropriate signal processing is performed to convert the linear convolution occurring during the frame transmission in the system to a circular convolution in the time domain. We would like to remind the readers that we propose ZP instead of CP for the training frames to facilitate reconfiguration of the RF precoders and combiners from frame to frame. With ZP assumed in the frame structure of the training preamble, the overlapping and sum [89] method is used, followed by the K-point FFT to formulate the frequency-domain sparse channel estimation problem per subcarrier $k = 1, 2, \cdots, K$. The overlap and add method essentially involves adding the last $N_{\mathrm{c}} - 1$ samples to first $N_{\mathrm{c}} - 1$ samples as shown in Fig. 4.3. Fig. 4.3 also illustrates the proposed system model in the time-domain with the hybrid architecture and signal processing components required for the frequency domain channel estimation in

an SC-FDE system with ZP. Alternatively, for an OFDM based system, the digital processing may be implemented in the frequency domain after the FFT operation. The advantage of the proposed frequency domain approach is that different baseband precoders and combiners can be used for different subcarriers [80] in the frequency domain, while the RF processing is frequency flat. The proposed frequency domain approach, therefore, works for both SC-FDE and OFDM systems, where the received signal is processed per-subcarrier. We next look into the received signal in the kth subcarrier.

With $\mathbf{F}_m$ denoting the RF precoder used at the transmitter for the transmission of the mth training frame/OFDM symbol, and $\mathbf{W}_m$, the corresponding RF combiner, the post combining signal in the kth subcarrier can be written as

$$\breve{\boldsymbol{y}}_m[k] = \mathbf{W}_m^* \boldsymbol{H}[k] \mathbf{F}_m \breve{\boldsymbol{s}}_m[k] + \breve{\boldsymbol{e}}_m[k], \tag{4.29}$$

$$\text{where} \quad \breve{\boldsymbol{s}}_m[k] = \sum_{n=1}^{N} \mathbf{s}_m[n] e^{-\mathrm{j}\frac{2\pi kn}{K}} \tag{4.30}$$

is the kth coefficient of the K-point FFT of $m$the time domain transmit frame. The covariance of the frequency domain noise vector in (4.29) is $\mathbb{E}\left[\breve{\boldsymbol{e}}_m[k]\breve{\boldsymbol{e}}_m^*[k]\right] = \sigma^2 \mathbf{W}_m^* \mathbf{W}_m$, and $\sigma^2 = N_{\mathrm{o}} B$. The frequency flat RF combiners and precoders are assumed to be realized with a network of phase shifters with phase angles drawn from a finite set, as before. Vectorizing (4.29), and substituting (4.28) gives

$$\mathrm{vec}\left(\breve{\boldsymbol{y}}_m[k]\right) = \underbrace{\left(\breve{\boldsymbol{s}}_m^{\mathrm{T}}[k] \mathbf{F}_m^{\mathrm{T}} \otimes \mathbf{W}_m^*\right)}_{\boldsymbol{\Phi}_{\mathrm{fd}}^{(m)}[k]} \mathrm{vec}\left(\boldsymbol{H}[k]\right) + \breve{\boldsymbol{e}}_m[k]. \tag{4.31}$$

Assuming the AoAs and AoDs are drawn from a grid of size G_{r} and G_{t}, respectively, and neglecting the quantization error, we can write (4.31) in terms of the dictionary

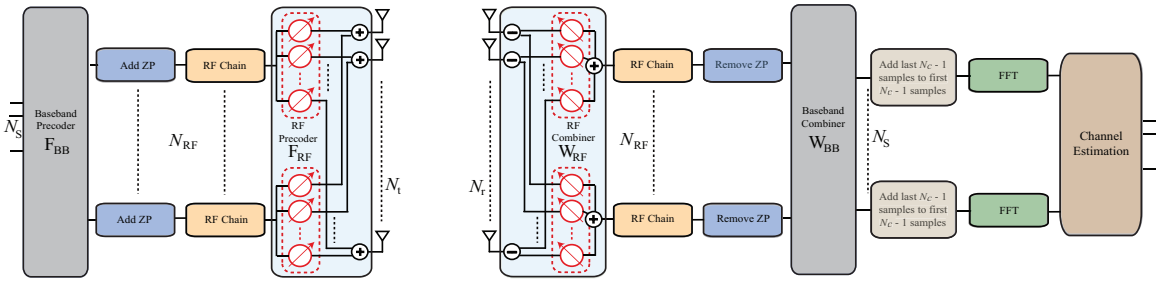

Figure 4.3: Figure illustrating the transceiver chains and the frame structure assumed for the frequency-domain channel estimation of the frequency selective mmWave system with N_{c} channel taps. Zero padding (ZP) of length $N_{\mathrm{c}}-1$ is prefixed to the training symbols of length N for RF chain reconfiguration across frames.

matrices defined in Section 4.4 as follows:

$$\mathrm{vec}\left(\breve{\boldsymbol{y}}_m[k]\right) = \boldsymbol{\Phi}_{\mathrm{fd}}^{(m)}[k]\left(\bar{\mathbf{A}}_{\mathrm{tx}} \otimes \mathbf{A}_{\mathrm{rx}}\right)\breve{\boldsymbol{x}}[k] + \breve{\boldsymbol{e}}_m[k], \tag{4.32}$$

with the signal $\breve{\boldsymbol{x}}[k] \in \mathbb{C}^{G_{\mathrm{r}}G_{\mathrm{t}}\times 1}$ being N_{p}-sparse. Stacking M such measurements obtained over the course of M training frame transmission, each with a different pair of RF precoder and combiner, we have the following sparse formulation for the kth subcarrier

$$\breve{\boldsymbol{y}}[k] = \boldsymbol{\Phi}_{\mathrm{fd}}[k]\boldsymbol{\Psi}_{\mathrm{fd}}\breve{\boldsymbol{x}}[k] + \breve{\boldsymbol{e}}[k], \tag{4.33}$$

in terms of the frequency domain dictionary $\boldsymbol{\Psi}_{\mathrm{fd}} = \left(\bar{\mathbf{A}}_{\mathrm{tx}} \otimes \mathbf{A}_{\mathrm{rx}}\right) \in \mathbb{C}^{N_{\mathrm{r}}N_{\mathrm{t}}\times G_{\mathrm{r}}G_{\mathrm{t}}}$ and the measurement matrix in the frequency domain

$$\boldsymbol{\Phi}_{\mathrm{fd}}[k] = \begin{bmatrix} \breve{\boldsymbol{s}}_1^{\mathrm{T}}[k]\mathbf{F}_1^{\mathrm{T}} \otimes \mathbf{W}_1^* \\ \breve{\boldsymbol{s}}_2^{\mathrm{T}}[k]\mathbf{F}_2^{\mathrm{T}} \otimes \mathbf{W}_2^* \\ \vdots \\ \breve{\boldsymbol{s}}_M^{\mathrm{T}}[k]\mathbf{F}_M^{\mathrm{T}} \otimes \mathbf{W}_M^* \end{bmatrix} \in \mathbb{C}^{MN_{\mathrm{RF}}\times N_{\mathrm{r}}N_{\mathrm{t}}}. \tag{4.34}$$

The covariance of the noise in (4.33) is

$$\mathbb{E}\left[\breve{\boldsymbol{e}}[k]\breve{\boldsymbol{e}}^*[k]\right] = \sigma^2 \mathrm{diag}\left(\mathbf{W}_1^*\mathbf{W}_1, \mathbf{W}_2^*\mathbf{W}_2, \cdots, \mathbf{W}_M^*\mathbf{W}_M\right). \tag{4.35}$$

4.5.2 AoA/AoD and Channel Gain Estimation per Subcarrier

As discussed previously in Section 4.4.2, we first estimate the support of $\breve{\boldsymbol{x}}[k]$, that corresponds to a particular AoA and AoD, and then proceed to estimate the MIMO channel coefficients of the kth subcarrier, which correspond to the non-zero values of $\breve{\boldsymbol{x}}[k]$. As with the time domain approach, we solve the following optimization problem

$$\min_{\breve{\boldsymbol{x}}[k]} \|\breve{\boldsymbol{x}}[k]\|_1 \quad \text{such that} \quad \|\breve{\boldsymbol{y}}[k] - \boldsymbol{\Phi}_{\text{fd}}[k]\boldsymbol{\Psi}_{\text{fd}}\breve{\boldsymbol{x}}[k]\|_2 \leq \epsilon. \tag{4.36}$$

via OMP with the stopping threshold $\epsilon = \mathbb{E}[\breve{\boldsymbol{e}}[k]^*\breve{\boldsymbol{e}}[k]]$, to estimate the support of the sparse vector $\breve{\boldsymbol{y}}[k]$, and hence the dominant angles of arrival and departure. The set of estimated AoAs is denoted as $\mathcal{S}_{\mathsf{A}}^{\text{fd}}$, and the set of AoDs is denoted as $\mathcal{S}_{\mathsf{D}}^{\text{fd}}$. These sets correspond to specific columns of the frequency domain dictionary Ψ_{fd}. Using $\mathcal{S}_{\mathsf{A}}^{\text{fd}}$ and $\mathcal{S}_{\mathsf{D}}^{\text{fd}}$, the channel coefficients, that correspond to the non-zero values of the sparse vector $\breve{\boldsymbol{x}}[k]$, can be derived as follows. From (4.33), after the sparse angle recovery

$$\breve{\boldsymbol{y}}[k] = \underbrace{\boldsymbol{\Phi}_{\text{fd}}[k]\left(\left[\bar{\mathbf{A}}_{\text{tx}}\right]_{:,\mathcal{S}_{\mathsf{D}}^{\text{fd}}} \otimes \left[\mathbf{A}_{\text{rx}}\right]_{:,\mathcal{S}_{\mathsf{A}}^{\text{fd}}}\right)}_{\boldsymbol{\Omega}_{\text{fd}}}\breve{\boldsymbol{x}}[k] + \breve{\boldsymbol{e}}[k], \tag{4.37}$$

so that, using least square estimation,

$$\breve{\boldsymbol{x}}^{\text{LS}}[k] = \left(\boldsymbol{\Omega}_{\text{fd}}^*\boldsymbol{\Omega}_{\text{fd}}\right)^{-1}\boldsymbol{\Omega}_{\text{fd}}^*\breve{\mathbf{y}}[\mathbf{k}]. \tag{4.38}$$

Note that using the sparse formulation in (4.33), the AoAs/AoDs and the channel coefficients of the the kth subcarrier can be estimated. Repeating the same for all the K subcarriers fully characterizes the frequency selective mmWave channel. While the dimensions of the matrices involved in the frequency-domain compressed

sensing problem is smaller in comparison to the time-domain formulation in Section 4.4, the channel estimation should be invoked K times to fully recover the channel coefficients. Further, additional pre-processing and FFT operation are required.

4.6 Combined Time-Frequency Compressive Channel Estimation

In this section, we formulate a technique via compressed sensing for explicit channel estimation, jointly in time and frequency. The key idea is to estimate the angles of arrival and departure via compressed sensing in the frequency domain, and then use the estimates to evaluate the channel gains and path delays in the time domain to obtain the entire channel.

The transmitter chain for the proposed combined time-frequency compressive channel estimation approach is the same as in Fig. 4.2 and Fig. 4.3. The system model for the receiver chain in Fig. 4.3, can be employed to perform sparse support recovery of the angles in the frequency domain for the proposed estimation approach in this section. Following the compressive support estimation, the pre-computed dictionary matrices in the time domain, and the measurement matrices can be used to estimate the channel coefficients of the frequency selective mmWave MIMO channel, as explained momentarily.

From (4.31) and (4.28), we can express the frequency domain received signal in the kth subcarrier, in terms of the actual AoAs and AoDs in the vector form as

follows

$$\mathrm{vec}\left(\breve{\boldsymbol{y}}_m[k]\right) = \boldsymbol{\Phi}_{\mathrm{fd}}^{(m)}[k]\left(\bar{\mathbf{A}}_{\mathrm{T}} \circ \mathbf{A}_{\mathrm{R}}\right) \begin{bmatrix} \alpha_1\beta_{k,1} \\ \alpha_2\beta_{k,2} \\ \vdots \\ \alpha_{N_{\mathrm{p}}}\beta_{k,N_{\mathrm{p}}} \end{bmatrix} + \breve{\boldsymbol{e}}_m[k], \tag{4.39}$$

with the noise covariance $\mathbb{E}\left[\breve{\boldsymbol{e}}_m[k]\breve{\boldsymbol{e}}_m^*[k]\right] = \sigma^2\mathbf{W}_m^*\mathbf{W}_m$.

AoA/AoD Estimation in Frequency Domain and Channel Gain Estimation in Time Domain: Note from (4.39), the AoA and AoD information in each subcarrier k is the same, and contained in $\bar{\mathbf{A}}_{\mathrm{T}} \circ \mathbf{A}_{\mathrm{R}}$, whose ℓth column is of the form $\bar{\mathbf{a}}_{\mathrm{T}}(\theta_\ell) \otimes \mathbf{a}_{\mathrm{R}}(\phi_\ell)$. Therefore, using sparse recovery in $1 \leq P \leq K$ number of subcarriers parallely, and concatenating the estimated angles, we can get a support set of the AoAs, denoted as $\mathcal{S}_{\mathsf{A}}$ and a set of AoD estimates denoted as $\mathcal{S}_{\mathsf{D}}$. One option to estimate the support is to use OMP as explained in Section 4.5.2, for P subcarriers in parallel. Since several angles might be estimated incorrectly due to sparse recovery under the influence of noise, using P parallel OMPs may not necessarily enhance performance. This is because we retain all the (potentially faulty) angle estimates on the P subcarrier, via concatenation. Prior work in [77, 90, 91] have studied methods to estimate a common support set from multiple parallel measurements. Such techniques may also be employed to recover the support set containing the AoA/AoD information in the frequency domain, both here as well as in the proposed approach in Section 4.5.

Following the support recovery in the frequency domain, to recover the entire channel, we switch to the time domain formulation in (4.15), (4.19), (4.21) and (4.22), but restrict to the set $\mathcal{S} = \{\mathcal{S}_{\mathsf{A}}, \mathcal{S}_{\mathsf{D}}\}$. Accordingly, we can write the effective time-

domain equation, conditioned on the estimated support set $\mathcal{S}$ as

$$\mathbf{y}_{\text{td}} = \underbrace{\mathbf{\Phi}_{\text{td}} \left[\mathbf{\Psi}_{\text{td}}\right]_{:,\mathcal{S}}}_{\mathbf{\Omega}} \mathbf{x}_{\text{td}} + \mathbf{e}, \tag{4.40}$$

where $\mathbf{\Phi}_{\text{td}}$ is that in (4.21), the noise covariance of $\mathbf{e}$ is that in (4.20), and

$$\left[\mathbf{\Psi}_{\text{td}}\right]_{:,\mathcal{S}} = \begin{bmatrix} \left[\bar{\mathbf{A}}_{\text{tx}}\right]_{:,\mathcal{S}_{\text{D}}} \otimes \left[\mathbf{A}_{\text{rx}}\right]_{:,\mathcal{S}_{\text{A}}} \otimes \tilde{\mathbf{p}}_1^T \\ \left[\bar{\mathbf{A}}_{\text{tx}}\right]_{:,\mathcal{S}_{\text{D}}} \otimes \left[\mathbf{A}_{\text{rx}}\right]_{:,\mathcal{S}_{\text{A}}} \otimes \tilde{\mathbf{p}}_2^T \\ \vdots \\ \left[\bar{\mathbf{A}}_{\text{tx}}\right]_{:,\mathcal{S}_{\text{D}}} \otimes \left[\mathbf{A}_{\text{rx}}\right]_{:,\mathcal{S}_{\text{A}}} \otimes \tilde{\mathbf{p}}_{N_{\text{c}}}^T \end{bmatrix} \in \mathbb{C}^{N_{\text{c}} N_{\text{r}} N_{\text{t}} \times G_{\text{c}} |\mathcal{S}|} \tag{4.41}$$

is the dictionary matrix conditioned on the knowledge of the support set. The unknown $\mathbf{x}_{\text{td}}$ in (4.40), contains channel coefficients in the time domain, which can now be obtained via least squares or MMSE to recover the entire MIMO channel matrices corresponding to all the delay taps. That is, from (4.40)

$$\mathbf{x}_{\text{td}}^{\text{LS}} = \left(\mathbf{\Omega}^* \mathbf{\Omega}\right)^{-1} \mathbf{\Omega}^* \mathbf{y}_{\text{td}}. \tag{4.42}$$

The advantage of using the combined time-frequency approach for the wideband channel estimation is twofold. First, since the sparse recovery is done in the frequency domain, the sizes of the measurement matrix and the dictionary are $MN_{\text{RF}} \times N_{\text{r}} N_{\text{t}}$ and $N_{\text{r}} N_{\text{t}} \times G_{\text{r}} G_{\text{t}}$, respectively, that are much smaller than the corresponding time domain matrices $\mathbf{\Phi}_{\text{td}}$ and $\mathbf{\Psi}_{\text{td}}$. Secondly, unlike the frequency domain approach, the channel estimates need not be separately evaluated per subcarrier, but only once in the time domain, thus further reducing the computation complexity.

4.7 Computational Complexity of Estimation Techniques

In this section, we compare the complexities of the OMP based complete channel recovery approaches proposed in Section 4.4 and Section 4.5. Since the sparse re-

covery is either done in the time domain (for the combiner time-frequency approach and the time-domain approach) or in the frequency domain, we consider these two distinct cases. The subsequent least squares based channel gain estimation step depends on the number of non-zero support set estimated from the sparse recovery, which is a random whole number given the assumed stopping criterion.

The computational complexity of OMP sparse recovery depends on the size of the sensing matrix and is a function of the iteration step, with the complexity increasing with each step. The number of iteration steps depends on the stopping criteria, or the sparsity level if it is known apriori. Since, we use the noise variance as the stopping threshold, and do not assume the knowledge of the sparsity level, we provide below the computational complexity of the kth iteration and with a total of M training step. The sizes of the sensing matrices for each sparse formulation are also provided for the ease of comparison.

The mathematical operations involved in each iteration of OMP can be summarized as follows. First, the inner product of each column of the sensing matrix is computed with the residual of the previous iteration. Then, the column giving the maximum projection value is identified. The Gram matrix comprising of the column(s) identified till the current step is then computed, following which an inversion of this Gram matrix is performed to compute the weights used for calculating the residual. Finally the residual is updated by subtracting the identified weighted dictionary element. In Table 4.1, we summarize the complex computations required per step of the iteration.

Table 4.1: Computational complexity in the kth iteration of the proposed sparse recovery approaches

	Time-domain sparse recovery	Frequency-domain sparse recovery
Size of the sensing matrix	$NMN_{\mathrm{RF}} \times G_{\mathsf{c}}G_{\mathsf{r}}G_{\mathsf{t}}$	$MN_{\mathrm{RF}} \times G_{\mathsf{r}}G_{\mathsf{t}}$
Compute inner product	$NMN_{\mathrm{RF}}G_{\mathsf{c}}G_{\mathsf{r}}G_{\mathsf{t}}$	$MN_{\mathrm{RF}}G_{\mathsf{r}}G_{\mathsf{t}}$
Find maximum	$G_{\mathsf{c}}G_{\mathsf{r}}G_{\mathsf{t}}$	$G_{\mathsf{r}}G_{\mathsf{t}}$
Compute Gram matrix	$kNMN_{\mathrm{RF}}$	kMN_{RF}
Compute weights	k^2	k^2
Update residual	$kNMN_{\mathrm{RF}}$	kMN_{RF}
Overall cost per iteration	$NMN_{\mathrm{RF}}G_{\mathsf{c}}G_{\mathsf{r}}G_{\mathsf{t}}$	$MN_{\mathrm{RF}}G_{\mathsf{r}}G_{\mathsf{t}}$

4.8 Simulation Results

In this section, the performance of the three proposed channel estimation algorithm are provided. For the compressed sensing estimation of the angles of arrival and departure, orthogonal matching pursuit is used. The channel gains are then estimated using least squares.

We assume uniform linear array (ULA) with half wavelength antenna element separation for the simulations. For such a ULA,

$$\mathbf{a}_{\mathrm{R}}(\phi_\ell) = \frac{1}{\sqrt{N_{\mathrm{r}}}}\begin{bmatrix}1 & e^{\mathrm{j}\pi\cos(\phi_\ell)} & \dots & e^{\mathrm{j}(N_{\mathrm{r}}-1)\pi\cos(\phi_\ell)}\end{bmatrix}^T,$$

and

$$\mathbf{a}_{\mathrm{T}}(\theta_\ell) = \frac{1}{\sqrt{N_{\mathrm{t}}}}\begin{bmatrix}1 & e^{\mathrm{j}\pi\cos(\theta_\ell)} & \dots & e^{\mathrm{j}(N_{\mathrm{t}}-1)\pi\cos(\theta_\ell)}\end{bmatrix}^T.$$

The AoA and AoD quantization used for constructing the transmitter and receiver dictionary matrices are taken from an angle grid of size G_{r} and G_{t}, respectively. This implies that the ℓth column of $\mathbf{A}_{\mathrm{tx}}$ is $\mathbf{a}_{\mathrm{T}}(\tilde{\theta}_\ell)$, where $\tilde{\theta}_\ell = \frac{(\ell-1)\pi}{G_{\mathsf{t}}}$ and the kth column

of $\mathbf{A}_{\rm rx}$ is $\mathbf{a}_{\rm R}(\tilde{\phi}_k)$, where $\tilde{\phi}_k = \frac{(k-1)\pi}{G_{\rm r}}$. The angle quantization used in the phase shifters is assumed to have $N_{\rm Q}$ quantization bits, so that the entries of $\mathbf{F}_m,\ \mathbf{W}_m$, $m = 1,\ 2,\ \cdots,\ M$ are drawn from $\mathcal{A}$, as defined in (4.3), with equal probability. The $N_{\rm p}$ paths of the wideband mmWave channel are assumed to be independently and identically distributed, with delay τ_ℓ chosen uniformly at random from $[0, (N_{\rm c}-1)T_{\rm s}]$, where $T_{\rm s}$ is the sampling interval and $N_{\rm c}$ is the number of delay taps of the channel. The angles of arrival and departure for each of the channel paths are assumed to be distributed independently and uniformly in $[0, \pi]$. The raised cosine pulse shaping signal is assumed to have a roll-off factor of 0.8.

Let $\hat{\mathbf{h}}_{\rm c} \in \mathbb{C}^{N_{\rm c}N_{\rm r}N_{\rm t}\times 1}$ denote the estimated channel vector. We use the following metrics to compare the performance of our proposed channel estimation algorithms:

1) the normalized mean squared error (`NMSE`) of the channel estimates defined as

$$\texttt{NMSE} = \frac{\|\mathbf{h}_{\rm c} - \hat{\mathbf{h}}_{\rm c}\|_2^2}{\|\mathbf{h}_{\rm c}\|_2^2} = \frac{\sum_{d=0}^{N_{\rm c}-1} ||\mathbf{H}_d - \hat{\mathbf{H}}_d||_F^2}{\sum_{d=0}^{N_{\rm c}-1} ||\mathbf{H}_d||_F^2}. \tag{4.43}$$

2) the ergodic spectral efficiency as defined in [79].

Fig. 4.4 shows the `NMSE` as a function of the post combining received signal SNR using the proposed time-domain channel estimation approach. Here we assume $N_{\rm r} = 16$, $N_{\rm t} = 32$, $N_{\rm c} = 4$, $N = 16$ and $N_{\rm p} = 2$. The time domain dictionary is constructed with the parameters $G_{\rm r} = 32$, $G_{\rm t} = 64$, and $G_{\rm c} = 8$. From Fig. 4.4, it can be seen that with training length of even $80-100$ frames, sufficiently low channel estimation error can be ensured. For comparing the recovery performance of the sensing matrix using OMP, we plot the `NMSE` for the case where the sparse recovery is

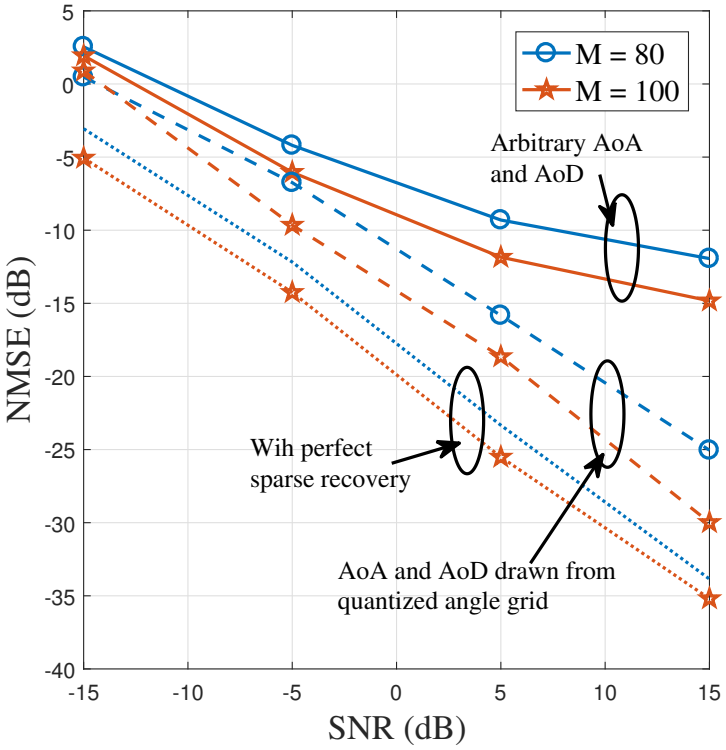

Figure 4.4: Average NMSE as a function of SNR for different training length M when $N_s = 1$ and $N_{\text{RF}} = 1$ using the proposed time-domain channel estimation technique. We assume $N = 16$ symbols per frame for a frequency selective channel of 4 taps. Using the proposed approach, training length of $80 - 100$ is sufficient to ensure very low estimation error, processing completely in the time-domain.

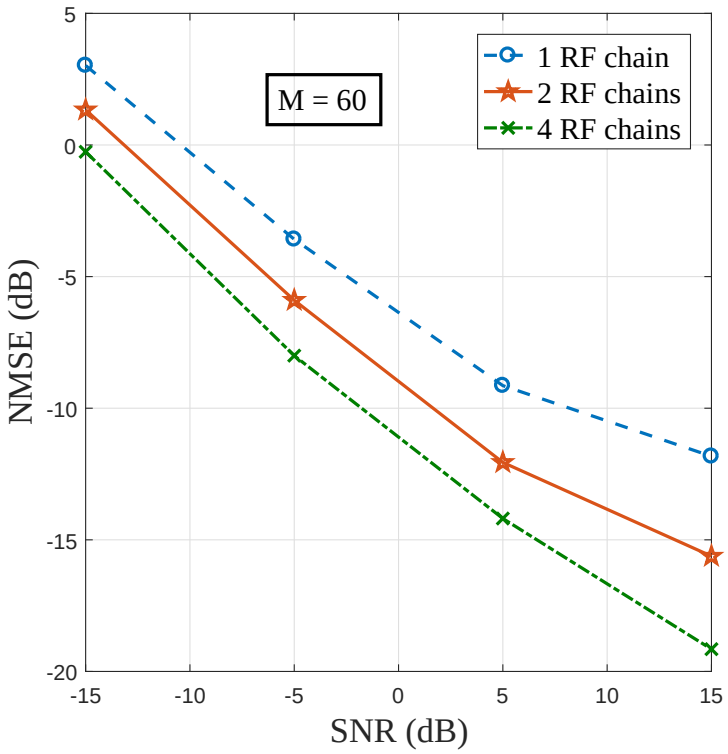

Figure 4.5: Average NMSE for the proposed time-domain channel estimation approach as a function of SNR for different numbers of RF chains used at the transceivers. By employing multiple RF chains at the transceivers, the NMSE performance is improved.

perfect (i.e., the exact angles and delays are provided by a genie). In Fig. 4.4, we also provide the NMSE when the AoA and AoD of the mmWave channel are drawn from quantized grids with $G_{\mathsf{t}} = 64$ and $G_{\mathsf{r}} = 32$ that are used to construct the dictionaries. The gap between the genie-aided perfect sparse recovery curve and that obtained when the parameters fall exactly on the grid elements captures the performance of the recovery algorithm used. Future work could try to narrow this gap using better recovery algorithms.

Fig. 4.5 shows how employing multiple RF chains at the transmitter and receiver can give good improvement in the estimation performance while requiring fewer number of training frame transmissions. We assume the same set of parameters as those used for generating Fig. 4.4, and the proposed time-domain channel estimation approach, while altering the number of RF chains used at the transceivers. In Fig. 4.5, we assume $M = 60$ frames are transmitted for training. The improvement in NMSE performance occurs thanks to a larger number of effective combining beam patterns that scale with the number of RF combiners N_{RF} at the receiver. Similarly, employing multiple RF chains N_{RF} at the transmitter contributes to a larger set of random precoders, resulting in smaller estimation error via compressed sensing. So, larger N_{RF} is preferred to decrease the estimation error and to fully leverage the hybrid architecture in wideband mmWave systems.

In both Fig. 4.4 and Fig. 4.5, we considered averaged NMSE to highlight the effectiveness of the proposed time-domain channel estimation algorithm and the performance gain when multiple RF chains are employed at the transmitter and receiver. In Fig. 4.6, the achievable spectral efficiency is plotted as a function of number of

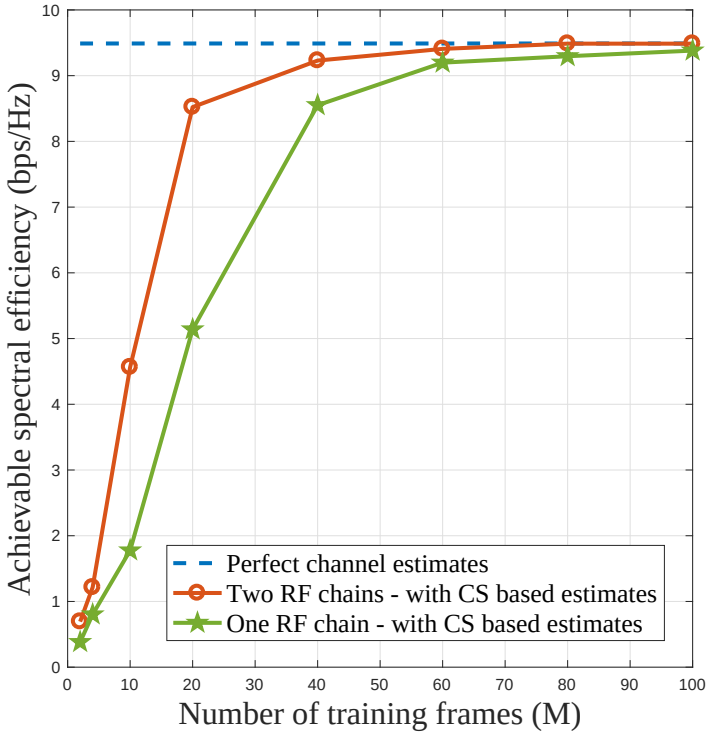

Figure 4.6: Achievable spectral efficiency using the proposed time-domain channel estimation approach as a function of the number of training frames used M for different numbers of RF combiners N_{RF} used at the receiver. Employing multiple RF chains at the transceivers significantly reduces the number of training steps.

training steps M. We assume the same set of parameters as that in Fig. 4.4, and the ergodic spectral efficiency computation used in [79] for SNR = 5 dB. It is observed that having more RF combiners results in fewer number of training frame transmissions to achieve the same spectral efficiency. This is because, with multiple RF chains at the receiver, more effective measurements can be obtained per training frame that is transmitted.

In Fig. 4.4, we see that an error gap exists between the cases where the AoA/AoD fall within the quantized grid and when the AoA/AoD are arbitrary. This gap is especially enhanced at higher SNR levels. Intuitively, thanks to our flexible and generic sparsifying dictionary construction, choosing larger values for G_{r} (G_{t}) in comparison with N_{r} (N_{t}) can further narrow the error gap between the two cases, so does increasing G_{c} in comparison to N_{c} as the dictionary will become more and more *robust*. This capability of our dictionary design is shown in Fig. 4.7 where we plot the `NMSE` for different values of the grid sizes along with the `NMSE` obtained when there is no error due to angle quantization. For plotting this baseline curve, we assume the exact angles are provided by a genie, similar to how we plot the reference curve in Fig. 4.4.

In Fig. 4.8, we plot the `NMSE` as a function of the number of paths in the channel for various RF combiner setups at the receiver. The proposed combined time-frequency domain channel estimation approach is used with $N_{\mathrm{r}} = N_{\mathrm{t}} = 32$, $G_{\mathsf{r}} = G_{\mathsf{t}} = 64$, $N = 32$, $N_{\mathrm{c}} = 8$ and $M = 60$ compressive training steps. In Fig. 4.8, we use sparse recovery in $P = 1$ subcarrier in the frequency domain to estimate the AoAs and AoDs, before switching to the time domain to estimate all the

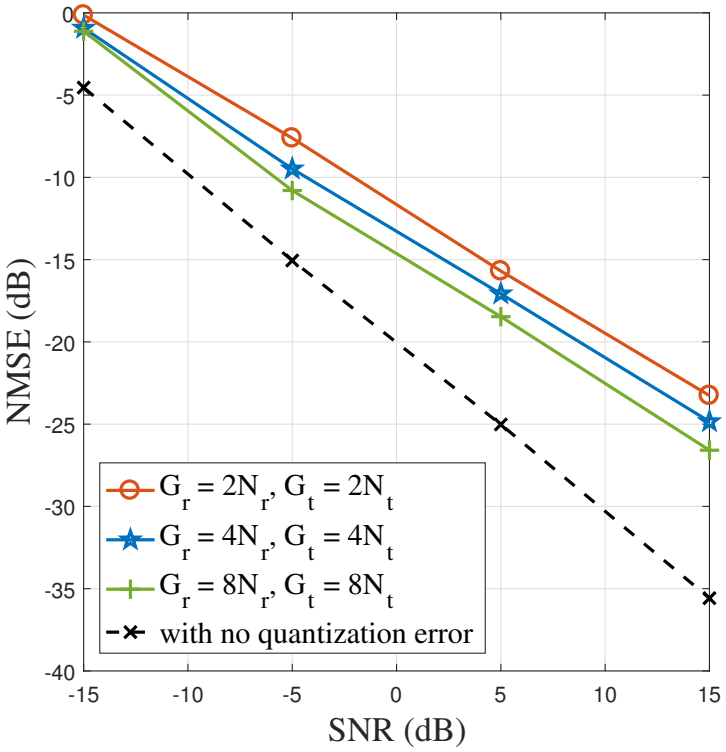

Figure 4.7: Average NMSE versus SNR (assuming $N_{\mathrm{r}} = N_{\mathrm{t}} = 16$) using the proposed frequency-domain channel estimation approach. The number of angles in the quantized grid used for generating the dictionary is denoted as G_{r} (for AoA) and G_{t} (for AoD). The figure shows how increasing G_{t} and G_{r} reduces the grid quantization error for a given antenna size.

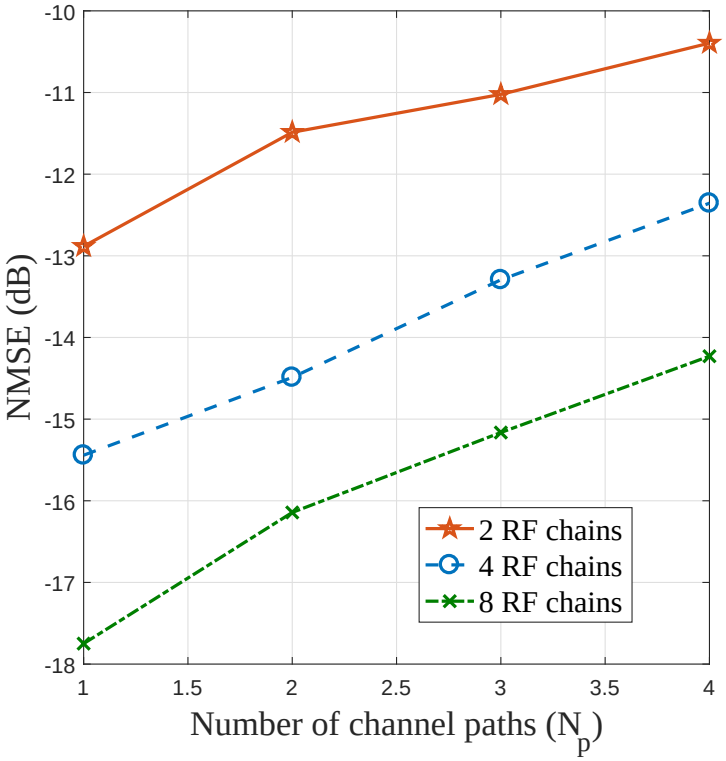

Figure 4.8: Average NMSE versus the number of paths N_{p}, for different hybrid configurations at the transceivers using the proposed combined time-frequency domain channel estimation approach. Increasing N_{p} increases the number of unknown parameters of the channel, and hence higher number of compressive measurements are required to get the required target estimation error performance.

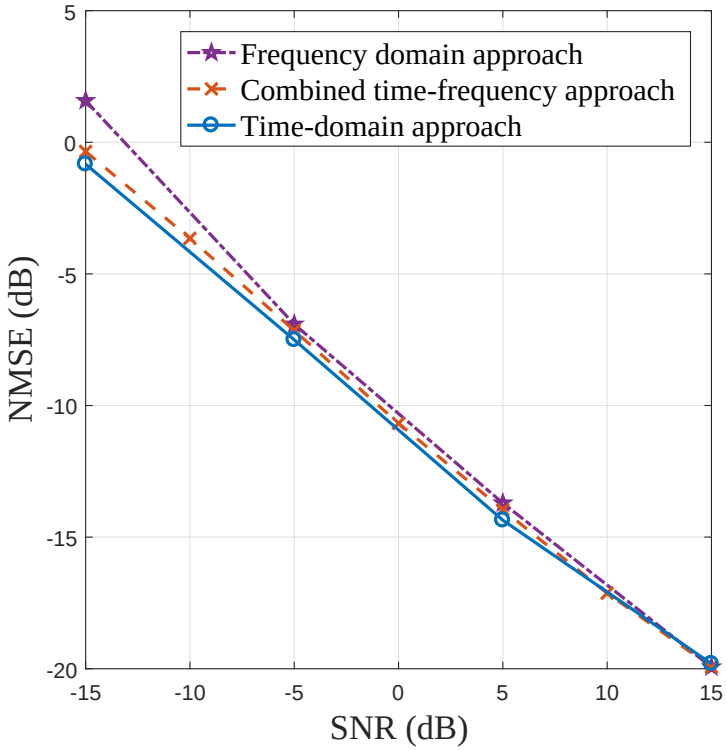

Figure 4.9: Plot showing the error performance of the three compressed sensing based channel estimation approaches proposed in this chapter as a function of SNR. At low SNR the combine time-frequency approach has the least average `NMSE`, while at higher SNRs, all the three proposed approaches give similar performance.

gain coefficients of the channel paths. As N_{p} is increased, the number of unknown parameters in the channel increases, thus increasing the estimation error for a given number of training steps and hardware configuration. Increasing the RF combiners, however, helps reduce the `NMSE` to meet a target estimation error performance.

In Fig. 4.9, we look the error performance of the three proposed channel estimation approaches by plotting the `NMSE` as a function of SNR. We assume $N_{\mathrm{r}} = N_{\mathrm{t}} = 32$,

$G_{\mathtt{r}} = G_{\mathtt{t}} = 64$, $M = 60$, $N_{\mathrm{c}} = 4$ and $N_{\mathrm{p}} = 2$. The number of RF chains at the transceivers N_{RF} is assumed to be 4. The combined time-frequency approach is assumed to use OMP on $P = 1$ subcarrier in the frequency domain to recover the angles of arrival and departure. For constructing the time domain dictionary, we assume $G_{\mathrm{c}} = 2N_{\mathrm{c}}$ delay quantization parameter. It can be seen that the time domain and combined time-frequency approaches give the best error performance whereas the proposed frequency domain approach results is large estimation error, especially at lower SNRs. This is mainly due to the accumulation of error incurred due to K parallel OMPs in the frequency, which is avoided in the combined time-frequency approach and the proposed time domain approach, which invoke the sparse recovery algorithm only once (when $P = 1$). At higher SNRs, however, the three proposed approaches give similar estimation error performance.

In Fig. 4.10, we compare the three proposed approaches' error performance as the number of channel paths is increased. We set $G_{\mathtt{r}} = G_{\mathtt{t}} = 2N_{\mathrm{r}} = 2N_{\mathrm{t}} = 64$, and assume 4 RF chains at the transceivers. The training frame length of $N = 16$ is assumed for the wideband channel of $N_{\mathrm{c}} = 4$ delay taps. For each case, $M = 60$ training steps are assumed. As the number of channel paths is increased, all the approaches perform worse. In particular, for a given delay quantization parameter $G_{\mathrm{c}} = 2N_{\mathrm{c}}$, assumed for the time domain approach's plot in Fig. 4.10, the degradation in `NMSE` is significant as the delay estimation results in more error. For smaller number of channel paths, however, the time domain approach gives lower channel estimation error. The plot also shows that when the number of delay taps is smaller compared to the number of paths in the channel, frequency domain techniques perform better.

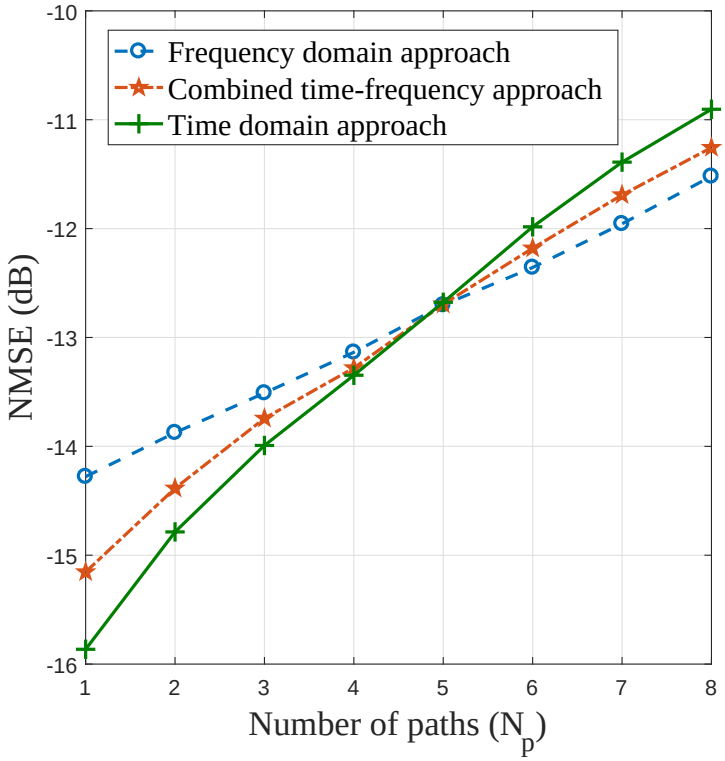

Figure 4.10: Plot showing the error performance of the three proposed approaches, as a function of the number of paths N_{p} in the channel. Increasing N_{p} degrades the average `NMSE` performance. While the proposed time domain approach gives the minimum average `NMSE` when the number of paths is small, the frequency domain approach gives the best error performance for larger N_{p}.

A comparison of the performance of the three proposed approaches as a function of the number of training steps is shown in Fig. 4.11. We set the SNR to 5 dB here and assume $G_{\mathtt{r}} = G_{\mathtt{t}} = 2N_{\mathrm{r}} = 2N_{\mathrm{t}} = 64$. Each training frame is assumed to be of length 16 symbols, for a frequency selective mmWave channel of tap length 4, and channel paths 2. The `NMSE` plots in Fig. 4.11 is assumed 4 RF chains at the transceivers with 2 bit quantization at the phase shifters during channel estimation. It can be seen that while, with a few training steps the combined time frequency approach and the proposed frequency domain approach outperform the time domain approach, with larger number of training steps, the time domain approach gives the least `NMSE`.

To compare the overhead in channel training in the proposed compressive sensing based approaches, consider the short preamble structure used in IEEE 802.11ad [11], which is of duration 1.891μs. At a chip rate of 1760 MHz, this short preamble consisting of the short training frame (STF) and the channel estimation frame (CEF) amounts to more than 3200 symbols. After the end of this short preamble transmission, IEEE 802.11ad beamforming protocol then switches to a different beam pair combination, and the process is repeated recursively to estimate the best set of beamforming directions. For the setting in Fig. 4.11, however, $MN = 1600$ symbols are only required for the proposed approaches to achieve low average `NMSE` and explicit estimation of the frequency selective MIMO channel.

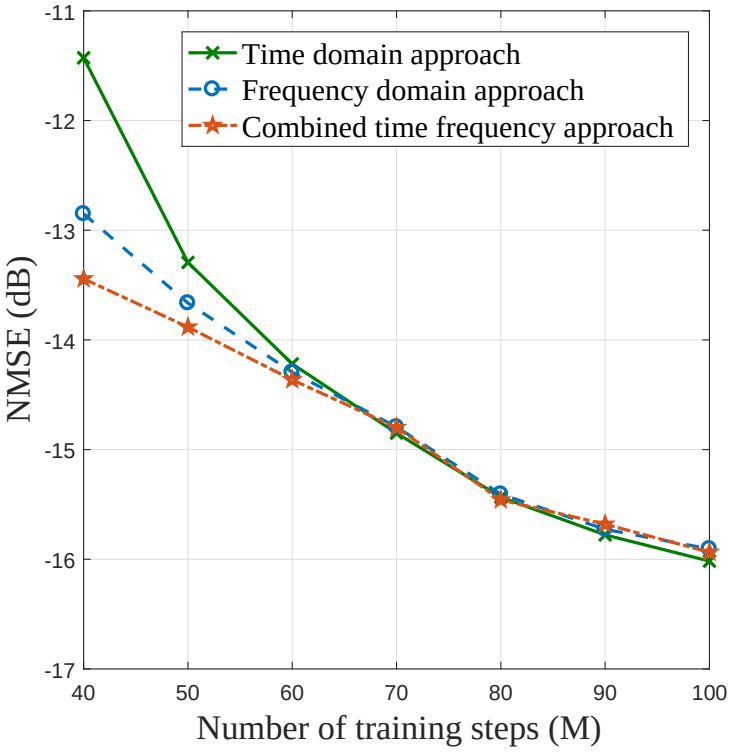

Figure 4.11: Plot showing the error performance of the three proposed approaches, as a function of the number of training steps M. More number of compressive measurements lead to better estimation error performance at the expense of higher signaling overhead. The combined time-frequency approach gives the best trade-off between low training overhead and minimum average NMSE performance.

4.9 Conclusion

In this chapter, we proposed wideband channel estimation algorithms for frequency selective mmWave systems using a hybrid architecture at the transmitter and receiver. The system model adopts zero padding that allows enough time for switching the analog beams and, hence, well matches the hybrid architectures. The proposed channel estimation algorithms are based on sparse recovery and can support MIMO operation in mmWave systems since the entire channel is estimated after the beam training phase. Three different approaches - in purely time, in purely frequency and a combined time frequency approach were proposed, that can be used in both SC-FDE and OFDM based wideband mmWave systems. Leveraging the frame structure and the hybrid architecture at the transceivers, it was shown that compressed sensing tools can be used for mmWave channel estimation. Simulation results showed that the proposed algorithms required very few training frames to ensure low estimation error. It was shown that further reduction in the training overhead and estimation error can be obtained by employing multiple RF chains at the transceivers.

Chapter 5

Optimal Frequency-flat Precoding via Compressive Subspace Estimation

5.1 Overview

Millimeter wave (mmWave) MIMO communication is a key feature of next generation wireless systems. The selection of precoders and combiners for wideband mmWave channels has involved frequency-selective designs based on channel state information. In this chapter[1], we show that under some assumptions, the dominant subspaces of the frequency domain channel matrices are equivalent. This means that semi-unitary frequency-flat precoding and combining are sufficient when there is not too much scattering in the channel. It also motivates the use of techniques such as compressive subspace estimation as an alternative to estimating the full channel. Importantly, this chapter proposes methods to design optimal precoders and combiners that are cost effective and easy to implement. This is critical for hardware-constrained mmWave wearable devices.

[1]Part of the content in this chapter has been published as a letter: K. Venugopal, N. González-Prelcic and R. W. Heath, Jr., "Optimality of Frequency Flat Precoding in Frequency Selective Millimeter Wave Channels," IEEE Wireless Communications Letters, March 2017. This work was supervised by Prof. Nuria González-Prelcic and Prof. Robert Heath.

5.2 Introduction

The use of large antenna arrays, and directional transmission and reception are key enabling technologies for wireless systems operating at mmWave frequencies [92]. Both analog-only and hybrid beamforming architectures have been proposed to reduce the cost and power consumption in mixed signal components of a fully-digital MIMO system operating at mmWave [34, 55]. While hybrid architectures are desirable for supporting multi-stream communication at mmWave, the analog processing stage is frequency-flat, so it can not perfectly reproduce the optimum frequency-selective precoders.

Some prior work on frequency-selective mmWave systems [80, 93, 94] involved precoding with a frequency-flat analog precoder followed optionally by a frequency-selective baseband precoder. This was found to be optimum in terms of the achievable spectral efficiency for a given analog codebook and a flexible baseband precoder. The potential optimality of optimal frequency-flat precoders and combiners was not considered.

In this paper, we show that frequency-flat precoding and combining, assuming semi-unitary precoding, is optimum in frequency-selective MIMO channels with few paths, as found in mmWave systems. This means that frequency-selective precoding is not necessarily required in MIMO systems operating at mmWave frequencies. Further, this result motivates the design of the precoder based on compressive covariance or subspace estimation instead of explicit channel estimation exploiting sparsity [64, 68]. We propose various subspace estimation strategies in this context and compare how such approaches give advantage over the complete MIMO channel

estimation algorithms depending on the channel parameters.

5.3 System Model

Consider a wideband mmWave system with N_{t} transmit antennas and N_{r} receive antennas. A geometric channel model [64,79] consisting of R paths is assumed for representing the frequency-selective channel [2]. The ℓth path has a complex gain $\alpha_\ell \in \mathbb{C}$, delay $\tau_\ell \in \mathbb{R}$, and angles of arrival and departure (AoA/AoD) $\phi_\ell \in [0, 2\pi)$ and $\theta_\ell \in [0, 2\pi)$. Assuming a pulse shaping filter denoted as $p(\tau)$, the discrete-time, frequency-selective channel with N_{c} delay taps can be represented in terms of the antenna array response vectors of the receiver $\mathbf{a}_{\mathrm{R}}(\phi_\ell) \in \mathbb{C}^{N_{\mathrm{r}}\times 1}$ and the transmitter $\mathbf{a}_{\mathrm{T}}(\theta_\ell) \in \mathbb{C}^{N_{\mathrm{t}}\times 1}$ [79]. Sampling with period T_{s}, the discrete-time MIMO channel is

$$\mathbf{H}_d = \sum_{\ell=1}^{R} \alpha_\ell p(dT_{\mathrm{s}} - \tau_\ell)\mathbf{a}_{\mathrm{R}}(\phi_\ell)\mathbf{a}_{\mathrm{T}}^*(\theta_\ell), \tag{5.1}$$

for $d = 0, 1, \ldots, N_{\mathrm{c}} - 1$. To obtain a more compact representation of $\mathbf{H}_d$, we define the matrices $\mathbf{A}_{\mathrm{R}} \in \mathbb{C}^{N_{\mathrm{r}}\times R}$, $\mathbf{A}_{\mathrm{T}} \in \mathbb{C}^{N_{\mathrm{t}}\times R}$, and a diagonal matrix $\mathbf{P}_d \in \mathbb{C}^{R\times R}$. The columns of $\mathbf{A}_{\mathrm{R}}$ and $\mathbf{A}_{\mathrm{T}}$ are given by $\{\mathbf{a}_{\mathrm{R}}(\theta_\ell)\}_{\ell=1}^{R}$ and $\{\mathbf{a}_{\mathrm{T}}(\theta_\ell)\}_{\ell=1}^{R}$ respectively, and the ℓth diagonal entry of $\mathbf{P}_d$ is $\alpha_\ell p(dT_{\mathrm{s}} - \tau_\ell)$. Using these definitions

$$\mathbf{H}_d = \mathbf{A}_{\mathrm{R}}\mathbf{P}_d\mathbf{A}_{\mathrm{T}}^*, \tag{5.2}$$

which provides a matrix representation of the dth delay tap of the channel.

Multicarrier (MC) transmission or a single carrier with frequency division multiplexing (SC-FDM) is assumed, with $K > N_{\mathrm{c}}$ denoting the number of subcarriers in

[2]For the purpose of this chapter, and in the context of subspace estimation, we say that R corresponds to the dimension of the dominant subspace of the channel.

the frequency domain. The complex channel matrix in the frequency domain can be written as

$$\mathbf{H}[k] = \sum_{d=0}^{N_{\mathrm{c}}-1} \mathbf{H}_d e^{-\mathrm{j}\frac{2\pi kd}{K}} \tag{5.3}$$

for $k = 0, 1, \ldots, K-1$. To express (5.3) in matrix form, let $\mathbf{P}[k] = \sum_{d=0}^{N_{\mathrm{c}}-1} \mathbf{P}_d e^{-\mathrm{j}\frac{2\pi kd}{K}}$. Substituting (5.2) into (5.3), using the fact that the matrices $\mathbf{A}_{\mathrm{R}}$ and $\mathbf{A}_{\mathrm{T}}$ are independent of d then

$$\mathbf{H}[k] = \sum_{d=0}^{N_{\mathrm{c}}-1} \mathbf{A}_{\mathrm{R}} \mathbf{P}_d \mathbf{A}_{\mathrm{T}}^{*} e^{-\mathrm{j}\frac{2\pi kd}{K}} \tag{5.4}$$

$$= \mathbf{A}_{\mathrm{R}} \mathbf{P}\left[k\right] \mathbf{A}_{\mathrm{T}}^{*}. \tag{5.5}$$

The number of paths R is assumed to be smaller than the number of delay taps N_{c} in the frequency-selective mmWave channel, which is reasonable due to the memory in the pulse shaping function. When R is thought of as the dimension of the dominant subspace of the MIMO channel, also then, it can be seen that R is much smaller than the dimensions of the frequency-selective mmWave MIMO channel [95].

Appropriate signal processing (for MC/SC-FDM) can be used at the transmitter and the receiver [84] to obtain K parallel narrowband channels in the frequency domain. For N_{s} stream transmission, let $\mathbf{x}[k] \in \mathbb{C}^{N_{\mathrm{s}} \times 1}$ denote the complex symbol transmitted in the kth subcarrier of the data frame. Assuming frequency-selective precoding with a matrix $\mathbf{F}[k] \in \mathbb{C}^{N_{\mathrm{t}} \times N_{\mathrm{s}}}$ and combining with $\mathbf{W}[k] \in \mathbb{C}^{N_{\mathrm{r}} \times N_{\mathrm{s}}}$ during the transmission-reception of the data frame, the post combining received symbol in the kth subcarrier can be written as

$$\mathbf{y}\left[k\right] = \mathbf{W}^{*}[k]\mathbf{H}[k]\mathbf{F}[k]\mathbf{x}\left[k\right] + \mathbf{W}[k]^{*}\mathbf{n}\left[k\right], \tag{5.6}$$

where $\mathbf{n}[k] \sim \mathcal{N}(0, \sigma^2\mathbf{I})$ is the circularly symmetric complex Gaussian distributed additive noise vector of size N_{r}. Next we argue that in some cases the precoder $\mathbf{F}[k]$ and $\mathbf{W}[k]$ do not have to vary with frequency k.

5.4 Optimality of Frequency-flat Precoding

Under some assumptions, we now show that the K MIMO channel matrices defined in (5.3) have the same row spaces and column spaces. Let $\mathcal{C}(\mathbf{A})$ denote the column space of $\mathbf{A}$ and $\mathcal{R}(\mathbf{A})$ the row space of $\mathbf{A}$. Using this notation, we define the subspaces $\mathcal{H}_c = \mathcal{C}(\mathbf{A}_{\mathrm{R}})$ and $\mathcal{H}_r = \mathcal{R}(\mathbf{A}_{\mathrm{T}}^*)$.

Proposition 6 *Assuming that $\mathbf{A}_{\mathrm{R}}$ and $\mathbf{A}_{\mathrm{T}}$ have full column rank and $\mathbf{P}[k]$ is full rank, the frequency domain MIMO channel matrices $\mathbf{H}[k]$, $k = 0, 1, \cdots, K-1$, have the same column space $\mathcal{H}_c$ and the same row space $\mathcal{H}_r$.*

Proof: From (5.5), $\mathcal{R}(\mathbf{H}[k]) \subseteq \mathcal{H}_r$ with equality when $\mathbf{A}_{\mathrm{R}}\mathbf{P}[k]$ has full column rank, which is true when $\mathbf{A}_{\mathrm{R}}$ has full column rank and $\mathbf{P}[k]$ is full rank. Similarly, $\mathcal{C}(\mathbf{H}[k]) \subseteq \mathcal{H}_c$ with equality when $\mathbf{P}[k]\mathbf{A}_{\mathrm{T}}^*$ has full row rank, which is true when $\mathbf{A}_{\mathrm{T}}$ has full column rank and $\mathbf{P}[k]$ is full rank. □

Assuming that $\mathbf{P}[k]$ is full rank is reasonable since the diagonal elements are the Fourier transform of shifted sampled Nyquist pulse shapes and the path gains are non-zero. The assumption that $\mathbf{A}_{\mathrm{R}}$ and $\mathbf{A}_{\mathrm{T}}$ have full column rank holds for typical array geometries, like the uniform linear array or uniform patch array, with small enough element spacing and distinct angles of arrival and departure.

Corollary 7 *Frequency-flat precoding (and combining) is optimum in frequency-selective mmWave channels under the assumptions of semi-unitary precoding (and combining) and a small number of paths ($R < N_{\mathrm{t}}$ and $R < N_{\mathrm{r}}$), if $\mathbf{A}_{\mathrm{R}}$ and $\mathbf{A}_{\mathrm{T}}$ have full column rank.*

Proof: The conventional semi-unitary frequency-selective precoder design is based on the singular value decomposition (SVD) of $\mathbf{H}[k] = \mathbf{U}[k]\mathbf{\Lambda}[k]\mathbf{V}^*[k]$, where $\mathbf{F}[k] = [\mathbf{V}[k]]_{:,1:N_{\mathrm{s}}}$ with $N_{\mathrm{s}} \leq \min(N_{\mathrm{t}}, N_{\mathrm{r}})$. If the number of paths is small, and $\mathbf{A}_{\mathrm{T}}$ has full column rank then $\mathrm{rank}(\mathbf{A}_{\mathrm{T}}) = R$ and it suffices to take $N_{\mathrm{s}} = R$. In this case, the columns of $\mathbf{F}[k]$ are a basis for $\mathcal{H}_r$. Based on Proposition 6, though, $\mathcal{H}_r$ is the same for all k thus a common basis for $\mathcal{H}_r$ given by $\mathbf{F}_{\mathrm{ff}}$ can be used for all subcarriers. A similar argument applies to using a single $\mathbf{W}_{\mathrm{ff}}$ for combining across all subcarriers. This means that the precoding and combining is independent of the subcarrier index. □

5.5 Achievable Rate with Frequency-flat Precoders

We choose the number of streams N_{s} to be equal to the rank of the MIMO channel matrices for each subcarrier k, given by $\min(R, N_{\mathrm{r}}, N_{\mathrm{t}})$. Based on the SVD of $\mathbf{H}[k]$ in the proof of Corollary 7, the conventional frequency-selective precoder $\mathbf{F}[k] = [\mathbf{V}[k]]_{:,1:N_{\mathrm{s}}}$ and combiner $\mathbf{W}[k] = [\mathbf{U}[k]]_{:,1:N_{\mathrm{s}}}$ results in achievable spectral efficiency

$$\mathsf{R}_{\mathrm{fs}} = \frac{1}{K}\sum_{k=1}^{K} \log_2 \left| \mathbf{I} + \frac{\mathrm{SNR}}{N_{\mathrm{s}}} \hat{\mathbf{\Lambda}}^2[k] \right|, \tag{5.7}$$

where SNR $= \frac{P}{K\sigma^2}$, P is the average transmitted power, and $\hat{\mathbf{\Lambda}}[k] = [\mathbf{\Lambda}[k]]_{1:N_\mathrm{s},1:N_\mathrm{s}}$. The maximal achievable rate can be derived by performing an additional spatial water-filling step [96]. In the sequel, for comparison, we show the maximum achievable spectral efficiency, allocating power along the spatial streams via water-filling assuming a uniform, constant power constraint for the MIMO channel per subcarrier $(= \frac{P}{K})$.

Let the frequency-flat precoder $\mathbf{F}_\mathrm{ff}$ be a semi-unitary matrix whose columns span $\mathcal{H}_r$. Similarly, let $\mathbf{W}_\mathrm{ff}$ be a semi-unitary matrix whose columns span $\mathcal{H}_c$. Since all the column spaces of the matrices are the same, we can write $\mathbf{W}_\mathrm{ff} = \mathbf{W}[k]\mathbf{Q}_\mathsf{W}[k]$, where $\mathbf{Q}_\mathsf{W}[k] \in \mathbb{C}^{N_\mathrm{s}\times N_\mathrm{s}}$ is a unitary rotation matrix that accounts for the unitary invariance in the representation of a point on the Grassmann manifold. Similarly, we can write $\mathbf{F}_\mathrm{ff} = \mathbf{F}[k]\mathbf{Q}_\mathsf{F}[k]$, where $\mathbf{Q}_\mathsf{F}[k] \in \mathbb{C}^{N_\mathrm{s}\times N_\mathrm{s}}$ is another unitary rotation matrix. Further, since the frequency-flat combiner is semi-unitary, the noise covariance of the post combining received signal in (5.6) is $\sigma^2\mathbf{I}$. Therefore, the achievable spectral efficiency using the proposed frequency-flat precoder is

$$\mathsf{R}_\mathrm{ff} = \frac{1}{K}\sum_{k=1}^{K}\log_2\left|\mathbf{I} + \frac{\mathrm{SNR}}{N_\mathrm{s}}\mathbf{W}_\mathrm{ff}^*\mathbf{H}[k]\mathbf{F}_\mathrm{ff}\mathbf{F}_\mathrm{ff}^*\mathbf{H}^*[k]\mathbf{W}_\mathrm{ff}\right|. \tag{5.8}$$

Note that the effective channel matrix with the optimal frequency-flat precoder and combiner is $\mathbf{H}_\mathrm{eff}[k] = \mathbf{W}_\mathrm{ff}^*\mathbf{H}[k]\mathbf{F}_\mathrm{ff}$, which can be written as

$$\mathbf{H}_\mathrm{eff}[k] = \mathbf{Q}_\mathsf{W}^*[k]\mathbf{W}^*[k]\mathbf{U}[k]\mathbf{\Lambda}[k]\mathbf{V}^*[k]\mathbf{F}[k]\mathbf{Q}_\mathsf{F}[k] \tag{5.9}$$

$$= \mathbf{Q}_\mathsf{W}^*[k]\hat{\mathbf{\Lambda}}[k]\mathbf{Q}_\mathsf{F}[k]. \tag{5.10}$$

Then (5.8) simplifies to

$$\mathsf{R}_{\text{ff}} = \frac{1}{K}\sum_{k=1}^{K}\log_2\left|\mathbf{I} + \frac{\text{SNR}}{N_{\text{s}}}\mathbf{Q}_{\mathsf{W}}^{*}[k]\hat{\mathbf{\Lambda}}^2[k]\mathbf{Q}_{\mathsf{W}}[k]\right| \tag{5.11}$$

$$\stackrel{(a)}{=} \frac{1}{K}\sum_{k=1}^{K}\log_2\left|\mathbf{I} + \frac{\text{SNR}}{N_{\text{s}}}\hat{\mathbf{\Lambda}}^2[k]\right| = \mathsf{R}_{\text{fs}}. \tag{5.12}$$

In (5.12), $\stackrel{(a)}{=}$ follows from the matrix identity $|\mathbf{I} + \mathbf{ABC}| = |\mathbf{I} + \mathbf{BCA}|$ and since $\mathbf{Q}_{\mathsf{W}}[k]$ is unitary.

It is important to note that the proposed precoder-combiner does not necessarily diagonalize the MIMO channel per-subcarrier $\mathbf{H}_{\text{eff}}[k]$, like the usual SVD-based frequency-selective precoding and combining. Therefore, the transmitted symbol may be detected using optimal digital receiver strategies with the knowledge of the $N_{\text{s}} \times N_{\text{s}}$ matrix $\mathbf{H}_{\text{eff}}[k]$. This low dimensional effective channel may be estimated using convention digital MIMO channel estimation techniques and feedback of this channel is not required, since there is no additional per-subcarrier digital precoding layer. As shown in the simulations, small gains with frequency-selective precoding can be achieved using water-filling across space and/or frequency. We also show in the simulations that the optimality of the frequency-flat beamformers does not depend on the number of subcarriers K or the number of delay taps N_{c}.

5.6 Compressive Subspace Estimation

Given that all the channel matrices have the same row and column spaces, $\mathcal{H}_c$ and $\mathcal{H}_r$, the knowledge of these subspaces is sufficient for designing the optimal precoders and combiners. The purpose of this section is to illustrate how this insight

from Section 5.4 can be used to replace the channel estimation stage, central for a conventional precoder design, by a compressive subspace estimation. Accordingly, the system design problem boils down to estimating the orthogonal bases of the row and column spaces of the $N_{\mathrm{r}} \times N_{\mathrm{t}}$ channel matrices.

While iterative approaches to estimate the right and left singular subspaces of mmWave MIMO channels have been considered previously [73], we use a variation of the nuclear norm minimization approach in [97] to perform the compressive subspace estimation. Compressive sensing based approaches are interesting because they only require a small number of random, linear measurements [97, 98] when estimating the low rank subspace of large dimensional matrices.

Let $\mathbf{F}_{(m)} \in \mathbb{C}^{N_{\mathrm{t}} \times N_{\mathrm{s}}}$ denote the precoder used for the mth training frame, and $\mathbf{W}_{(m)} \in \mathbb{C}^{N_{\mathrm{r}} \times N_{\mathrm{s}}}$ denote the corresponding combiner. Then, with $N_{\mathrm{s}} \leq \min(N_{\mathrm{r}}, N_{\mathrm{t}})$ and denoted the mth training data as $\mathbf{x}_{(m)}$, the compressive measurement at the receiver for the kth subcarrier is

$$\mathbf{y}_{(m)}[k] = \mathbf{W}_{(m)}^{*} \mathbf{H}[k] \mathbf{F}_{(m)} \mathbf{x}_{(m)}[k] + \mathbf{W}_{(m)}^{*} \mathbf{n}[k]. \tag{5.13}$$

Since $\mathbf{H}[k]$ is a low rank channel for each k (the condition under which the proposed frequency-flat precoding and combining are optimal), nuclear norm relaxation may be used for low rank matrix estimation. Following this, the row and column principal subspaces can be evaluated. That is, the channel estimate $\hat{\mathbf{H}}[k]$ is obtained by solving the following optimization problem:

$$\begin{aligned} \min_{\mathbf{H} \in \mathbb{C}^{N_{\mathrm{r}} \times N_{\mathrm{t}}}} \quad & \|\mathbf{H}\|_{*} \\ \text{s.t. } \|\mathbf{W}_{(m)}^{*} \mathbf{H} \mathbf{F}_{(m)} \mathbf{x}_{(m)}[k] - \mathbf{y}_{(m)}[k]\| \leq \epsilon \quad & \text{for } m = 1, 2, \cdots, M. \end{aligned} \tag{5.14}$$

Note that M is the number of compressed measurements in (5.14), and $\|\mathbf{H}\|_*$ denotes the nuclear norm of matrix $\mathbf{H}$.

An alternating minimization technique inspired from [97], but with complex input corresponding to the compressive measurements and the measurement matrices may be used to directly estimate the row and column principal subspaces. We provide this modified alternating minimization technique for subspace estimation in Algorithm 1.

Algorithm 1 : Modified Alternating Minimization for Low Rank Subspace Estimation

Input: Measurements $\mathbf{y}_{(1:M)}$, training data $\mathbf{x}_{(1:M)}$, frequency-flat training precoders $\mathbf{F}_{(1:M)}$ and combiners $\mathbf{W}_{(1:M)}$, number of iterations M'

Divide $\left(\mathbf{y}_{(1:M)}, \mathbf{x}_{(1:M)}, \mathbf{F}_{(1:M)}, \mathbf{W}_{(1:M)}\right)$ into $2M'+1$ sets (of size μ each) with the mth set being

$\mathbf{y}^m = \mathbf{y}_{((m-1)\mu+1:m\mu)} = \left\{\mathbf{y}_1^m, \mathbf{y}_2^m, \cdots, \mathbf{y}_\mu^m\right\}$

$\mathbf{x}^m = \mathbf{x}_{((m-1)\mu+1:m\mu)} = \left\{\mathbf{x}_1^m, \mathbf{x}_2^m, \cdots, \mathbf{x}_\mu^m\right\}$

$\mathbf{F}^m = \mathbf{F}_{((m-1)\mu+1:m\mu)} = \left\{\mathbf{F}_1^m, \mathbf{F}_2^m, \cdots, \mathbf{F}_\mu^m\right\}$

$\mathbf{W}^m = \mathbf{W}_{((m-1)\mu+1:m\mu)} = \left\{\mathbf{W}_1^m, \mathbf{W}_2^m, \cdots, \mathbf{W}_\mu^m\right\}$

Initialize:

$\mathbf{U}_0 =$ top-R left singular vectors of $\frac{1}{\mu N_\mathrm{s}} \sum_{i=1}^{\mu} \sum_{j=1}^{N_\mathrm{s}} \left[\mathbf{y}_i^0\right]_j \left[\mathbf{W}_i^0\right]_{:,j} \left(\mathbf{F}_i^0 \mathbf{x}_i^0\right)^*$

for $m = 0$ to $M'-1$ **do**

$\mathbf{y} \leftarrow \mathbf{y}^{2m+1}$, $\mathbf{x} \leftarrow \mathbf{x}^{2m+1}$, $\mathbf{F} \leftarrow \mathbf{F}^{2m+1}$, $\mathbf{W} \leftarrow \mathbf{W}^{2m+1}$

$\hat{\mathbf{V}}_{m+1} \leftarrow \underset{\mathbf{V} \in \mathcal{C}^{N_\mathrm{t} \times R}}{\arg\min} \sum_{i=1}^{\mu} \|\mathbf{y}_i - \mathbf{W}_i^* \mathbf{U}_m \mathbf{V}^* \mathbf{F}_i \mathbf{x}_i\|_2^2$

$\mathbf{V}_{m+1} = QR\left(\hat{\mathbf{V}}_{m+1}\right)$ % orthonormalize $\hat{\mathbf{V}}_{m+1}$

$\mathbf{y} \leftarrow \mathbf{y}^{2m+2}$, $\mathbf{x} \leftarrow \mathbf{x}^{2m+2}$, $\mathbf{F} \leftarrow \mathbf{F}^{2m+2}$, $\mathbf{W} \leftarrow \mathbf{W}^{2m+2}$

$\hat{\mathbf{U}}_{m+1} \leftarrow \underset{\mathbf{U} \in \mathcal{C}^{N_\mathrm{r} \times R}}{\arg\min} \sum_{i=1}^{\mu} \|\mathbf{y}_i - \mathbf{W}_i^* \mathbf{U} \mathbf{V}_{m+1}^* \mathbf{F}_i \mathbf{x}_i\|_2^2$

$\mathbf{U}_{m+1} = QR\left(\hat{\mathbf{U}}_{m+1}\right)$ % orthonormalize $\hat{\mathbf{U}}_{m+1}$

end for

Output: Semi-unitary matrices $\mathbf{U}_{M'}$ and $\mathbf{V}_{M'}$

The estimated left and right orthogonal vectors constitute the columns of the optimal frequency-flat combiner and precoder. This is unlike most of the prior work on mmWave frequency-selective systems where at least the baseband precoder-combiner are subcarrier specific, while the analog processing is frequency-flat [80].

Note that in the discussion till now, we described a few compressive subspace estimation techniques that have used in literature. Various algorithms that are optimized for computational complexity and efficiency with guaranteed performance criteria have been reported previously. None of these, however, elaborate algorithms that estimate subspaces that are common to multiple channels, directly with multiple compressive measurements. Hence, we propose and elaborate next, a few compressive subspace estimation techniques, that leverage the fact that the MIMO channels corresponding to all the subcarriers have the same row and column spaces.

5.6.1 Using the "Best" Subcarrier

In this proposed approach, we first identify that subcarrier which has the maximum received SNR and then estimate the subspaces using nuclear norm minimization or the modified alternating minimization technique in Algorithm 1. The advantage of this approach is that the optimal frequency-flat precoder and combiner can be evaluated with minimum computational complexity. The disadvantage is that the compressive measurements of the other subcarriers are not utilized here.

To formalize, let

$$\hat{k} = \arg\min_{k} \sum_{m=1}^{M} \|\mathbf{y}_{(m)}[k]\|_2^2. \tag{5.15}$$

Then, for this proposed compressive subspace estimation approach, the constraints for the optimization problem in (5.14) are $\|\mathbf{W}^*_{(m)}\mathbf{H}\mathbf{F}_{(m)}\mathbf{x}_{(m)}[\hat{k}] - \mathbf{y}_{(m)}[\hat{k}]\| \leq \epsilon$, for $m = 1, 2, \cdots M$ for estimating $\hat{\mathbf{H}}[\hat{k}]$. Alternatively, Algorithm 1 with input $\mathbf{y}_{(1:M)}[\hat{k}]$, $\mathbf{x}_{(1:M)}[\hat{k}]$, $\mathbf{F}_{(1:M)}$ and $\mathbf{W}_{(1:M)}$ may also be used to estimate the semi-unitary matrices $\mathbf{U}_{M'}[\hat{k}]$ and $\mathbf{V}_{M'}[\hat{k}]$, in this proposed approach.

Since MIMO channels corresponding to all the subcarriers have the same row and column spaces, the subspaces estimated from the best subcarrier can then used to derive the frequency-flat precoder and combiner. Accordingly, the SVD of the estimated MIMO channel $\hat{\mathbf{H}}[\hat{k}] = \mathbf{U}[\hat{k}]\mathbf{\Lambda}[\hat{k}]\mathbf{V}^*[\hat{k}]$ from solving (5.14) gives us the frequency-flat precoder $\mathbf{F}_{\text{ff}} = \mathbf{V}[\hat{k}]_{:,1:R}$, and the frequency-flat combiner $\mathbf{W}_{\text{ff}} = \mathbf{U}[\hat{k}]_{:,1:R}$. Using Algorithm 1, alternatively, gives us $\mathbf{F}_{\text{ff}} = \mathbf{V}_{M'}[\hat{k}]$ and $\mathbf{W}_{\text{ff}} = \mathbf{U}_{M'}[\hat{k}]$, directly.

5.6.2 With Extrinsic Mean of the Subspaces

In this proposed approach, we evaluate the right and left orthogonal vectors of each of the MIMO channel matrices corresponding to the different subcarriers separately and then compute the extrinsic mean of the estimated subspaces, which is then orthogonalized to derive the optimal frequency-flat precoder and combiner. The advantage of this approach is that all the measurements are utilized and the averaging operation results in noise reductions, thus results in better estimation error performance.

Formally, let $\mathbf{U}_{M'}[k]$ be the left semi-unitary matrix from Algorithm 1, and let $\mathbf{V}_{M'}[k]$ be the corresponding right semi-unitary matrix, for each subcarrier k. In

other words, $\mathbf{U}_{M'}[k]$ and $\mathbf{V}_{M'}[k]$ are the outputs from Algorithm 1 for the inputs $\mathbf{y}_{(1:M)}[k]$, $\mathbf{x}_{(1:M)}[k]$, $\mathbf{F}_{(1:M)}$ and $\mathbf{W}_{(1:M)}$. Let the extrinsic mean of the column space [99, 100] of $\{\mathbf{U}_{M'}[k]\}_{k=1,\cdots K}$ be denoted as $\mathcal{U}$, and denote the extrinsic mean of the column space of $\{\mathbf{V}_{M'}[k]\}_{k=1,\cdots K}$ as $\mathcal{V}$. Then the R-dimensional orthonormal bases of $\mathcal{U}$ are the columns of the frequency-flat combiner $\mathbf{W}_{\text{ff}}$, and the R-dimensional orthonormal bases of $\mathcal{V}$ are the columns of the frequency-flat precoder $\mathbf{F}_{\text{ff}}$. Note that the extrinsic subspace mean $\mathcal{U}$ can be easily found out as the R-dimensional eigenspace of $\frac{1}{K}\sum_{k=1}^{K}\mathbf{U}_{M'}[k]\mathbf{U}_{M'}^{*}[k]$ [100]. Similarly, the extrinsic subspace mean $\mathcal{V}$ can be evaluated as the R-dimensional eigenspace of $\frac{1}{K}\sum_{k=1}^{K}\mathbf{V}_{M'}[k]\mathbf{V}_{M'}^{*}[k]$.

Alternatively, we can solve (5.14) for each k and compute the left and right orthonormal matrices $\hat{\mathbf{U}}[k]$ and $\hat{\mathbf{V}}[k]$ corresponding to the estimated channel matrix $\hat{\mathbf{H}}[k]$. Then the orthonormal bases of the R-dimensional eigenspace of

$$\frac{1}{K}\sum_{k=1}^{K}\left(\left[\hat{\mathbf{U}}[k]\right]_{:,1:R}\right)\left(\left[\hat{\mathbf{U}}[k]\right]_{:,1:R}\right)^{*}$$

are the columns of $\mathbf{W}_{\text{ff}}$, and the orthonormal bases of the R-dimensional eigenspace of

$$\frac{1}{K}\sum_{k=1}^{K}\left(\left[\hat{\mathbf{V}}[k]\right]_{:,1:R}\right)\left(\left[\hat{\mathbf{V}}[k]\right]_{:,1:R}\right)^{*}$$

are the columns of $\mathbf{F}_{\text{ff}}$.

Note that though we assume extrinsic subspace mean for this proposed approach, other subspace means [99] may also be used to derive the orthonormal columns of the frequency-flat precoder and combiner. Our choice of using extrinsic mean is due to the ease of computing it analytically, rather than through an iterative algorithm needed for computing other subspace means.

5.6.3 Via MIMO Channel Stacking

Given that all the MIMO channel matrices corresponding to different subcarriers have the same column space, in this proposed approach, we stack all the measurements column-wise and resulting unknown matrix is still low rank (row rank). Applying Algorithm 1 to this effective unknown matrix directly gives the orthogonal vectors that span the column space of all the channel matrices. In other words, the resulting vectors constitute the ideal frequency-flat combiner.

To elaborate, define $\mathbf{H}_{\text{fat}} = [\mathbf{H}[1] \mid \mathbf{H}[2] \mid \cdots \mid \mathbf{H}[K]]$, obtained by stacking the channel matrices column-wise. With $\mathbf{0}_m$ denoting an all-zero vector of length m, we can rewrite (5.13) in terms of $\mathbf{H}_{\text{fat}}$ as follows:

$$\mathbf{y}_{(m)}[k] = \mathbf{W}_{(m)}^{*}\mathbf{H}_{\text{fat}} \begin{bmatrix} \mathbf{0}_{(k-1)N_{\text{t}}} \\ \mathbf{F}_{(m)}\mathbf{x}_{(m)}[k] \\ \mathbf{0}_{(K-k)N_{\text{t}}} \end{bmatrix} + \mathbf{W}_{(m)}^{*}\mathbf{n}[k]. \tag{5.16}$$

Let $\mathbf{F}_{(m)}^{\text{fat}}(\mathbf{x}) \in \mathcal{C}^{KN_{\text{t}} \times K}$ denote a block diagonal matrix with the kth block diagonal entry equal to $\mathbf{F}_{(m)}\mathbf{x}_{(m)}[k]$. Denote the effective combiner matrix obtaining by repeating the frequency-flat combiner column-wise K times, as $\mathbf{W}_{(m)}^{\text{fat}} \in \mathcal{C}^{N_{\text{r}} \times KN_{\text{r}}}$. Then, stacking (5.16) for each k leads to

$$\mathbf{y}_{(m)}^{\text{eff}} = \begin{bmatrix} \mathbf{y}_{(m)}[1] \\ \mathbf{y}_{(m)}[2] \\ \vdots \\ \mathbf{y}_{(m)}[K] \end{bmatrix} = \mathbf{W}_{(m)}^{\text{fat}\ *}\mathbf{H}_{\text{fat}}\text{vec}\left(\mathbf{F}_{(m)}^{\text{fat}}(\mathbf{x})\right) + \begin{bmatrix} \mathbf{W}_{(m)}^{*}\mathbf{n}[1] \\ \mathbf{W}_{(m)}^{*}\mathbf{n}[2] \\ \vdots \\ \mathbf{W}_{(m)}^{*}\mathbf{n}[K] \end{bmatrix}. \tag{5.17}$$

Note that the column space of $\mathbf{H}_{\text{fat}}$ is the same as the column-space of $\mathbf{H}[k]$, $\forall\ k$. Therefore, applying Algorithm 1 with inputs $\mathbf{y}_{(1:M)}^{\text{eff}}$, $\mathbf{x}_{(1:M)} \equiv 1$, vec $\left(\mathbf{F}_{(1:M)}^{\text{fat}}(\mathbf{x})\right)$ and $\mathbf{W}_{(1:M)}^{\text{fat}}$ gives the left semi-unitary matrix $\mathbf{U}_{M'}$ whose first N_{s} columns constitute the columns of the frequency-flat combiner $\mathbf{W}_{\text{ff}}$.

For estimating the right semi-unitary matrix of the MIMO channel matrices, we assume $\mathbf{x}_{(m)}[k] = \mathbf{x}_{(m)}$ and stack the measurements row-wise as follows. First, let

$$\mathbf{H}_{\text{tall}} = \begin{bmatrix} \mathbf{H}[1] \\ \mathbf{H}[2] \\ \vdots \\ \mathbf{H}[K] \end{bmatrix} \in \mathcal{C}^{KN_{\text{r}} \times N_{\text{t}}} \tag{5.18}$$

denote the effective channel matrix obtained by stacking the MIMO channel matrices row-wise. With $\mathbf{O}_{m\times n}$ denoting the all-zero matrix of dimension $m \times n$, (5.13) in terms of $\mathbf{H}_{\text{tall}}$ is

$$\mathbf{y}_{(m)}[k] = \left[\mathbf{O}_{N_{\text{s}}\times(k-1)N_{\text{r}}}\ \mathbf{W}^{*}_{(m)}\ \mathbf{O}_{N_{\text{s}}\times(K-k)N_{\text{r}}}\right] \mathbf{H}_{\text{tall}}\mathbf{F}_{(m)}\mathbf{x}_{(m)} + \mathbf{W}^{*}_{(m)}\mathbf{n}[k]. \tag{5.19}$$

Then with $\mathbf{I}_n$ denoting the identity matrix of size n, we define $\mathbf{W}^{\text{tall}}_{(m)} = \mathbf{I}_K \otimes \mathbf{W}_{(m)}$, so that stacking (5.19) for each k gives us

$$\mathbf{y}^{\text{eff}}_{(m)} = \mathbf{W}^{\text{tall}\,*}_{(m)}\mathbf{H}_{\text{tall}}\mathbf{F}_{(m)}\mathbf{x}_{(m)} + \begin{bmatrix} \mathbf{W}^{*}_{(m)}\mathbf{n}[1] \\ \mathbf{W}^{*}_{(m)}\mathbf{n}[2] \\ \vdots \\ \mathbf{W}^{*}_{(m)}\mathbf{n}[K] \end{bmatrix}. \tag{5.20}$$

Since the row-space of $\mathbf{H}_{\text{tall}}$ is the same as the row-space of $\mathbf{H}[k]$, $\forall\ k$, applying Algorithm 1 with inputs $\mathbf{y}^{\text{eff}}_{(1:M)}$, $\mathbf{x}_{(1:M)}$, $\mathbf{F}_{(1:M)}$ and $\mathbf{W}^{\text{tall}}_{(1:M)}$ gives the right semi-unitary matrix $\mathbf{V}_{M'}$ whose first N_{s} columns constitute the columns of the frequency-flat combiner $\mathbf{F}_{\text{ff}}$.

5.6.4 Empirical Covariance Estimation at the Transceivers

In this proposed approach, the receive subspace is estimated at the receiver during downlink training. Similarly, assuming channel reciprocity, estimating the

receive subspace during uplink training gives us the original transmit subspace of the intended downlink channel. This is unlike the previous proposed approaches in the paper, where both the subspaces are estimated at the (downlink) receiver after the end of the training.

In this section, we elaborate how the receive subspace can be estimated using the proposed approach during downlink training. The details about the transmit subspace estimation follows the same principle during uplink training and with channel reciprocity. During the mth training phase, the received signal before combining in the kth subcarrier is

$$\mathbf{r}_{(m)}[k] = \mathbf{H}[k]\mathbf{F}_{(m)}\mathbf{x}_{(m)}[k] + \mathbf{n}[k], \tag{5.21}$$

which using the expansion for $\mathbf{H}[k]$ in (5.5), and denoting the inner product of two vectors $\mathbf{a}$ and $\mathbf{b}$ as $\langle \mathbf{a}, \mathbf{b} \rangle = \mathbf{a}^*\mathbf{b}$, can be represented as

$$\mathbf{r}_{(m)}[k] = \mathbf{A}_{\mathrm{R}} \begin{bmatrix} [\mathbf{P}[k]]_{1,1} \left\langle \mathbf{a}_{\mathrm{T}}^*(\theta_1), \mathbf{F}_{(m)}\mathbf{x}_{(m)}[k] \right\rangle \\ [\mathbf{P}[k]]_{2,2} \left\langle \mathbf{a}_{\mathrm{T}}^*(\theta_2), \mathbf{F}_{(m)}\mathbf{x}_{(m)}[k] \right\rangle \\ \vdots \\ [\mathbf{P}[k]]_{R,R} \left\langle \mathbf{a}_{\mathrm{T}}^*(\theta_R), \mathbf{F}_{(m)}\mathbf{x}_{(m)}[k] \right\rangle \end{bmatrix} + \mathbf{n}[k]. \tag{5.22}$$

Since the path gains $\{\alpha_\ell\}$ are independently distributed and because

$$[\mathbf{P}[k]]_{\ell,\ell} = \sum_{d=0}^{N_{\mathrm{c}}-1} [\mathbf{P}_d]_{\ell,\ell} \, e^{-\mathrm{j}\frac{2\pi k d}{K}} \tag{5.23}$$

$$= \sum_{d=0}^{N_{\mathrm{c}}-1} \alpha_\ell p(dT_{\mathrm{s}} - \tau_\ell) e^{-\mathrm{j}\frac{2\pi k d}{K}}, \tag{5.24}$$

we have that $\left\{ [\mathbf{P}[k]]_{\ell,\ell} \right\}$ are independently distributed. Therefore, the covariance $\mathbf{C}_{\mathbf{r},\mathbf{r}}[k]$ of $\mathbf{r}_{(m)}[k]$ is

$$\mathbf{C}_{\mathbf{r},\mathbf{r}}[k] = \mathbf{A}_{\mathrm{R}} \mathbf{\Sigma}[k] \, \mathbf{A}_{\mathrm{R}}{}^* + \sigma^2 \mathbf{I}, \tag{5.25}$$

where $\mathbf{\Sigma}[k] \in \mathbb{R}_{+}^{R\times R}$ is a diagonal matrix with the ℓth entry

$$[\mathbf{\Sigma}[k]]_{\ell,\ell} = \left|[\mathbf{P}[k]]_{\ell,\ell}\right|^2 \left|\left\langle \mathbf{a}_{\mathrm{T}}^{*}(\theta_\ell), \mathbf{F}_{(m)}\mathbf{x}_{(m)}[k]\right\rangle\right|^2. \tag{5.26}$$

The received signal post combining is $\mathbf{y}_{(m)}[k] = \mathbf{W}_{(m)}^{*}\mathbf{r}_{(m)}[k]$. The covariance of the post combined signal $\mathbf{y}_{(m)}[k]$, therefore, is $\mathbf{C}_{\mathbf{y},\mathbf{y}}(m)[k] = \mathbf{W}_{(m)}^{*}\mathbf{C}_{\mathbf{r},\mathbf{r}}[k]\mathbf{W}_{(m)}$. From this, the averaged empirical covariance $\tilde{\mathbf{C}}_{\mathbf{y},\mathbf{y}}(m)$ of the post combiner received signal

$$\tilde{\mathbf{C}}_{\mathbf{y},\mathbf{y}}(m) = \frac{1}{K}\sum_{k=1}^{K}\mathbf{y}_{(m)}[k]\,\mathbf{y}_{(m)}^{*}[k] \tag{5.27}$$

can be used to estimate the receive subspace $\mathcal{H}_c$, noting that fact that the column space of $\mathbf{C}_{\mathbf{y},\mathbf{y}}(m)[k]$ is a subspace of $\mathcal{H}_c$, neglecting noise and when Proposition 6 holds. Hence the receive subspace estimation problem can be solved by the following optimization problem, with $\mathbf{C}_{\mathbf{r},\mathbf{r}}$ denoting the variable of optimization:

$$\begin{aligned} &\min_{\mathbf{C}_{\mathbf{r},\mathbf{r}}\in\mathbb{C}^{N_{\mathrm{r}}\times N_{\mathrm{r}}}} \quad \|\mathbf{C}_{\mathbf{r},\mathbf{r}}\|_{*} \\ &\text{s.t. } \|\mathbf{W}_{(m)}^{*}\mathbf{C}_{\mathbf{r},\mathbf{r}}\mathbf{W}_{(m)} - \tilde{\mathbf{C}}_{\mathbf{y},\mathbf{y}}(m)\|_{F} \le \epsilon \quad \text{for } m=1,2,\cdots,M. \end{aligned} \tag{5.28}$$

The left singular vectors of the optimum $\hat{\mathbf{C}}_{\mathbf{r},\mathbf{r}}$, that solves (5.28), then span $\mathcal{H}_c$, and hence, are the columns of the optimum frequency-flat combiner $\mathbf{W}_{\mathrm{ff}}$.

Repeating the proposed empirical covariance approached in the uplink, and assuming channel reciprocity, we could also get the optimum frequency-flat precoder $\mathbf{F}_{\mathrm{ff}}$.

5.7 Simulation Results

In this section, we present simulation results to illustrate the optimality of the proposed frequency precoder and combiner proposed in Section 5.4. We assume a uni-

form linear array with half wavelength antenna element separation at the transceivers, a frequency-selective mmWave MIMO channel with $N_{\mathrm{c}} = 16$ channel taps, and an OFDM system with $K = 64$ subcarriers for the simulations.

The metric used to evaluate the optimality of the proposed procoders and combiners is the normalized energy Υ forced into the dominant subspaces when using the optimal frequency-flat precoder and combiner. This energy can be computed as $\Upsilon = \frac{1}{K} \sum_{k=1}^{K} \gamma_k$, with

$$\gamma_k = \frac{\|\mathbf{W}_{\mathrm{ff}}^{*} \mathbf{H}[k] \mathbf{F}_{\mathrm{ff}}\|_F^2}{\|\mathbf{H}[k]\|_F^2}. \tag{5.29}$$

Fig. 5.1 shows the optimality metric against the number of paths R in the frequency-selective MIMO channel, for various values of N_{r} and N_{t}. The rank of the channel matrices is upper bounded by $\min(R, N_{\mathrm{r}}, N_{\mathrm{t}})$. When the number of paths R is small compared to the number of transmit and receive antennas, from (5.5), the rank of each of the MIMO channel matrices is at most R. In this case, the proposed frequency-flat precoder and combiner are optimal. When $R > \min(N_{\mathrm{r}}, N_{\mathrm{t}})$, the semi-unitary precoding-combining solution is sub-optimum, as seen from Fig. 5.1. Note, however, that when the MIMO channel is full rank and $N_{\mathrm{r}} = N_{\mathrm{t}}$, unitary precoding and combining give optimum rate [80].

In Fig. 5.2, we plot the achievable rate using the proposed frequency-flat precoder and combiner as a function of the number of paths R for SNR = 0dB, $N_{\mathrm{t}} = 64$ and $N_{\mathrm{r}} = 16$. Fig. 5.2 also shows achievable rates with the conventional frequency-selective precoder and combiner, with and without water-filling. The plots in Fig. 5.2 show that when the MIMO channel rank equals the number of paths $R \leq \min(N_{\mathrm{r}}, N_{\mathrm{t}})$,

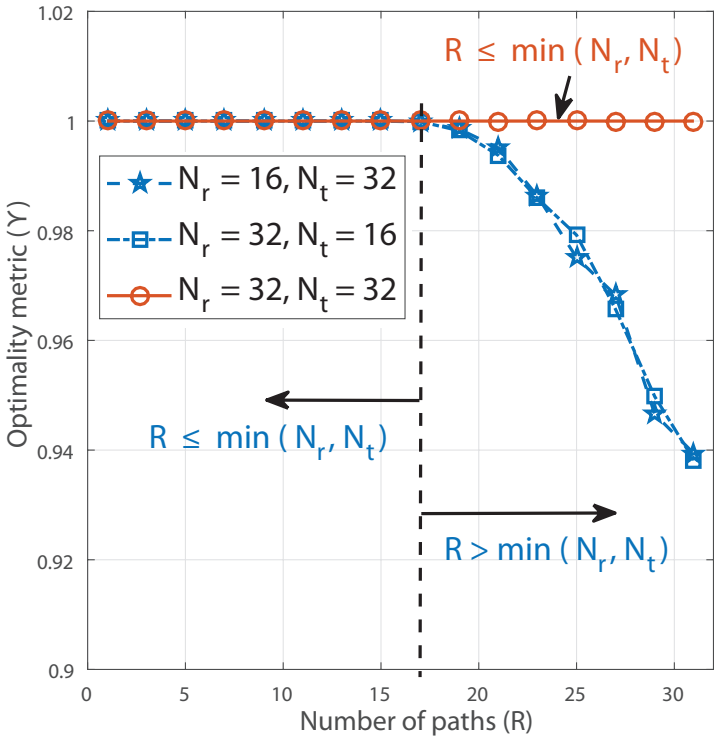

Figure 5.1: Optimality metric Υ, as a function of the number of paths R. The frequency-flat precoder, combiner is optimal when the number of paths R is small in comparison to $\min(N_{\mathrm{r}}, N_{\mathrm{t}})$.

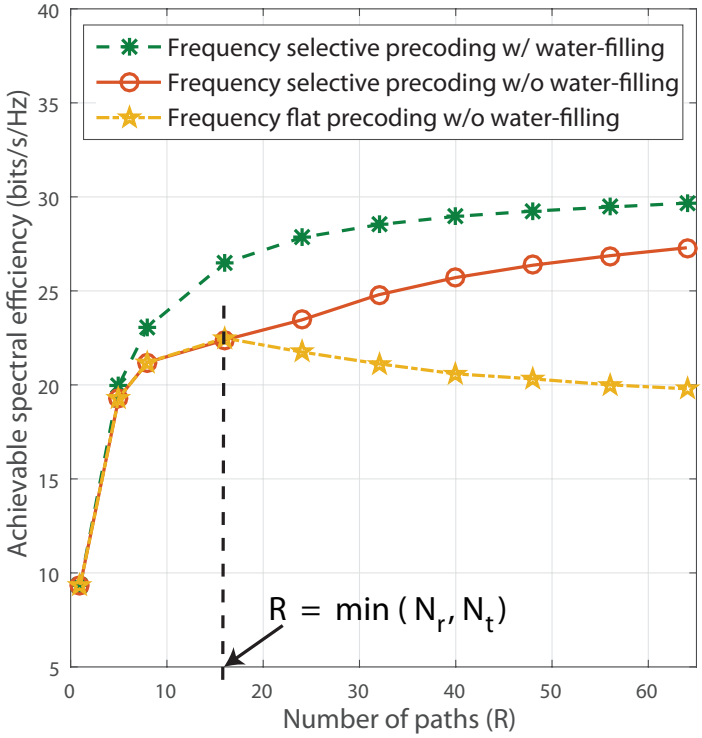

Figure 5.2: Plot showing the achievable spectral efficiency with the proposed frequency-flat precoder and combiner versus the number of paths R. The achievable rates with frequency-selective precoder-combiner are also plotted in the figure to show that the proposed frequency-flat precoding-combining strategy gives optimum achievable spectral efficiency when $R \leq \min(N_{\mathrm{r}}, N_{\mathrm{t}})$.

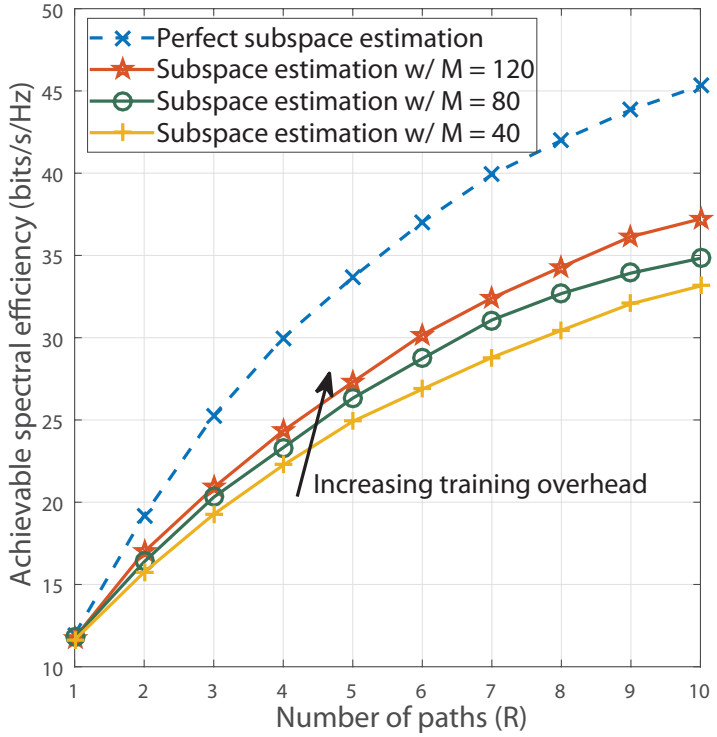

Figure 5.3: Plot showing the achievable spectral efficiency for SNR = 10dB with the compressive subspace estimation algorithm as a function of the number of paths R for various training lengths M.

then the frequency-flat precoder-combiner achieves the same rate as the SVD-based frequency-selective precoder-combiner. This implies that the system design and implementation is simplified in low-rank, large dimensional frequency-selective MIMO channels that are common in wideband mmWave systems.

In Fig. 5.3, we compare the achievable spectral efficiency provided by the frequency-flat precoders and combiners designed from compressive subspace estimation outlined in Section 5.6, as a function of the number of paths R, for various

training length M. We assume $N_{\mathrm{r}} = N_{\mathrm{t}} = 32$ here. When the number of paths is small, subspace recovery tools requiring small number of compressive measurements can be used to design the frequency-flat precoders and combiners. In this case, the loss in performance relative to the optimal frequency-flat precoders and combiners (assuming perfect channel knowledge) is also small. When the rank of the channel (which depends on the number of paths) is higher, a larger number of measurements is needed to obtain a good estimation of the subspaces and design the proposed frequency-flat precoders and combiners.

The hardware limitations in mmWave systems make the use of fully digital precoders and combiners impractical [55]. These place constraints on the frequency-selective hybrid precoder-combiner design as well. Nevertheless, efficient designs of frequency-selective hybrid precoder-combiner guarantee achievable rates similar to all-digital systems [80]. The proposed frequency-flat optimal precoder-combiner in this paper, can however, be implemented in the RF part of the transceiver architecture with additional constraints incorporating the limited resolution of phase shifters [86]. This not only makes the system design easier, but also makes the hardware implementation cost effective.

5.8 Conclusion

In this chapter, we established the optimality of the frequency-flat precoder-combiner for frequency-selective wideband mmWave channel with small number of paths. We proved that all the MIMO channel matrices corresponding to the time-domain delay taps, and all the subcarriers in the frequency-domain, have the same

row space and the column space. The combiners and precoders derived from these subspaces were shown to form optimal frequency-selective combiners and precoders when the MIMO channel dimensions are large in comparison with the rank of the channel, that is a function of the number of paths.

Chapter 6

Concluding Remarks

6.1 Summary

This dissertation presents the results of the study on the potential of mmWave frequencies for supporting high data rates among wearable devices. The key advantages and challenges of using mmWave-based device-to-device communication were identified. First, we developed an analytic model to evaluate expected coverage and rate performances given by finite mmWave wearable networks. Then, we proposed to model the impact of reflections and self-blocking which result in non-isotropic performance in indoor wearable operation. While the analytic framework assumed that the channel is already known and the transmitter is pointed correctly to the intended on-body receiver, explicit algorithms to enable MIMO channel estimation in wideband and frequency-selective mmWave channels were addressed in the later part of this dissertation. Finally, low-complexity, easy to implement precoding and combining solutions were proposed to support multi-stream communication between mmWave wearable devices.

While modeling finite mmWave-based communication networks, we incorporated the impact of human body blockages that are the major source of blockages in wearable applications. This framework is general and works for arbitrary distance-

dependent parameters and any Gamma-distributed small scale fading for a given network geometry. Techniques to ascertain whether an interfering device is blocked or not were also developed. We also proposed a tractable model for parameterizing 3-D antenna gain pattern of a uniform planar array of size N. The performance evaluation using the developed analytic framework showed the impact of N relative to the density of interfering devices. It was also proved via simulations that the derived closed-form expressions for coverage and ergodic rate closely predicts the actual system performance in a device-to-device link between a user's wearable devices in the presence of a finite number of nearby interfering users.

For understanding the impact of reflecting objects during an indoor operation of wearable networks, we developed a tractable model that quantified the connection between user location and orientation. Here we included a 3-D model with reflections from ceiling and the walls accounted for. Leveraging the elevation beamwidth of compact antennas used in mmWave wearables, we studied how the relative positioning of the transmitted and the receiver impacted the expected achievable rate performance. By modeling reflected signals as those emanating from phantom interferers located at the mirror image locations of the actual interferers, we proposed a method to quantify users as strong and weak sources of interference. In this part, we also developed a stochastic model to study self-blockage during mmWave wearables operation. Results showed the non-isotropy in performance when mmWave wearable networks are operated in indoor environment and the necessity of pointing the transceiver beams in the the correct direction to maximize SINR.

We developed channel estimation techniques to enable accurate pointing of

mmWave beams for wideband and frequency-selective mmWave systems. Here the hardware constraints in the system were modeled and the channel estimation problem was formulated as a sparse recovery problem in both time and frequency domain. We showed how various parameters in the system affected the channel estimation performance. Compared to conventional beam training approaches, we showed that the proposed compressive sensing based channel estimation techniques had fewer overheads. Furthermore, the knowledge of the completer MIMO channel enables design of efficient precoders and combiners that achieve multi-stream communication and rates similar to all-digital systems.

For low-rank frequency-selective hybrid MIMO mmWave systems, we proved that frequency-flat precoders and combiners are optimal. This means that low-complexity and easy to implement precoders and combiners can be designed for mmWave systems. This is especially promising for hardware-constrained mmWave wearable communication networks. We showed that in such a scenario subspace estimation techniques can be used for designing the precoders and combiners. We proposed several algorithms to perform subspace estimation that leveraged the fact that the MIMO channel matrices of all the subcarriers have the same rowspace and column space. For frequency-selective channels, we proposed OFDM-based hybrid precoding and codebook designs. We also examined the conditions under which the proposed frequency-flat beamformers are optimal.

6.2 Future Work

This dissertation only addressed some of the critical and initial aspects to enable mmWave-based high data rate requiring mmWave wearable networks. The following are a few research directions that need to be explored in the future. These also include some of the practical and general challenges that need to be considered before mmWave wearable devices become a reality.

Health Concerns Before mmWave devices are introduced in the consumer market of wearables, their compliance to radiation exposure guidelines as set out by the governing agencies has to be ensured. The sensitivity of human eye tissues and skin to mmWave frequencies needs to be analyzed more carefully before large scale deployment of mmWave devices, because high-intensity direct exposure of mmWave frequencies could cause ocular injury.

The preferred metric to determine compliance for devices operating at higher carrier frequencies is power density rather than specific absorption rate [101]. Given that the wearable devices would be held close to the body, reliable power density measurements are hard to obtain since the resulting electromagnetic fields are near-field. For distances less than 5 cm between devices and the human body, analytic tools may be used to compute power density numerically. Temperature elevation measurements are yet another way to evaluate compliance on mmWave devices [102, 103]. It was noted in [102] that longer, low-intensity exposure to mmWave signals, for example, 10 mW/cm^2 for upto 8 hours, appears to be safe. Further studies are needed with actual mmWave-based wearable devices to understand both long time and short term impacts.

Circuits The higher carrier frequencies and higher bandwidths pose several challenges for the design of RF circuits, mixed signal components, and the digital baseband. The high dielectric constant of most of the semi-conductors used today can result in a dielectric waveguiding effect depending on the size of the substrate. This could lead to energy loss for chip components or energy radiation in undesired directions [104] at mmWave frequencies. The leaked energy could even result in parasitic coupling between on-chip components. This poses problems for modeling transistors and passive devices, and requires careful treatment of small parasitic components within the model.

Another design challenge is to develop linear RF power amplifier which is a key ingredient to meet link budget of mmWave systems. These power amplifiers would need to operate at low-voltage supplies of the current semi-conductor technology while providing large dynamic ranges required for certain modulations [105].

The analog-to-digital converters (ADCs) can be a significant source of power consumption due to the wide bandwidth of the signals that need to be sampled. The issue is compounded with the use of many antennas. Potential solutions including analog, hybrid analog/digital, and low resolution ADCs are described in the next section. Commercial products based on mmWave systems such as the IEEE 802.11ad and WirelessHD are already available in the market today in high volume consumer applications. Hence, significant progress is being made on addressing these challenges.

Propagation Modeling MmWave propagation in the 60 GHz band is well understood, due to past work for IEEE 802.15.3c [40] and IEEE 802.11ad [11]. Most work though was done with different use cases in mind, especially in cable replace-

ment.

Blockage is a significant issue for mmWave in general, and specifically for wearable networks. The inadvertent movement the user's hands, for example, could occlude the on-body transmitter - receiver direct signal link in a wearable network. The blockage of signal due to the placement of fingers over the antenna arrays is yet another modeling challenge. The accurate variation in the propagation environment is difficult to model without detailed measurement data for such cases. Both ray-tracing and measurement-based studies have been used previously to study mmWave propagation in indoor environments [54, 106–108]. These, however, do not include several number of human users in the measurement chamber. These would also shed valuable insights regarding antenna placement and space optimization to ensure connectivity and minimize hand/body blockages for mmWave wearables.

Extension to lower-resolution A/D and D/A converters In Chapter 4, we proposed wideband mmWave channel estimation assuming hybrid architecture at the transceivers. The mixed signal components, A/D and D/A converters are still a major source of power consumption. Therefore, extension of the proposed techniques to the low-resolution mixed signal components are important for power-constrained wearable applications. This is non-trivial, though, since we are dealing with a wideband system with other hardware constrains that restrict our baseband measurements. Therefore, it would be interesting to examine this problem carefully inspired from prior work on narrowband systems.

Synchronization and offset correction In this dissertation, we assumed that the communication system is fully synchronized. In practice, however, synchro-

nization phase has to be performed before data transmission. It would be interesting to study synchronization techniques using hybrid architecture and low-resolution mixed-signal components for wideband mmWave systems. These could include both frequency and timing offset estimation and correction. It would be interesting to explore further the robustness of these algorithms in a highly interference limited regime, such as those in a crowded mmWave wearable network operation.

Appendices

Appendix A

Proof of Lemmas and Theorems

A.1 Proof of Lemma 2

The probability that user i blocks $\mathsf{R}_0 - \mathsf{T}_i$ link is the same as the probability that $\mathsf{R}_0^{\mathcal{P}} - \mathsf{T}_i$ link is blocked by B_i in $\mathcal{P}$. Since T_i is assumed to be located uniformly at random in a radius-d circle around B_i (same as B_i being located randomly around T_i in a radius-d circle), the probability that B_i blocks T_i link is

$$p_{\mathsf{b}}^{\text{self}} = \frac{1}{\pi} \arcsin\left(\frac{W}{2d}\right). \tag{A.1}$$

An illustration explaining the derivation of $p_{\mathsf{b}}^{\text{self}}$ is shown in Fig. A.1.

The probability that T_i falls in the blocking cone of B_0 is also $p_{\mathsf{b}}^{\text{self}}$ as $\mathcal{B}\left(\mathsf{R}_0^{\mathcal{P}}, r_{\mathsf{B}}(\mathsf{R}_0^{\mathcal{P}})\right)$ is circular with R_0 located at its center. So, the probability that both B_0 and B_i blocks

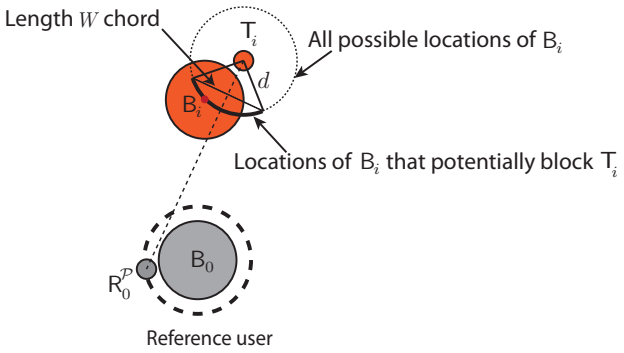

Figure A.1: Illustration of self-blockage of $\mathsf{R}_0 - \mathsf{T}_i$ link due to B_i.

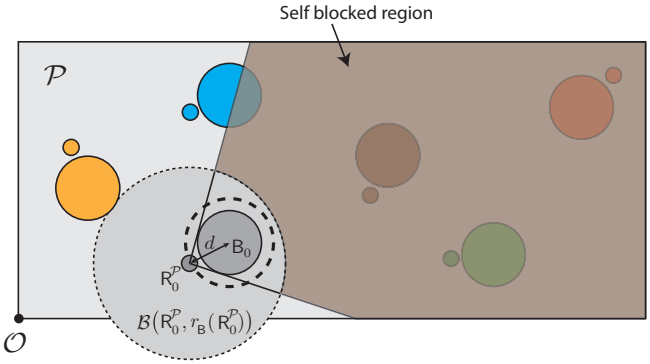

Figure A.2: Illustration showing the (shaded) region where weak interferers are self-blocked by B_0

T_i's interference is $p_2 = \left(p_{\mathsf{b}}^{\text{self}}\right)^2$, and the probability that neither user bodies block the interference is $p_0 = (1 - p_{\mathsf{b}}^{\text{self}})^2$. Finally, p_1 can be computed to satisfy $\sum_{s=0}^{2} p_s = 1$.

To evaluate $q(\mathsf{R}_0, \psi_0)$ in the second part of the Lemma, we use the illustration shown in Fig. A.2 which depicts the region in $\mathcal{P} \setminus \mathcal{B}\left(\mathsf{R}_0^{\mathcal{P}}, r_{\mathsf{B}}(\mathsf{R}_0^{\mathcal{P}})\right)$ that is blocked due to B_0. The probability that T_i is in this region (denoted as $\mathcal{BC}(\mathsf{B}_0) \setminus \mathcal{B}\left(\mathsf{R}_0^{\mathcal{P}}, r_{\mathsf{B}}(\mathsf{R}_0^{\mathcal{P}})\right)$) is $q_1(\mathsf{R}_0, \psi_0)$ given in Lemma 2. The probability that B_i blocks T_i is still $p_{\mathsf{b}}^{\text{self}}$ since it only depends on $\psi_i = \measuredangle\left(\psi_i - \mathsf{B}_i\right)$ that is uniformly random in $[0, 2\pi]$ (cf Fig. A.1). So the probability that both the weak interferer T_i and z_0 are facing each other is

$$q(\mathsf{R}_0, \psi_0) \;=\; \left(1 - p_{\mathsf{b}}^{\text{self}}\right)\left(1 - q_1(\mathsf{R}_0, \psi_0)\right). \tag{A.2}$$

A.2 Proof of Lemma 3

The interferers T_i such that $\measuredangle\mathsf{T}_i \in \left[\phi_0^{(\mathsf{a})} - \frac{\theta_{\mathsf{r}}^{(\mathsf{a})}}{2}, \phi_0^{(\mathsf{a})} + \frac{\theta_{\mathsf{r}}^{(\mathsf{a})}}{2}\right]$ fall within the receiver main-lobe in the azimuth. Since the strong interferers are assumed to be uniformly and isotropically distributed in $\mathcal{B}\left(\mathsf{R}_0^{\mathcal{P}}, r_{\mathsf{B}}(\mathsf{R}_0^{\mathcal{P}})\right)$, the probability that a strong

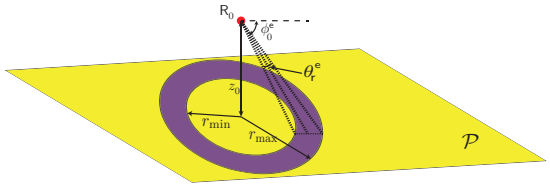

Figure A.3: Illustration showing the region in $\mathcal{P}$ that falls within the receiver main-lobe due to the elevation beam-width of the antenna.

interferer falls within azimuth beam-width of the reference receiver is $\frac{\theta_{\mathsf{r}}^{(\mathsf{a})}}{2\pi}$. Due to the non-isotropy of $\hat{\mathcal{P}} = \mathcal{P} \setminus \mathcal{B}\left(\mathsf{R}_0^{\mathcal{P}}, r_{\mathsf{B}}(\mathsf{R}_0^{\mathcal{P}})\right)$ with respect to the reference receiver, the probability that a weak interferer lies in the receiver main-lobe in the azimuth needs to be computed numerically (using the definition in (3.27)) and evaluates to $\frac{|\Upsilon(\phi_0^{(\mathsf{a})})|}{|\hat{\mathcal{P}}|}$.

The region in $\mathcal{P}$ falling within the elevation beam-width of R_0 depends not only on the receiver antenna beam-width $\theta_{\mathsf{r}}^{\mathsf{e}}$ but also on z_0. This is illustrated in Fig. A.3.

The region in $\mathcal{B}\left(\mathsf{R}_0^{\mathcal{P}}, r_{\mathsf{B}}(\mathsf{R}_0^{\mathcal{P}})\right)$ that falls within the elevation beam-width of R_0 is an annulus with inner radius $r_{\min}$ and outer radius $\min\left(r_{\mathsf{B}}(\mathsf{R}_0^{\mathcal{P}}), r_{\max}\right)$. The ratio of area of this annulus to the area of $\mathcal{B}\left(\mathsf{R}_0^{\mathcal{P}}, r_{\mathsf{B}}(\mathsf{R}_0^{\mathcal{P}})\right)$ gives the probability that a strong interferer lies within the receiver antenna elevation beam-width. This evaluates to

$$\left(\frac{\min\left(r_{\mathsf{B}}(\mathsf{R}_0^{\mathcal{P}}), r_{\max}\right)^2 - r_{\min}^2}{r_{\mathsf{B}}^2(\mathsf{R}_0^{\mathcal{P}})}\right). \tag{A.3}$$

Similarly, the probability of being within the elevation beam-width of R_0 for weak interferers is computed as

$$\left(1 - \frac{|\mathcal{P} \setminus \mathcal{B}\left(\mathsf{R}_0^{\mathcal{P}}, \max(r_{\mathsf{B}}(\mathsf{R}_0^{\mathcal{P}}), r_{\mathsf{max}})\right)|}{|\mathcal{P} \setminus \mathcal{B}\left(\mathsf{R}_0^{\mathcal{P}}, r_{\mathsf{B}}(\mathsf{R}_0^{\mathcal{P}})\right)|}\right). \tag{A.4}$$

Finally, an interferer lies within the main-lobe of the reference receiver if its position in $\mathcal{P}$ falls within both the azimuth and the elevation beam-widths of $\mathsf{R}_0^{\mathcal{P}}$. This leads to the expressions for $p_{\text{rx}}^{\mathsf{SI}}$ and $p_{\text{rx}}^{\mathsf{WI}}$ given in Lemma 3.

A.3 Proof of Theorem 4

Suppose there are J number of strong interferers. Clearly, J is Poisson distributed with mean $\lambda|\mathcal{B}\left(\mathsf{R}_0^{\mathcal{P}}, r_{\mathsf{B}}(\mathsf{R}_0^{\mathcal{P}})\right)| = \lambda\pi r_{\mathsf{B}}^2(\mathsf{R}_0^{\mathcal{P}})$. With $\ell = \{\ell(\mathsf{R}_0, \mathsf{T}_i)\}_{i=1}^J$, $h = \{h_i\}_{i=1}^J$, $\tilde{G}_{\mathsf{t}} = \{G_{\mathsf{t},i}\}_{i=1}^J$ and $\tilde{G}_{\mathsf{r}} = \{G_{\mathsf{r},i}\}_{i=1}^J$,

$$\mathbb{E}_{\mathbf{\Phi}}\left[e^{-km\tilde{m}\tilde{\gamma}I_{\mathbf{\Phi}}^{\mathsf{SI}}}\right] = \mathbb{E}_J\left[\mathbb{E}_{\ell,h,\tilde{G}_{\mathsf{t}},\tilde{G}_{\mathsf{r}}}\left[\prod_{i=1}^J e^{-km\tilde{m}\tilde{\gamma}h_i\ell(\mathsf{R}_0,\mathsf{T}_i)G_{\mathsf{t},i}G_{\mathsf{r},i}}\right]\right]. \tag{A.5}$$

Since h are independent normalized gamma random variables, their moment generating functions can be used to evaluate the expectation with respect to h which leads to

$$\mathbb{E}_J\left[\mathbb{E}_{\ell,\tilde{G}_{\mathsf{t}},\tilde{G}_{\mathsf{r}}}\left[\prod_{i=1}^J (1 + k\tilde{m}\tilde{\gamma}\ell(\mathsf{R}_0, \mathsf{T}_i)G_{\mathsf{t},i}G_{\mathsf{r},i})^{-m}\right]\right]. \tag{A.6}$$

For strong interferers, $\ell(\mathsf{R}_0, \mathsf{T}_i) = \frac{\|\mathsf{R}_0 - \mathsf{T}_i\|^{-\alpha_{\mathsf{L}}}}{\mathsf{B}_{\mathsf{L}}^s}$, and $\{\mathsf{T}_i\}_{i=1}^J$ are uniformly and independently distributed in $\mathcal{B}\left(\mathsf{R}_0^{\mathcal{P}}, r_{\mathsf{B}}(\mathsf{R}_0^{\mathcal{P}})\right)$. The expectation with respect to ℓ can be evaluated in two steps - taking an expectation over the number of self body blockages s followed by averaging over $r_i = |\mathsf{R}_0^{\mathcal{P}} - \mathsf{T}_i|$ that has distribution

$$f_{r_i}(r) = \frac{2r}{r_{\mathsf{B}}^2(\mathsf{R}_0^{\mathcal{P}})}\ 0 \le r \le r_{\mathsf{B}}(\mathsf{R}_0^{\mathcal{P}}). \tag{A.7}$$

Using this observation and the distribution in (A.7), the expectation (A.6) with respect to ℓ evaluates to

$$\mathbb{E}_J\left[\mathbb{E}_{\tilde{G}_\mathsf{t},\tilde{G}_\mathsf{r}}\left[\prod_{i=1}^{J}\sum_{s=0}^{2}p_s\int_0^{r_\mathsf{B}(\mathsf{R}_0^\mathcal{P})}\left(1+\frac{k\tilde{m}\tilde{\gamma}G_{\mathsf{r},i}G_{\mathsf{t},i}}{(r^2+z_0^2)^{\frac{\alpha_\mathsf{L}}{2}}\,\mathsf{B}_\mathsf{L}^s}\right)^{-m}\frac{2r}{r_\mathsf{B}^2(\mathsf{R}_0^\mathcal{P})}\mathsf{d}r\right]\right]. \tag{A.8}$$

The reference receiver's antenna is pointed towards the reference transmitter, which by our assumption is not blocked by the reference user's body. This implies that the interference from all the strong interferers that fall in $\mathcal{BC}(\mathsf{B}_0)$ signals see a receiver gain of g_r at R_0. The receiver gain at R_0 for the strong interferers outside $\mathcal{BC}(\mathsf{B}_0)$ is either G_r with probability $p_{\mathrm{rx}}^{\mathsf{SI}}$ or g_r with probability $1-p_{\mathrm{rx}}^{\mathsf{SI}}$. Using this observation and the notation,

$$\mathcal{F}(a,s)=\int_0^{r_\mathsf{B}(\mathsf{R}_0^\mathcal{P})}\left(1+\frac{k\tilde{m}\tilde{\gamma}aG_{\mathsf{t},i}}{(r^2+z_0^2)^{\frac{\alpha_\mathsf{L}}{2}}\,\mathsf{B}_\mathsf{L}^s}\right)^{-m}\frac{2r}{r_\mathsf{B}^2(\mathsf{R}_0^\mathcal{P})}\mathsf{d}r,$$

the expectation with respect to $\tilde{G}_\mathsf{r}$ in (A.8) evaluates to

$$\mathbb{E}_J\left[\mathbb{E}_{\tilde{G}_\mathsf{t}}\left[p_0\left(p_{\mathrm{rx}}^{\mathsf{SI}}\mathcal{F}(G_\mathsf{r},0)+(1-p_{\mathrm{rx}}^{\mathsf{SI}})\mathcal{F}(g_\mathsf{r},0)\right)+\frac{p_1}{2}\left(p_{\mathrm{rx}}^{\mathsf{SI}}\mathcal{F}(G_\mathsf{r},1)+(1-p_{\mathrm{rx}}^{\mathsf{SI}})\mathcal{F}(g_\mathsf{r},1)\right)\right.\right.$$
$$\left.\left.+\frac{p_1}{2}\mathcal{F}(g_\mathsf{r},1)+p_2\mathcal{F}(g_\mathsf{r},2)\right]^J\right] \tag{A.9}$$

Averaging over the random distribution of $\tilde{G}_\mathsf{t}$, (A.9) results in (A.10) which uses the notation in (3.32).

$$\mathbb{E}_J\left[p_0\sum_{j=1}^{4}\mu_j\left(1-\frac{2}{r_\mathsf{B}^2(\mathsf{R}_0^\mathcal{P})}A_{j,0}\right)+\frac{p_1}{2}\sum_{j=1}^{4}\mu_j\left(1-\frac{2}{r_\mathsf{B}^2(\mathsf{R}_0^\mathcal{P})}A_{j,1}\right)\right.$$
$$\left.+\frac{p_1}{2\,(1-p_{\mathrm{rx}}^{\mathsf{SI}})}\sum_{j=3}^{4}\mu_j\left(1-\frac{2}{r_\mathsf{B}^2(\mathsf{R}_0^\mathcal{P})}A_{j,1}\right)+\frac{p_2}{(1-p_{\mathrm{rx}}^{\mathsf{SI}})}\sum_{j=3}^{4}\mu_j\left(1-\frac{2}{r_\mathsf{B}^2(\mathsf{R}_0^\mathcal{P})}A_{j,2}\right)\right]^J \tag{A.10}$$

Finally, taking the expectation in (A.10) with respect to Poisson distributed J results in the expression in (3.33).

A.4 Proof of Theorem 5

We use the notations $\ell = \{\ell(\mathsf{R}_0, \mathsf{T}_i)\}_{i=1}^K$, $h = \{h_i\}_{i=1}^K$, $\tilde{G}_\mathsf{t} = \{G_{\mathsf{t},i}\}_{i=1}^K$ and $\tilde{G}_\mathsf{r} = \{G_{\mathsf{r},i}\}_{i=1}^K$. For simplicity, we use q to denote $q(\mathsf{R}_0, \psi_0)$ here. Noting that the number of weak interferers K is a Poisson distributed random variable with mean $\lambda|\hat{\mathcal{P}}|$, we have $\mathbb{E}_{\mathbf{\Phi}}\left[e^{-km\tilde{m}\tilde{\gamma}I_{\mathbf{\Phi}}^{\mathsf{WI}}}\right]$

$$
\begin{aligned}
&= \mathbb{E}_K\left[\mathbb{E}_{\ell,h,\tilde{G}_\mathsf{t},\tilde{G}_\mathsf{r}}\left[\prod_{i=1}^K e^{-km\tilde{m}\tilde{\gamma}h_i\ell(\mathsf{R}_0,\mathsf{T}_i)G_{\mathsf{t},i}G_{\mathsf{r},i}}\right]\right] && \text{(A.11)}\\
&= \mathbb{E}_K\left[\mathbb{E}_{\tilde{G}_\mathsf{r},\ell}\left[\prod_{i=1}^K \Big(p_\mathsf{M}\left(1+k\tilde{m}\tilde{\gamma}\ell(\mathsf{R}_0,\mathsf{T}_i)G_\mathsf{t}G_{\mathsf{r},i}\right)^{-m}\right.\right.\\
&\qquad \left.\left.+\left(1-p_\mathsf{M}\right)\left(1+k\tilde{m}\tilde{\gamma}\ell(\mathsf{R}_0,\mathsf{T}_i)g_\mathsf{t}G_{\mathsf{r},i}\right)^{-m}\Big)\right]\right], && \text{(A.12)}
\end{aligned}
$$

where we used the IID property of h and $\tilde{G}_\mathsf{t}$. Given K, $\{\mathsf{T}_i\}_{i=1}^K$ are uniformly distributed in $\hat{\mathcal{P}}$ and the probability of self-blockage is as per Lemma 2. Using the notations

$$
\begin{aligned}
\mathcal{D}(a,b) &= \frac{1}{|\hat{\mathcal{P}}|}\int_{z\in\hat{\mathcal{P}}}\left(1+\frac{k\tilde{m}\tilde{\gamma}aG_{\mathsf{r},i}}{b}\right)^{-m}\mathrm{d}z, && \text{(A.13)}\\
b_1 &= \|\mathsf{R}_0 - z\|_c^{\alpha_\mathsf{L}} \text{ and} && \text{(A.14)}\\
b_2 &= \|\mathsf{R}_0 - z\|^{\alpha_\mathsf{N}}, && \text{(A.15)}
\end{aligned}
$$

the expectation of (A.12) with respect to ℓ evaluates to

$$
\begin{aligned}
&\mathbb{E}_K\mathbb{E}_{\tilde{G}_\mathsf{r}}\left[\prod_{i=1}^K\left(q\left[p_\mathsf{M}\mathcal{D}(G_\mathsf{t},b_1)+(1-p_\mathsf{M})\mathcal{D}(g_\mathsf{t},b_1)\right]\right.\right.\\
&\left.\left.+(1-q)\left[p_\mathsf{M}\mathcal{D}(G_\mathsf{t},b_2)+(1-p_\mathsf{M})\mathcal{D}(g_\mathsf{t},b_2)\right]\right)\right]. && \text{(A.16)}
\end{aligned}
$$

This follows directly using the path-loss model as defined in (3.15). The orientation of the reference receiver's antenna is such that the interferers falling in $\mathcal{BC}(\mathsf{B}_0)$ always see the side-lobe gain. Using this fact, with $p_{\text{rx}}^{\mathsf{WI}}$ defined in Lemma 3 and with the notations in (3.30), (3.31), we can evaluate the expectation with respect to $\tilde{G}_{\mathsf{r}}$ to simplify (A.16) as

$$\mathbb{E}_K \left[\frac{q}{|\hat{\mathcal{P}}|} \left(|\hat{\mathcal{P}}| - C_1 \right) + \frac{1-q}{|\hat{\mathcal{P}}|} \left(|\hat{\mathcal{P}}| - C_2 \right) \right]^K . \tag{A.17}$$

Taking the expectation of (A.17) with respect to Poisson distributed K leads to the expressions in Theorem 5.

Bibliography

[1] K. Venugopal, M. Valenti, and R. Heath, "Interference in finite-sized highly dense millimeter wave networks," in *Proc. IEEE Inform. Theory and Applicat. Workshop (ITA)*, pp. 175–180, Feb. 2015.

[2] R. T. Llamas, "Worldwide wearable computing device 2014-2018 update: December 2014." [Online] Available: `http://www.idc.com/getdoc.jsp?containerId=253091`.

[3] "Wearable technology 2015-2025: Technologies, markets, forecasts." `http://www.idtechex.com/research/reports/wearable-technology-2015-2025-technologies-markets-forecasts-000427.asp`, May 2015.

[4] D. Cypher, N. Chevrollier, N. Montavont, and N. Golmie, "Prevailing over wires in healthcare environments: benefits and challenges," *IEEE Commun. Mag.*, vol. 44, pp. 56–63, April 2006.

[5] R. Kohno, K. Hamaguchi, H. B. Li, and K. Takizawa, "R&D and standardization of body area network (BAN) for medical healthcare," in *Proc. IEEE Int. Conf. Ultra-Wideband*, vol. 3, pp. 5–8, 2008.

[6] D. B. Smith, D. Miniutti, T. A. Lamahewa, and L. W. Hanlen, "Propagation models for body-area networks: A survey and new outlook," *IEEE Antennas Propag. Mag.*, vol. 55, pp. 97–117, Oct. 2013.

[7] "IEEE 802.15 WPAN task group 6 body area networks." http://www.ieee802.org/15/pub/TG6.html, Jan. 2008.

[8] J. Foerster, J. Lansford, J. Laskar, T. Rappaport, and S. Kato, "Realizing Gbps wireless personal area networks - guest editorial," *IEEE J. Sel. Areas Commun.*, vol. 27, pp. 1313–1317, Oct. 2009.

[9] C. Park and T. Rappaport, "Short-range wireless communications for next-generation networks: UWB, 60 GHz millimeter-wave WPAN, and zigbee," *IEEE Wireless Commun.*, vol. 14, pp. 70–78, Aug. 2007.

[10] "WirelessHD specification overview." accessed in Nov. 2014, [Online] Available: http://www.wirelesshd.org/pdfs/WirelessHD-SpecificationOverview-v1.1May2010.pdf, Aug. 2009.

[11] E. Perahia, C. Cordeiro, M. Park, and L. L. Yang, "IEEE 802.11ad: Defining the next generation multi-Gbps Wi-Fi," in *Proc. IEEE Consumer Commun. and Networking Conf. (CCNC)*, pp. 1–5, Jan. 2010.

[12] T. Bai and R. W. Heath Jr., "Coverage and rate analysis for millimeter-wave cellular networks," *IEEE Trans. Wireless Commun.*, vol. 14, pp. 1100–1114, Feb 2015.

[13] S. Singh, M. N. Kulkarni, A. Ghosh, and J. G. Andrews, "Tractable model for rate in self-backhauled millimeter wave cellular networks," *IEEE J. Sel. Areas Commun.*, vol. 33, pp. 2196–2211, Oct. 2015.

[14] T. Bai, A. Alkhateeb, and R. W. Heath Jr., "Coverage and capacity of millimeter-wave cellular networks," *IEEE Commun. Mag.*, vol. 52, pp. 70–77, Sept. 2014.

[15] D. Torrieri and M. C. Valenti, "The outage probability of a finite ad hoc network in Nakagami fading," *IEEE Trans. Commun.*, vol. 60, pp. 3509–3518, Nov. 2012.

[16] M. C. Valenti, D. Torrieri, and S. Talarico, "Adjacent-channel interference in frequency-hopping ad hoc networks," in *Proc. IEEE Int. Conf. on Commun. (ICC)*, pp. 5583–5588, June 2013.

[17] G. George and A. Lozano, "Performance of enclosed mmwave wearable networks," Dec. 2015.

[18] K. Venugopal, M. C. Valenti, and R. W. Heath, "Device-to-device millimeter wave communications: Interference, coverage, rate, and finite topologies," *IEEE Trans. Wireless Commun.*, vol. 15, pp. 6175–6188, Sept. 2016.

[19] K. Venugopal, M. C. Valenti, and R. W. Heath, "Analysis of millimeter-wave networked wearables in crowded environment," in *Proc. Asilomar Conf. Signals, Syst., Comput.*, Nov. 2015.

[20] K. Venugopal and R. W. Heath, "Location based performance model for indoor mmwave wearable communication," in *Proc. IEEE Int. Conf. on Commun. (ICC)*, pp. 1–6, May 2016.

[21] K. Venugopal and R. W. Heath, "Millimeter wave networked wearables in dense indoor environments," *IEEE Access*, vol. 4, pp. 1205–1221, 2016.

[22] K. Venugopal, A. Alkhateeb, R. W. Heath, and N. González-Prelcic, "Time-domain channel estimation for wideband millimeter wave systems with hybrid architecture," in *Proc. Int. Conf. Acoust., Speech and Sig. Proc. (ICASSP)*, pp. 1–5, Sept. 2016.

[23] K. Venugopal, A. Alkhateeb, N. González-Prelcic, and R. W. Heath, "Channel estimation for hybrid architecture based wideband millimeter wave systems," *(to appear) IEEE J. Sel. Areas Commun.*, Nov. 2016. `https://arxiv.org/abs/1611.03046`.

[24] K. Venugopal, N. González-Prelcic, and R. W. Heath, "Optimality of frequency flat precoding in frequency selective millimeter wave channels,," *(to appear) IEEE Wireless Commun. Lett.*, Nov. 2016.

[25] J. Moar, "Smart wearable devices: Fitness, healthcare, entertainment & enterprise 2013-2018," *Juniper Research*, Oct. 2013.

[26] A. Pyattaev, K. Johnsson, S. Andreev, and Y. Koucheryavy, "Communication challenges in high-density deployments of wearable wireless devices," *IEEE Wireless Commun.*, vol. 22, pp. 12–18, Feb. 2015.

[27] F. Boccardi, R. W. Heath Jr., A. Lozano, T. L. Marzetta, and P. Popovski, "Five disruptive technology directions for 5G," *IEEE Commun. Mag.*, vol. 52, pp. 74–80, Feb. 2014.

[28] T. Rappaport *et al*, "Millimeter wave mobile communications for 5G cellular: It will work!," *IEEE Access*, vol. 1, pp. 335–349, 2013.

[29] P. Cardieri, "Modeling interference in wireless ad hoc networks," *IEEE Commun. Surveys and Tutorials*, vol. 12, pp. 551–572, Fourth Quarter 2010.

[30] J. G. Andrews, R. K. Ganti, M. Haenggi, N. Jindal, and S. Weber, "A primer on spatial modeling and analysis in wireless networks," *IEEE Commun. Mag.*, vol. 48, pp. 156–163, November 2010.

[31] M. Haenggi, J. G. Andrews, F. Baccelli, O. Dousse, and M. Franceschetti, "Stochastic geometry and random graphs for the analysis and design of wireless networks," *IEEE J. Sel. Areas Commun.*, vol. 27, pp. 1029–1046, Sept. 2009.

[32] M. Haenggi and R. K. Ganti, *Interference in large wireless networks*. Now Publishers, 2009.

[33] F. Baccelli and B. Blaszczyszyn, *Stochastic Geometry and Wireless Networks*. NOW: Foundations and Trends in Networking, 2010.

[34] T. Rappapport, R. W. Heath Jr., R. Daniels, and J. N. Murdock, *Millimeter Wave Wireless Communications*. Pearson Education, Inc., 2014.

[35] T. Rappaport *et al*, "Broadband millimeter-wave propagation measurements and models using adaptive-beam antennas for outdoor urban cellular communications," *IEEE Trans. Antennas Propag.*, vol. 61, pp. 1850–1859, April 2013.

[36] T. Bai, R. Vaze, and R. W. Heath Jr., "Analysis of blockage effects on urban cellular networks," *IEEE Trans. Wireless Commun.*, vol. 13, pp. 5070–5083, Sept. 2014.

[37] J. S. Lu, D. Steinbach, P. Cabrol, and P. Pietraski, "Modeling human blockers in millimeter wave radio links," *ZTE Communications*, vol. 10, pp. 23–28, Dec. 2012.

[38] T. Bai and R. W. Heath Jr., "Analysis of self-body blocking effects in millimeter wave cellular networks," in *Proc. Asilomar Conf. Signals, Syst., Comput.*, pp. 1921–1925, Nov. 2014.

[39] H. Xu, V. Kukshya, and T. Rappaport, "Spatial and temporal characteristics of 60-ghz indoor channels," *IEEE J. Sel. Areas Commun.*, vol. 20, pp. 620–630, April 2002.

[40] "IEEE 802.15 task group 3c: Channel modeling sub-committee final report." accessed in Nov. 2015, [Online], Available: `http://www.ieee802.org/15/pub/TG3c_contributions.html`.

[41] C. A. Balanis, *Antenna Theory: Analysis and Design, Third Edition*. Wiley Interscience, 2012.

[42] H. Li, Y.-D. Yao, and J. Yu, "Outage probabilities of wireless systems with imperfect beamforming," *IEEE Trans. Veh. Technol.*, vol. 55, pp. 1503–1515, Sept. 2006.

[43] J. Wildman, P. H. J. Nardelli, M. Latva-aho, and S. Weber, "On the joint impact of beamwidth and orientation error on throughput in directional wireless Poisson networks," *IEEE Trans. Wireless Commun.*, vol. 13, pp. 7072–7085, Dec. 2014.

[44] H. Alzer, "On some inequalities for the incomplete gamma function," *Math. of Computation*, vol. 66, pp. 771–778, April 1997.

[45] A. Papoulis and S. U. Pillai, *Probability, Random Variables and Stochastic Processes, Fourth Edition.* McGraw Hill, 2002.

[46] "Railway Passenger Vehicle Capacity, An overview of the way railway vehicle capacity has evolved." accessed in Jan. 2015, [Online] Available: `http://www.railwaytechnical.com/Infopaper%202%20Railway%20Passenger%20%Vehicle%20Capacity%20v1.pdf`.

[47] M. C. Valenti, D. Torrieri, and S. Talarico, "A direct approach to computing spatially averaged outage probability," *IEEE Commun. Lett.*, vol. 18, pp. 1103–1106, July 2014.

[48] "2014 public transportation fact book," *American Public Transportation Assoc.*, Nov. 2014.

[49] S. Cotton, W. Scanlon, and P. Hall, "A simulated study of co-channel inter-ban interference at 2.45 GHz and 60 GHz," in *Proc. European Wireless Technol. Conf. (EuWIT)*, pp. 61–64, Sept. 2010.

[50] S. Collonge, G. Zaharia, and G. Zein, "Influence of the human activity on wide-band characteristics of the 60 GHz indoor radio channel," *IEEE Trans. Wireless Commun.*, vol. 3, pp. 2396–2406, Nov. 2004.

[51] P. Karadimas, B. Allen, and P. Smith, "Human body shadowing characterization for 60-GHz indoor short-range wireless links," *IEEE Antennas Wireless Propag. Lett.*, vol. 12, pp. 1650–1653, Dec. 2013.

[52] A. Abouraddy and S. Elnoubi, "Statistical modeling of the indoor radio channel at 10 GHz through propagation measurements .I. narrow-band measurements and modeling," *IEEE Trans. Veh. Technol.*, vol. 49, pp. 1491–1507, Sept. 2000.

[53] D. Beauvarlet and K. Virga, "Measured characteristics of 30-GHz indoor propagation channels with low-profile directional antennas," *IEEE Antennas Wireless Propag. Lett.*, vol. 1, no. 1, pp. 87–90, 2002.

[54] G. R. Maccartney, T. S. Rappaport, S. Sun, and S. Deng, "Indoor office wideband millimeter-wave propagation measurements and channel models at 28 GHz and 73 GHz for ultra-dense 5G wireless networks," *IEEE Access*, vol. PP, pp. 1–1, Oct. 2015.

[55] R. W. Heath, N. González-Prelcic, S. Rangan, W. Roh, and A. M. Sayeed, "An overview of signal processing techniques for millimeter wave MIMO systems," *IEEE J. Sel. Topics Signal Process.*, vol. 10, pp. 436–453, April 2016.

[56] J. Singh, S. Ponnuru, and U. Madhow, "Multi-gigabit communication: the ADC bottleneck," in *Proc. of IEEE Int. Conf. Ultra-Wideband (ICUWB)*, (Vancouver, BC), pp. 22–27, Sept. 2009.

[57] O. El Ayach, S. Rajagopal, S. Abu-Surra, Z. Pi, and R. Heath, "Spatially sparse precoding in millimeter wave MIMO systems," *IEEE Trans. Wireless*

Commun., vol. 13, pp. 1499–1513, March 2014.

[58] A. Alkhateeb, J. Mo, N. González-Prelcic, and R. Heath, "MIMO precoding and combining solutions for millimeter-wave systems," *IEEE Commun. Mag.*, vol. 52, pp. 122–131, Dec. 2014.

[59] J. Wang, "Beam codebook based beamforming protocol for multi-Gbps millimeter-wave WPAN systems," *IEEE J. Sel. Areas Commun.*, vol. 27, pp. 1390–1399, Oct. 2009.

[60] L. Chen, Y. Yang, X. Chen, and W. Wang, "Multi-stage beamforming codebook for 60GHz WPAN," in *Proc. of 6th Int. ICST Conf. Commun. and Networking in China*, (China), pp. 361–365, 2011.

[61] S. Hur, T. Kim, D. Love, J. Krogmeier, T. Thomas, and A. Ghosh, "Millimeter wave beamforming for wireless backhaul and access in small cell networks," *IEEE Trans. Commun.*, vol. 61, pp. 4391–4403, Oct. 2013.

[62] Y. Tsang, A. Poon, and S. Addepalli, "Coding the beams: Improving beamforming training in mmwave communication system," in *Proc. IEEE Global Telecommun. Conf. (GLOBECOM)*, (Houston, TX), pp. 1–6, Dec. 2011.

[63] "IEEE 802.15 WPAN millimeter wave alternative PHY task group 3c (TG3c)." `http://www.ieee802.org/15/pub/TG3c_contributions.html`.

[64] A. Alkhateeb, O. El Ayach, G. Leus, and R. Heath, "Channel estimation and hybrid precoding for millimeter wave cellular systems," *IEEE J. Sel. Topics Signal Process.*, vol. 8, pp. 831–846, Oct. 2014.

[65] R. Mendez-Rial, C. Rusu, N. González-Prelcic, A. Alkhateeb, and R. Heath, "Hybrid MIMO architectures for millimeter wave communications: Phase shifters or switches?," *IEEE Access*, vol. PP, no. 99, pp. 1–1, 2016.

[66] A. Alkhateeb, G. Leus, and R. Heath, "Compressed-sensing based multi-user millimeter wave systems: How many measurements are needed?," in *Proc. IEEE Int. Conf. Acoustics, Speech and Sig. Process. (ICASSP), Brisbane, Australia, arXiv preprint arXiv:1505.00299*, April 2015.

[67] Y. Han and J. Lee, "Two-stage compressed sensing for millimeter wave channel estimation," in *Proc. IEEE Int. Symp. on Inform. Theory (ISIT)*, pp. 860–864, July 2016.

[68] J. Lee, G.-T. Gil, and Y. Lee, "Exploiting spatial sparsity for estimating channels of hybrid MIMO systems in millimeter wave communications," in *Proc. IEEE Global Telecommun. Conf. (GLOBECOM)*, pp. 3326–3331, Dec. 2014.

[69] M. A. Iwen and A. H. Tewfik, "Adaptive strategies for target detection and localization in noisy environments," *IEEE Trans. Signal Proc.*, vol. 60, pp. 2344–2353, May 2012.

[70] M. Malloy and R. D. Nowak, "Near-optimal compressive binary search," *CoRR*, vol. abs/1203.1804, 2012. `http://arxiv.org/abs/1203.1804`.

[71] D. Ramasamy, S. Venkateswaran, and U. Madhow, "Compressive adaptation of large steerable arrays," in *Proc. IEEE Inform. Theory and Applicat. Workshop (ITA)*, pp. 234–239, Feb. 2012.

[72] D. E. Berraki, S. M. D. Armour, and A. R. Nix, "Application of compressive sensing in sparse spatial channel recovery for beamforming in mmwave outdoor systems," in *Proc. IEEE Wireless Commun. and Networking Conf.*, pp. 887–892, April 2014.

[73] H. Ghauch, T. Kim, M. Bengtsson, and M. Skoglund, "Subspace estimation and decomposition for large millimeter-wave MIMO systems," *IEEE J. Sel. Topics Signal Process.*, vol. 10, pp. 528–542, April 2016.

[74] M. Kokshoorn, P. Wang, Y. Li, and B. Vucetic, "Fast channel estimation for millimetre wave wireless systems using overlapped beam patterns," in *Proc. IEEE Int. Conf. on Commun. (ICC)*, pp. 1304–1309, June 2015.

[75] D. Zhu, J. Choi, and R. W. Heath Jr, "Auxiliary beam pair enabled aod and aoa estimation in closed-loop large-scale mmwave MIMO system," *arXiv preprint arXiv:1610.05587*, 2016.

[76] A. Ghosh, T. Thomas, M. Cudak, R. Ratasuk, P. Moorut, F. Vook, T. Rappaport, G. MacCartney, S. Sun, and S. Nie, "Millimeter-wave enhanced local area systems: A high-data-rate approach for future wireless networks," *IEEE J. Sel. Areas Commun.*, vol. 32, pp. 1152–1163, June 2014.

[77] Z. Gao, C. Hu, L. Dai, and Z. Wang, "Channel estimation for millimeter-wave massive MIMO with hybrid precoding over frequency-selective fading channels," *IEEE Commun. Lett.*, vol. 20, pp. 1259–1262, June 2016.

[78] B. Gao, Z. Xiao, L. Su, Z. Chen, D. Jin, and L. Zeng, "Multi-device multi-path beamforming training for 60-ghz millimeter-wave communications," in *Proc. IEEE Int. Conf. on Commun. (ICC)*, pp. 1328–1333, June 2015.

[79] P. Schniter and A. Sayeed, "Channel estimation and precoder design for millimeter-wave communications: The sparse way," in *Proc. Asilomar Conf. Signals, Syst., Comput.*, pp. 273–277, Nov. 2014.

[80] A. Alkhateeb and R. W. Heath Jr., "Frequency selective hybrid precoding for limited feedback millimeter wave systems," *IEEE Trans. Commun.*, vol. 64, pp. 1801–1818, May 2016.

[81] S. Guillouard, G. E. Zein, and J. Citerne, "Wideband propagation measurements and doppler analysis for the 60 GHz indoor channel," in *IEEE MTT-S Int. Microwave Symp. Digest (Cat. No.99CH36282)*, vol. 4, pp. 1751–1754 vol.4, June 1999.

[82] N. Moraitis and P. Constantinou, "Indoor channel measurements and characterization at 60 GHz for wireless local area network applications," *IEEE Trans. Antennas Propag.*, vol. 52, pp. 3180–3189, Dec. 2004.

[83] P. F. M. Smulders, "Statistical characterization of 60-GHzi indoor radio channels," *IEEE Trans. Antennas Propag.*, vol. 57, pp. 2820–2829, Oct. 2009.

[84] Z. Wang, X. Ma, and G. B. Giannakis, "OFDM or single-carrier block transmissions?," *IEEE Trans. Commun.*, vol. 52, pp. 380–394, March 2004.

[85] G. Taubock, F. Hlawatsch, D. Eiwen, and H. Rauhut, "Compressive estimation of doubly selective channels in multicarrier systems: Leakage effects and sparsity-enhancing processing," *IEEE J. Sel. Topics Signal Process.*, vol. 4, pp. 255–271, April 2010.

[86] R. Méndez-Rial, C. Rusu, N. González-Prelcic, A. Alkhateeb, and R. W. Heath, "Hybrid MIMO architectures for millimeter wave communications: Phase shifters or switches?," *IEEE Access*, Jan. 2016.

[87] Y. C. Eldar and G. Kutyniok, *Compressed sensing: theory and applications*. Cambridge University Press, 2012.

[88] T. Blumensath and M. E. Davies, "On the difference between orthogonal matching pursuit and orthogonal least squares," 2007.

[89] Y. Chen, J. Zhang, and A. D. S. Jayalath, "New training sequence structure for zero-padded sc-fde system in presence of carrier frequency offset," in *Proc. IEEE Veh. Tech. Conf. (VTC)*, pp. 1–4, Sept. 2008.

[90] Z. Gao, L. Dai, W. Dai, B. Shim, and Z. Wang, "Structured compressive sensing-based spatio-temporal joint channel estimation for FDD massive MIMO," *IEEE Trans. Commun.*, vol. 64, pp. 601–617, Feb. 2016.

[91] B. Wang, L. Dai, T. Mir, and Z. Wang, "Joint user activity and data detection based on structured compressive sensing for noma," *IEEE Commun. Lett.*, vol. 20, pp. 1473–1476, July 2016.

[92] W. Roh *et al*, "Millimeter-wave beamforming as an enabling technology for 5G cellular communications: theoretical feasibility and prototype results," *IEEE Commun. Mag.*, vol. 52, pp. 106–113, Feb. 2014.

[93] P. Sudarshan, N. B. Mehta, A. F. Molisch, and J. Zhang, "Channel statistics-based RF pre-processing with antenna selection," *IEEE Trans. Wireless Commun.*, vol. 5, pp. 3501–3511, Dec. 2006.

[94] S. Park, A. Alkhateeb, and R. W. Heath Jr., "Dynamic subarrays for hybrid precoding in wideband mmwave MIMO systems," *CoRR*, vol. abs/1606.08405, 2016. `http://arxiv.org/abs/1606.08405`.

[95] G. R. M. J. Shu Sun and T. S. Rappaport, "A novel millimeter-wave channel simulator and applications for 5G wireless communications," in *Proc. IEEE Int. Conf. on Commun. (ICC)*, pp. 5583–5588, May 2017.

[96] E. Telatar, "Capacity of multi-antenna Gaussian channels," *European Trans. on Telecommun.*, vol. 10, pp. 585–595, Nov. 1999.

[97] K. Zhong, P. Jain, and I. S. Dhillon, "Efficient matrix sensing using rank-1 Gaussian measurements," in *Proc. Int. Conf. Algorithmic Learning Theory (ALT)*, pp. 3–18, Oct. 2015.

[98] S. Haghighatshoar and G. Caire, "Low-complexity massive MIMO subspace estimation and tracking from low-dimensional projections," *CoRR*, vol. abs/1608.02477, 2016. `https://arxiv.org/abs/1608.02477`.

[99] T. Marrinan, B. Draper, J. R. Beveridge, M. Kirby, and C. Peterson, "Finding the subspace mean or median to fit your need," in *Proc. IEEE Conf. Comput. Vision Pattern Recog.*, pp. 1082–1089, June 2014.

[100] Q. Rentmeesters, P. A. Absil, P. V. Dooren, K. Gallivan, and A. Srivastava, "An efficient particle filtering technique on the grassmann manifold," pp. 3838–3841, March 2010.

[101] "IEEE standard for safety levels with respect to human exposure to radio frequency electromagnetic fields, 3 kHz to 300 GHz," *IEEE Std C95.1-2005*, pp. 1–238, April 2006.

[102] T. Wu, T. Rappaport, and C. Collins, "Safe for generations to come: Considerations of safety for millimeter waves in wireless communications," *IEEE Microwave Mag.*, vol. 16, pp. 65–84, March 2015.

[103] K. Ryan, J. D'Andrea, J. Jauchem, and P. Mason, "Radio frequency radiation of millimeter wave length: potential occupational safety issues relating to surface heating," *Health Phys.*, vol. 78, no. 2, pp. 170–181, 2000.

[104] A. Hajimiri, "mm-wave silicon ICs: Challenges and opportunities," in *IEEE Custom Integrated Circuits Conf. (CICC), 2007*, pp. 741–747, Sept. 2007.

[105] T. Rappaport, J. Murdock, and F. Gutierrez, "State of the art in 60-GHz integrated circuits and systems for wireless communications," *Proc. of the IEEE*, vol. 99, pp. 1390–1436, Aug. 2011.

[106] P. Smulders and A. Wagemans, "Wide-band measurements of mm-wave indoor radio channels," in *Proc. Int. Symp. Personal, Indoor, & Mobile Radio Commun. (PIMRC)*, pp. 329–333, Oct. 1992.

[107] A. Kato, T. Manabe, Y. Miura, K. Sato, and T. Ihara, "Measurements of millimeter wave indoor propagation and high-speed digital transmission characteristics at 60 GHz," in *Proc. Int. Symp. Personal, Indoor, & Mobile Radio Commun. (PIMRC)*, vol. 1, pp. 149–154 vol.1, Sept. 1997.

[108] S. Geng and P. Vainikainen, "Millimeter-wave propagation in indoor corridors," *IEEE Antennas Wireless Propag. Lett.*, vol. 8, pp. 1242–1245, Dec. 2009.

Publications

Publications related to the dissertation

1. Kiran Venugopal, Matthew C. Valenti and Robert W. Heath Jr.,"Interference in finite-sized highly dense millimeter wave networks," in *Proc. of Information Theory and Applications Workshop (ITA)*, 2015, pp. 175-180, Feb. 2015.

2. Kiran Venugopal, Matthew C. Valenti, and Robert W. Heath, Jr., "Device-to-Device Millimeter Wave Communications: Interference, Coverage, Rate, and Finite Topologies," in *IEEE Transactions on Wireless Communications*, vol. 15, no. 9, pp. 6175-6188, Sept. 2016. Available online at arXiv: 1506.07158v1 [cs.IT], 23 Jun 2015.

3. Kiran Venugopal, Matthew C. Valenti, and Robert W. Heath, Jr., "Analysis of Millimeter-Wave Networked Wearables in Crowded Environment," in *Proc. of Asilomar Conference on Signals, Systems, and Computers*, Nov. 2015.

4. Kiran Venugopal and Robert W. Heath, Jr., "Location Based Performance Model for Indoor MmWave Wearable Communication, in *Proc. of IEEE International Conference on Communications*, Kuala Lumpur, Malaysia, 2016, pp. 1-6, May 2016.

5. Kiran Venugopal and Robert W. Heath, Jr., "Millimeter Wave Networked Wearables in Dense Indoor Environments, in *IEEE Access*, vol. 4, pp. 1205-1221, 2016.

6. Geordie George, Kiran Venugopal, Angel Lozano, and Robert W. Heath, Jr., "Enclosed mmWave Wearable Networks: Feasibility and Performance," in *IEEE Transactions on Wireless Communications*, vol. 16, no. 4, pp. 2300-2313, April 2017. Available online at arXiv: 1607.04339 [cs.IT], 14 July 2016.

7. Kiran Venugopal, Ahmed Alkhateeb, Robert W. Heath, Jr., and Nuria González-Prelcic, "Time-Domain Channel Estimation for Wideband Millimeter Wave Systems With Hybrid Architecture," in *Proc. IEEE International Conference on Acoustics, Speech and Signal Processing (ICASSP)*, March 2017.

8. Kiran Venugopal, Ahmed Alkhateeb, Nuria González-Prelcic and Robert W. Heath, Jr., "Channel Estimation for Hybrid Architecture Based Wideband Millimeter Wave Systems," to appear in *IEEE Journal of Selected Areas in Communications*. Available at arXiv: 1611.03046 [cs.IT], 13 Nov. 2016.

9. Kiran Venugopal, Nuria González-Prelcic and Robert W. Heath, Jr., "Optimality of Frequency Flat Precoding in Frequency Selective Millimeter Wave Channels," to appear in *IEEE Wireless Communications Letters*, 24 Nov. 2016.

10. Javier Rodríguez-Fernández, Kiran Venugopal, Nuria González-Prelcic and Robert W. Heath, Jr., "A Frequency-Domain Approach to Wideband Channel Estimation in Millimeter Wave Systems," to appear in *Proc. of IEEE International Conference on Communications*, May 2017, Paris, France.

Other publications

1. Yuyang Wang, Kiran Venugopal, Andreas F. Molisch and Robert W. Heath, Jr., "Blockage and Coverage Analysis with MmWave Cross Street BSs Near Urban Intersections," to appear in *Proc. of IEEE International Conference on Communications*, May 2017, Paris, France.

2. Yuyang Wang, Kiran Venugopal, Andreas F. Molisch and Robert W. Heath, Jr., "MmWave vehicle-to-infrastructure communication: Analysis of urban microcellular networks," submitted to *IEEE Transactions on Vehicular Technology*, 26 Feb. 2017.

3. Yuyang Wang, Kiran Venugopal, Andreas F. Molisch and Robert W. Heath, Jr., "Analysis of Urban Millimeter Wave Microcellular Networks," in *Proc. of IEEE Vehicular Technology Conference*, 18-21 Sep. 2016, Montreal, Canada.

Vita

Kiran Venugopal received the B.Tech. degree in Electronics and Communication Engineering from National Institute of Technology, Calicut in 2011, and the M.E. degree in Telecommunication Engineering from Indian Institute of Science, Bangalore in 2013. Currently he is pursuing Ph.D. degree at the Wireless Networking and Communications group, Department of Electrical and Computer Engineering, the University of Texas at Austin. From 2013 to 2014 he worked as a Systems Design Staff Engineer at Broadcom Communication Technologies Pvt. Ltd., Bangalore. During the summers of 2015 he was a graduate intern at Intel Labs. In the summer of 2016, he was a research intern at Nokia Bell Labs, Arlington Heights, IL. His research interests include wireless communication, signal processing, network coding, and estimation theory. He was awarded Prof. S. V. C. Aiya Medal for best M.E. (Telecommunications) student, 2013 from Indian Institute of Science, Bangalore and Er. M.L. Bapna Gold Medal, 2011 from National Institute of Technology, Calicut for scoring the highest CGPA among all the under graduate programs.

Email address: kiranv@utexas.edu

This dissertation was typeset with LaTeX[†] by the author.

[†]LaTeX is a document preparation system developed by Leslie Lamport as a special version of Donald Knuth's TeX Program.